SODIUM ENERGETICS OF CHIMERIC FLAGELLAR MOTORS IN *Escherichia coli*

Chien-Jung Lo

A thesis submitted in partial fulfilment of
the requirement for the degree of
Doctor of Philosophy at the University of Oxford

University College
University of Oxford
Hilary Term 2007

Sodium Energetics of Chimeric Flagellar Motors in *Escherichia coli*

Chien-Jung Lo, University College
Thesis submitted for the degree of Doctor of Philosophy
at the University of Oxford, Hilary Term 2007

ABSTRACT

This thesis is a trilogy describing the fundamental investigation of the energy input and output of the chimeric flagellar motor in *Escherichia coli*. The motor contains parts from both proton- and sodium-driven motors and is driven by sodium ion flux and sodium-motive force (smf), comprising membrane potential (V_m) and sodium concentration gradient (ΔpNa) across membrane. We have developed single bacterial cell fluorescence measurement of intracellular sodium concentration ($[Na^+]_{in}$) and V_m to measure the smf of the chimeric motor. Combining high resolution single motor speed measurements and a fast flow-cell, we study the motor speed and functions in various regimes of load, number of torque-generating units and driving force.

In the $[Na^+]_{in}$ measurement, we develop a single cell fluorescence measurement using a sodium-sensitive fluorescent dye, Sodium Green. In order to have a precise single cell measurement, we calibrated each cell at the end of experiments. We have measured $[Na^+]_{in}$ in response to extracellular sodium concentrations ($[Na^+]_{ex}$) and extracellular pH (pH_{ex}). Thus the sodium concentration gradient can be calculated.

In the V_m measurement, we adapted a published fluorescence technique to the measurement of a single bacterial cell using the dye Tetramethyl Rhodamine Methyl Ester (TMRM). We used a convolution model to determine the relationship between fluorescence intensity in images of cells and intracellular dye concentration, and calculated V_m using the ratio of intracellular to extracellular dye concentrations. We have measured V_m in different $[Na^+]_{ex}$ and pH_{ex}. Combining these two fluorescence measurements, the smf of *E. coli* can be obtained.

We investigated motor speed of the chimeric motor using back-focal-plane (BFP) interferometry in different load, induction level and smf conditions. Steady-state low-level induction of stators during culture and "resurrection" are both useful methods to assess low-stator number rotation. We measured the torque-speed relationship by changing external viscosity and the motor speed with different smf in different load. Stable slow rotation conditions with known smf were found for the next stage of step experiments. Direct observations of steps in stable rotation and dwell time distributions are also presented.

ACKNOWLEDGEMENTS

Words can't fully express my gratitude to the people who accompanied me in my DPhil period. Those who teach me, help me, work with me, and inspire me, thank you.

First of all is my supervisor, the optimistic and brilliant mentor, Dr. Richard Berry. Thank you for the encouragement and productive discussions.
Thanks to all the laboratory members:
Dr. Mark Leake, for his great help on experiments and academic skills.
Dr. Alexander Rowe, Dr. Teuta Pilizota, Dr. Yoshiyuki Sowa, Dr. Jennifer Chandler, Fan Bai, Tania Saxl, Stuart Reid, Thomas Bilyard and Richard Branch for their assistance to my research and creating enjoyable lab environment.

Special thanks to Fan Bai for the many open discussions of physics and life.
Special thanks to Thomas Bilyard and Richard Branch for proofreading.

I also have to thank my computers who work with me for these years, without them, it is impossible to see this thesis.

Thanks to Professor Robin Nicholas for his encouragement of DPhil scholarship, and most of all, Swire Group and ORSAS for the scholarship and financial support to my DPhil study.

To my family, parents, sister, and brother, thank you for your long standing support.

Final words to my closest friend of my life, my wife, without you, I can't go so far.

ABBREVIATIONS

BFP	back-focal-plane
BFM	bacterial flagellar motor
CCCP	carbonyl cyanide 3-chlorophenylhydrazone
EDTA	ethylenediaminetetraacetic acid
QPD	quadrant photo diode
IPTG	isopropyl-ß-D-thiogalactopyranoside
LPS	lipopolysaccharide
$[Na^+]_{ex}$	extracellular sodium concentration
$[Na^+]_{in}$	intracellular sodium concentration
pH_{ex}	extracellular pH
pH_{in}	intracellular pH
pmf	proton-motive force
ΔpNa	sodium concentration gradient $\Delta pNa = log_{10}\{[Na^+]_{in}/[Na^+]_{ex}\}$
psf	point-spread-function
smf	sodium-motive force
TB	tryptone broth
TMRM	tetramethyl rhodamine methyl ester
V_m	membrane potential

TABLE OF CONTENTS

CHAPTER 1

INTRODUCTION

'We may, I believe, regard it as extremely improbable that our understanding of the world represents any definite or final stage, a maximum or optimum in any respect.'

Erwin Schrödinger (1887-1961)

Our current understanding of biology is down to the molecular level. In living organisms, biological functions are regulated by proteins, small molecules and molecular machines. Among these, from a physicist's eye, molecular motors are the most interesting subjects.

Biological molecular motors are defined as molecules or molecular complexes that can convert biological energy into force or torque to do physical work. These motors are related to locomotion, force generation, transportation and cellular regulation. Molecular motors are constructed from protein molecules and work in the nanometer (nm), piconewton (pN) and millisecond (ms) ranges. Surely, biology is wet and dynamic. All these molecular motors work in environments where inertia is insignificant and are subject to Brownian motion. Thus, the energetics of these systems is different from macro-scale machines.

Within these micro machines, the bacterial flagellar motor (BFM) is one of the most interesting motors, not only because of its role in bacterial chemotaxis, but also powerful

potential applications in the micro-scale world. Many species of bacteria use rotary motors to spin flagellar filaments for swimming. The motor is powered by ion flux, either protons or sodium ions through stators. This rotary machine can spin up to a few hundred Hz in physiological conditions, faster than the car engines. Even though we have learned a lot about this motor in the past three decades, we still can not build up a comparable man-made rotary molecular motor.

Since Robert Hooke (FRS, 1635-1703) introduced microscopy to biology, we can explore life on the micro-scale. It took more than one hundred years until Christian Ehrenberg (1795-1876) improved the quality of the microscope to be able to see the flagella of bacteria (1836). However, people put more emphasis on pathology than motility of bacteria at that time. Modern research on the BFM can be traced back to the 1960s when Cohen-Bazire and London showed that the basal body of the BFM is about 50 nm wide by electron-microscopy (EM) images [Cohen-Bazire , 1967] and Silverman and Siman showed that the BFM rotates rather than waving [Silverman, 1974]. It was finally realized that the BFM is a tiny rotary molecular motor. In the last three decades, new experimental and theoretical tools and ideas have been applied to this field including assembly, chemotaxis, energetics, and performance. However, the detailed mechanism of torque generation remains a puzzle.

To understand an unknown machine, there are two methodologies that one can use. One is watching the performance of the machine and the other one is taking the machine apart. The motor is a complex with ~25 proteins in the final structure. The torque is thought to be generated between stators and rotor. Stator proteins are membrane proteins with unknown atomic structure and are difficult to purify. Therefore, measuring BFM performance in different conditions would be a good approach to understand the mechanism. We are not simply observing an event or a behavior. To reach a new level of understanding of this system, we need to make quantitative biophysical measurements. Due to recent developments in optical tweezers, fluorescence microscopy and biochemistry, we can measure biological and physical parameters with high precision.

The motivation underlying my research is the question of the energy usage of the BFM. Biological systems are subject to physical laws but are much more complex than

previously thought. We used an *Escherichia coli (E. coli)* strain containing a chimeric flagellar motor with proton- and sodium-driven components that functions as a sodium-driven motor. This is a special and powerful system for further understanding and better controlling the BFM. Because sodium energetics plays a secondary role in *E. coli*, the manipulation of motor rotating speed via external sodium concentration is not damaging to the cell [Sowa, 2005]. We aim to understand the motor function and its relationship to the motor driving force of this chimeric motor in *E. coli*.

The structure of this thesis is organized as follows:

In Chapter 2, a review of molecular motors and, in particular, the BFM is presented. This is with the aim of presenting the current understanding of molecular motors, the recent research results of the BFM and the latest progress.

Chapter 3 describes experimental techniques used in this thesis including fluorescence microscopy, optical trap and single motor speed measurements. Details of strains used in this thesis are also included.

The main research results of this thesis are in three parts. Chapter 4 and Chapter 5 cover the developments of the single cell fluorescence measurements of intracellular sodium concentrations ($[Na^+]_{in}$) and membrane potentials (V_m) respectively. The energy-transducing cytoplasmic membrane of bacteria contains pumps and antiports maintaining the membrane potential and ion gradients. In Chapter 4, we develop a method for rapid, single-cell measurement of the $[Na^+]_{in}$ in *E. coli* using the sodium ion fluorescence indicator, Sodium Green. With the final calibration of every cell, we can make precise single cell $[Na^+]_{in}$ measurements and obtain sodium concentration gradient, ΔpNa.

In Chapter 5, we demonstrate the development of the fluorescence technique to measure V_m in single cells, using the Tetramethyl Rhodamine Methyl Ester (TMRM) dye. We used a convolution model to determine the relationship between fluorescence intensity in images of cells and intracellular dye concentrations; and calculated V_m using the ratio of intracellular to extracellular dye concentrations. Combining the knowledge of Chapter 4 and Chapter 5, the sodium-motive force (smf) of the chimeric motor can be obtained.

Chapter 6 shows the most important contribution of this thesis where the mechanical performance and sodium energetics are related. First we demonstrate that the steady-state speed measurements and resurrection measurements are consistent ways of obtaining motor speed with different stator numbers. Second, the torque-speed relationship under different conditions is informative for the understanding of the motor output. We compare the torque-speed relationship of the chimeric motor with the wild-type proton motor and the wild-type sodium motor in *V. alginolyticus*. Third, we control the smf and vary the two components of smf separately via pH_{ex} and $[Na^+]_{ex}$. We measure the speed in different combinations of smf in order to understand the influence of the two components on motor function. We found different effects on the motor with high-load and low-load. Fourth, in low smf conditions, stepwise and stable rotation of the chimeric motor in *E. coli* can be observed. Statistical results can provide hints to the BFM mechanism.

In Chapter 7, conclusions of this thesis and outlook of future works are discussed.

CHAPTER 2

MOLECULAR MOTORS

Living cells have molecular motors that convert free energy into controlled motion or mechanical power. These motors can be cataloged into two types of motion: linear and rotary. Three types of linear motors are known: myosins, which move on actin filaments, and dyneins and kinesins, which use microtubules as tracks [Schliwa, 2003]. Three types of rotary motors are known: F_1 and F_o in ATP synthase, and the BFM. In a broader definition of 'molecular motors', many enzymes have been found to perform some controlled motion or force generation such as DNA and RNA polymerases or helicases which will not be discussed in this thesis.

This Chapter is divided into three parts: a broad overview of molecular motors, a review of the BFM including structure and performance, and an introduction of the chimeric BFM which is the focus of research in this thesis.

2-1 Introduction of Molecular Motors

Two different energy sources are used by molecular motors, ATP hydrolysis and ion-motive force. The natural energy unit in this micro-environment is k_BT, the thermal

energy of a molecule at temperature T, where k_B is Boltzmann's constant and T is absolute temperature. The ATP hydrolysis energy (ATP → ADP + Pi) is about 24 k_BT depending on the conditions. Cells maintain proton-motive force at ~ -150 mV (-150 meV ~ 6 k_BT). These molecular motors operate in the micro-scale facing huge fluctuations. Current researches seek understanding of their mechanical and energetic (chemical) cycles. Theorists look for physical principles that can govern and describe these tiny machines.

2-1-1 Linear Motors

Linear motors are mainly responsible for movement in the cellular world with a 'walking' protein on a 'track' progressing in one direction [Schliwa, 2003]. These motors typically consist of one, two or more large heads that allow attachment to the track (motor domain), a central coiled region, and a light-chain region which connects to other intracellular structures or cargo. Myosins are involved in contractile motion and organelle transport, kinesins are implicated in moving vesicles, and dyneins are required for eukaryotic flagella and ciliary function and cytoplasmic transport, Figure 2-1. These three types of linear motors each form a superfamily. From phylogenetic analyses, motors in the same superfamily possibly have a similar genetic origin and many of them have not had their specific functions characterized [Korn, 2000].

The general mechanisms of converting chemical energy into mechanical work are similar. The globular domain of the motors hydrolyzes ATP to cause conformation changes, leading to movement along the track. Kinesins show tight-coupling of one ATP for one step of 8 nm along microtubules in the plus-end direction. The maximum force that kinesin can exert is about 6 pN [Visscher, 1999]. Myosin V motors walk along the actin filaments with a step size of ~ 36 nm, corresponding to the pitch of the actin helix. The stall force for Myosin V is ~ 3 pN [Sellers, 2006]. In contrast, dynein shows 'gearing', a load-dependent step-size. In no load, dynein moves with a mixture of 24 nm and 32 nm steps. In medium and high load, they walk in 15 nm and 8 nm steps respectively [Mallik, 2004].

The observation of stepwise movement of linear motors leads to the next question of motor binding time. The duty ratio, r, is defined as the fraction of time the motor head is bound to its track, $r = t_{bind}/t_{total}$ [Howard, 1997]. Individual motors have high duty ratios to avoid losing their track when they are transporting cargos. For a two-headed myosin V molecule to be processive and maintain attachment to the actin filament, the duty ratio of a single motor head must be high; otherwise the motor would diffuse away while both motor heads were detached. The measured duty ratio is 0.7 for single myosin V motor heads [Cruz, 1999] which support the high processivity of myosin V. Another extreme case is where the motor head is detached from the track for most of the time. Skeletal muscle myosins work as a team with at least 10 to 100 motor molecules. The duty ratio must be small to optimize force generation.

Several experimental methods have been designed to perform single-molecule studies. Fluorescent labeled kinesin molecules can be observed moving along microtubules [Vale, 1996]. Direct observation of kinesin stepping has been reported by using optical trapping interferometry [Svoboda, 1993]. Optical trap experiments on single motors can measure mechanical properties such as step size and stall force in different energetic conditions

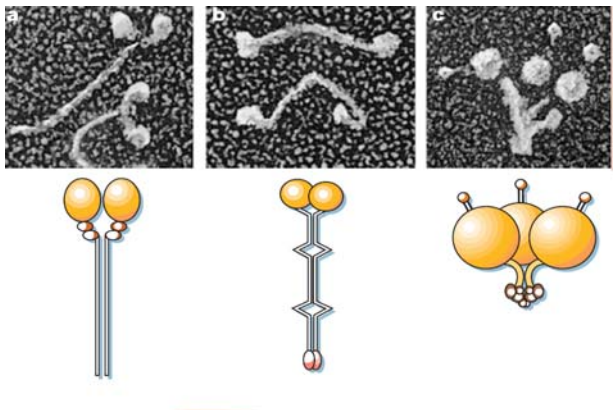

Figure 2-1: Linear molecular motors. (a) Myosin II; (b) kinesin; (c) ciliary dynein. Top row shows electron micrographs of quick-frozen individual molecules. Bottom row shows the cartoon drawing of these motors. Motor domains are in orange. Figure is adapted from [Schliwa, 2003].

and load. The rate-limiting step of the motor cycle can be found by changing external load or energetic conditions [Visscher, 1999]. Also, statistical information from the fundamental events can provide valuable knowledge of dwell time and step size which can show the hint of the motor mechanism. Here I show two examples of our current understanding of linear molecular motors.

Myosin V walking hand-over-hand:

The Myosin V molecule has two motor domains connected to a neck region, a coiled coil region and a cargo binding site, Figure 2-2 (A). It shows processive movement along actin tracks and has high actin affinity preventing the cargo from dissociating during kinetic cycles. Myosin V moves in a hand-over-hand mechanism with each head leading in turn. Using fluorescence microscopy, one can reach the resolution of a few nm for a single fluorescent molecule (fluorescence imaging with one nanometer accuracy, FIONA) [Yildiz, 2003]. A fluorescent molecule can form a diffraction limited image of width ~ 250 nm for visible light emission. With sufficient photons, the image (a 2D section of the point spread function) can be fitted with a Gaussian function [Cheezum, 2001]. The center of the image, indicating the position of the molecule, could be located with nm resolution.

In Myosin V, with cy3-labelled on one neck or GFP fused to the head, processive movement with ~72 nm steps can be observed [Yildiz, 2003]. It is consistent with the hand-over-hand model where the rear head moves forward and becomes the new leading head. The later experiment of a Myosin V molecule with two different quantum-dots labelled in two heads shows direct evidence of the hand over hand mechanism of walking along actin filaments [Warshaw, 2005].

Dynein in flagella:

The similarity of eukaryotic flagella and prokaryotic flagella (see Chapter 2-2) is morphological rather than mechanical. Sperm motility is generated by a highly organized axoneme which is a microtubule-dynein-based structure, Figure 2-2 (B). In the core of

the axoneme, nine special doublet microtubules are arranged in a ring around a pair of single microtubules [Inaba, 2003]. The doublet microtubules consist of one complete and

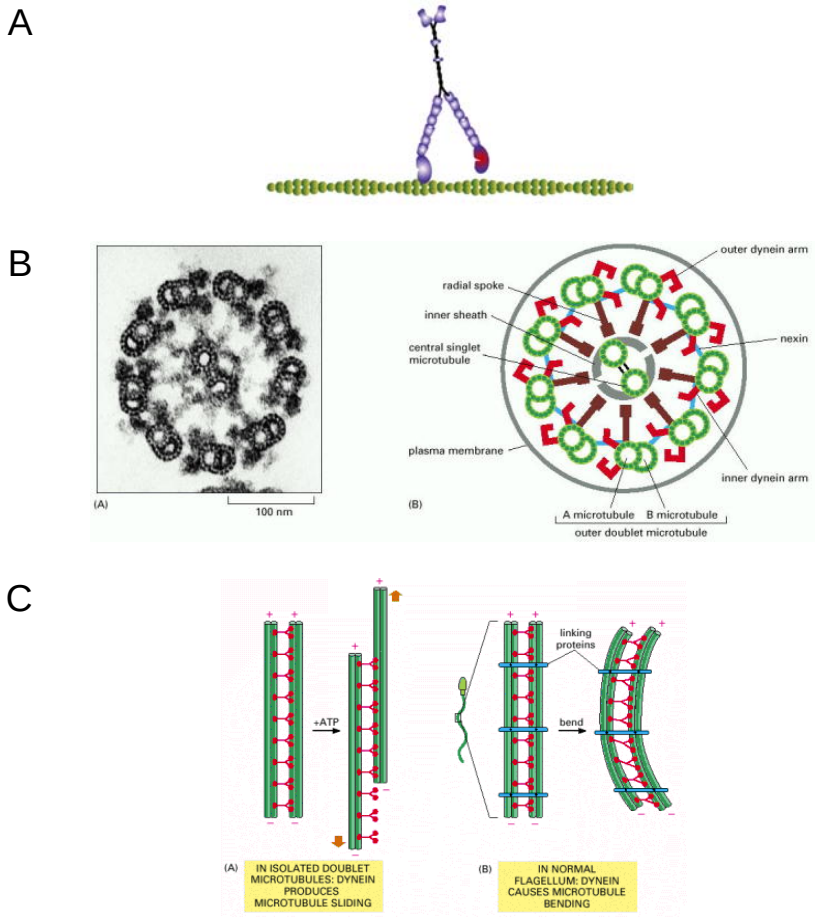

Figure 2-2 (A): Myosin V walks with ~ 36 nm steps. A Myosin V walking with one leg labeled with fluorophore shows ~72 nm steps, which suggests a hand-over-hand mechanism. Adapted from http://physiology.med.uvm.edu/warshaw/MMpgRI_mainframe.html

(B) Axoneme core arrangement. Left: Electron micrograph of the flagellum of a green alga shown in cross section. Right: Cartoon diagram of the 9+2 arrangement of the microtubules with dyneins connected to it. (C) The mechanism of bending of Axoneme. Left: Without the linkage between doublet microtubules, dyneins can move one microtubule against another one. Right: With linkage, the motor motion will cause bending of microtubules. (B, C) are adapted from [Molecular Biology of the Cell. 2002]

one partial microtubule fused together and sharing a tubule wall. Dynein molecules form bridges between the neighboring doublet microtubules. When dynein molecules attached to one microtubule and its motor domain attempts to walk along the neighboring microtubule, the neighboring microtubules tend to slide relative to another. However, there are also other links between microtubules which prevent sliding and result in a bending motion of microtubules. Thus, the whole flagellum can bend and wave as the driving force of sperm. Similar structure can be found in cilia, Figure 2-2 (C).

2-1-2 Rotary Motors

It is rare to find rotary machines in nature, compared to our daily life. Two types of rotary molecular motors are known: bacterial flagellar motors (BFM), which are ubiquitous rotary molecular machines in swimming bacteria, and F_1F_o ATP synthase, which is a rotary molecular motor consisting of 2 sub-motors, F_1 (subunits $\alpha_3\beta_3\gamma\varepsilon\delta$) and F_o (subunits $ab_2c_{10\text{-}14}$) sharing a common shaft, Figure 2-3. Even though these motors all rotate, the structures are quite different. The BFM will be discussed in Chapter 2-2.

F_1 is a soluble enzyme that can catalyze ATP synthesis by rotation. The membrane-bound F_0 converts ion motive force into mechanical torque. The whole system, generally couples the proton-motive force to the synthesis of ATP, though reversibility has also been demonstrated [Stock, 2000].

The torque drives the shaft consisting of subunits γ and ε that connect F_1 and F_o. $\alpha_3\beta_3$ subunits of F_1 form a hexamer $(\alpha\beta)_3$. The nucleotide-binding sites lie in the interface clefts between the subunits. Three catalytic sites lie mostly in β subunits, and non-catalytic sites lie mostly in α subunits. The hexamer surrounds the common shaft γ subunit with ε subunit in the end. The δ subunit sits atop of $\alpha_3\beta_3$ linking to the b_2 subunit of F_o. F_o can be divided into two parts, rotor and stator. The common shaft $\gamma\varepsilon$ connected to a ring shaped array of double-helix c subunits is the rotor. The number of c subunits is species dependent. The stator consists of ab_2 and is linked to F_1 by δ. b_2 and δ provide the

opposing elastic linkage between rotor and stator so that they can exert torque to each other.

Direct observation of the rotation of F_1 motor has been reported using fluorescent actin filaments attached to the γ subunit [Noji, 1997]. Later experiments showed the motor rotates in discrete 120^o steps [Yasuda, 1998]. Further higher angle resolution experiments using 40 nm beads attached to the γ subunit and dark-field microscopy show a 90^o substep due to ATP binding and a 30^o substep due to releasing hydrolysis products [Yasuda, 2001]. With 60 nm beads, the F_1 motors can rotate at an average speed of ~380 Hz in 2 mM ATP concentration [Nakanishi-Matsui, 2006]. The efficiency is very high and may be close to 100%.

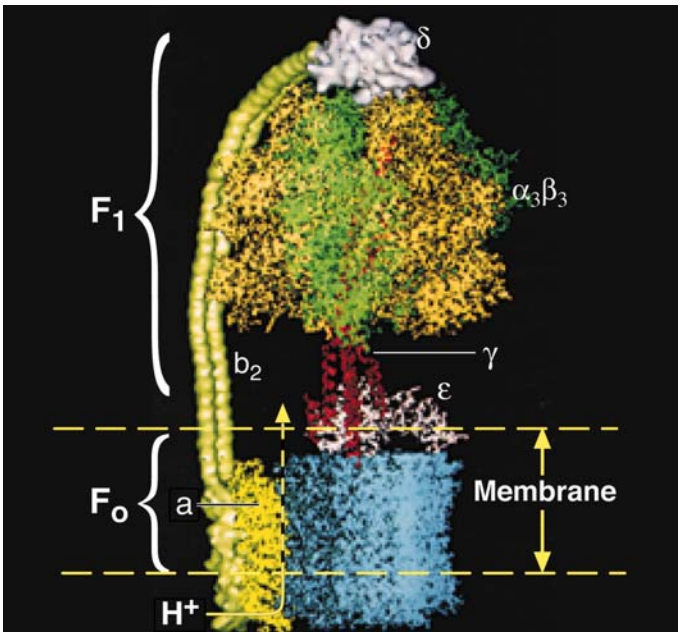

Figure 2-3: F_1Fo structure. Figure is adapted from [Xing, 2005].

Table 2-1

Stall Force/Torque of Molecular Motors.

Molecular Motor	Force/Torque	Reference
Myosin V	3 pN	[Sellers, 2006]
Kinesin	6 pN	[Visscher, 1999]
Dynein	1.1 pN	[Mallik, 2004]
F_1	40 pN nm	[Noji, 1997]
E. coli flagellar motor	1260 pN nm	[Reid, 2006]
Vibrio alginolyticus flagellar motor	3800 pN nm	[Sowa, 2003]

2-2 Bacterial Flagellar Motor

Many species of bacteria can swim by rotating their flagella, helical filaments extending outside the cell body and connected to a rotary motor embedded in the cell membrane, Figure 2-4. The external filament is a passive device unlike active flagella in eukaryotic cells (see Chapter 2-1-1). The BFM can output a power of about 1.5×10^5 pN nm s^{-1} [Ryu, 2000] and can make the cell swim at 30 μm s^{-1}, compared to the cell length of 2 μm. The BFM is probably the most complex, organized and powerful organelle found in bacteria. Table 2-1 lists the stall force/torque of different molecular motors. The BFM is not simply a propeller but also part of the chemotaxis pathway. It allows the bacteria to swim towards their favored environment. In this section, the current understanding of the bacterial flagellar motor architecture, composition, performance and energetics will be summarized.

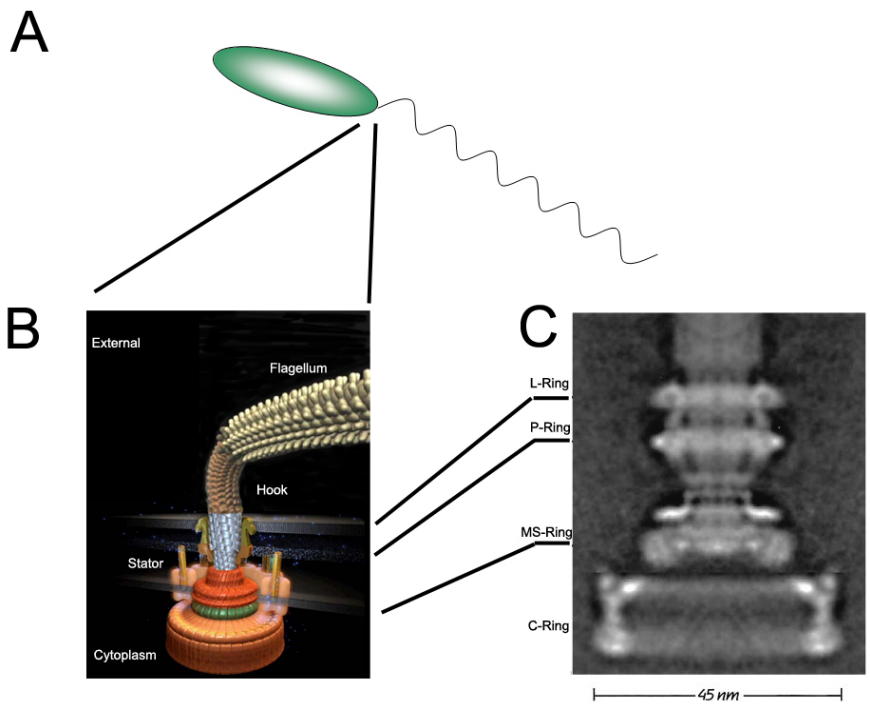

Figure 2-4: (A) Illustration of a bacterium with a single flagellum. (B) An enlarged view of the flagellar motor structure (Adapted from Prof. Homma's web page). (C) An averaged EM image of a basal body (rotor) from bacterial *Salmonella enterica* [Thomas, 2001].

2-2-1 Flagellar Motor Structure

Some species of bacteria have multi-flagella, some have only one. The BFM is one of the most complex structures in bacteria. There are 40-50 genes involved in its expression and assembly and ~ 25 different kinds of proteins in the final structure [Berg, 2003]. It looks like a man-made electrical motor with a propeller (flagellar filament, FliC), a hook (universal joint, FlgE), a rod (shaft), a series of rings for bushing (L-ring, FlgH; P-ring, FlgI), a rotor (MS-ring, FliF; C-ring, FliG, FliM, FliN), and stators (MotA, MotB). The width of the basal body is about 45 nm. The motor structure is shown schematically in Figure 2-5.

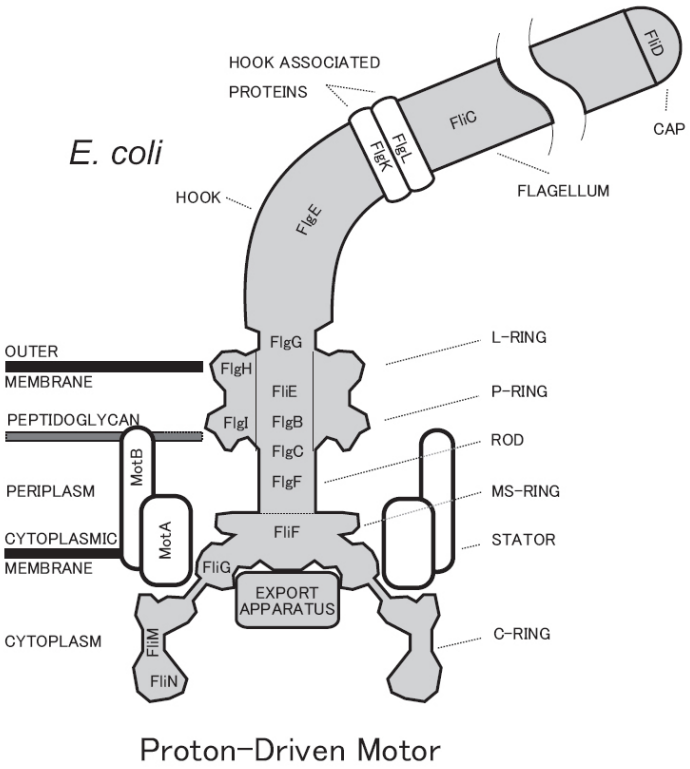

Figure 2-5: Schematic structure of the bacterial flagellar motor cross section. Stators are formed by MotA and MotB proteins and ~12 stators surround the rotor in *E. coli*. The torque is generated by the interaction between stators and rotor proteins, probably FliG. Figure is adapted from [Rowe, DPhil Thesis].

Main Structure:

The propeller (filament) is a polymer of single polypeptides, flagellin (FliC), that comprise 11 rows of subunits on the surface of a cylinder [Yonekura, 2003]. The filament is helical, rigid and about 5-10 μm long. The hook is a flexible polymer of single polypeptides, FlgE, connected to the basal body. The length of the hook is about 50 nm only but it is important as the universal joint for the bundling of flagellar filaments [Samatey, 2004]. The basal body comprises three rings, L-ring (FlgH), P-ring(FlgI), MS-ring(FliF), and a rod. The C-ring is in the cytoplasm and consists of three proteins (FliN,

FliM, FliG). FliM and FliN are thought to make up the switching complex. The chemotactic signaling protein, CheY-P, binds to FliM, thus changing the ratio of CW and CCW rotation. Structural analysis of purified rotors using EM images shows that the C-ring has 32-fold to 36-fold symmetry and MS-ring has 24-fold to 26-fold symmetry [Thomas, 2006]. Mainly, the basal body, hook, and filament are purely structural. It is thought that the torque is generated at the interface of stators and MS-ring or C-ring.

Stators:

The stator is thought to comprise MotA and MotB proteins. Sequence analysis suggests MotA has four trans-membrane sections and MotB has two trans-membrane sections. MotB has a peptidoglycan-binding domain near its C-terminus and is thought to anchor the stator complex to the cell wall. Therefore, the rotor and the filament can rotate relative to the cell wall. There is, however, no homology to any identified protein structure so far. It is likely that 4 MotA and 2 MotB proteins form a complex with 2 ion channels [Kojima, 2004].

In freeze-fracture preparations of inner membranes, stator complexes can be visualized as circular arrays of membrane particles. Images from different species show different numbers of stators in the motor: 10-12 stators in *E. coli* and *Streptococcus* [Khan, 1988] and 12 stators in *Salmonella typhimurium* [Khan, 1991]. In *motB* mutant cells, motor motility can be restored by expressing a wild-type gene from a plasmid in a process called ‘Resurrection’ [Block, 1984].

Recently, Leake et al. [2006] used fluorescent bleaching and GFP fused MotB in functioning flagellar motors to show that there are 22 ± 6 MotB proteins in one motor complex. Under strong bleaching laser power, the fluorescence of the GFP-MotB shows rapid decay and stepwise decay at the end of bleaching. Stochiometry supports the results from freeze-fracture EM images and two MotB per torque-generating unit results.

Proton Stator and Sodium Stators:

Bacterial flagellar motors are either driven by protons (H^+) or sodium ions (Na^+). *Salmonella typhimurium* and *E. coli* cells use protons to drive motors whose energetic cycle is a proton cycle. However, Alkaliphilic *Bacillus* lives at and is motile at pH 10-11.

The corresponding proton-motive force is small because the intracellular pH is maintained at 8-9. *Vibrio cholerae*, *Vibrio alginolyticus* and *Vibrio parahaemolyticus* also have sodium-driven polar flagellar motors. In *V. alginolyticus*, PomA and PomB are homologs of MotA and MotB respectively. PomA has 4 trans-membrane sections and PomB has 2 trans-membrane sections. Two other components, MotX and MotY, are essential for motor rotation in *V. alginolyticus* but the roles are unclear. MotX and MotY are membrane proteins with single transmembrane regions. A recent mutation study shows that their roles are stabilizing stator proteins [Yagasaki, 2006]. However, chimeric stators PomA/PotB (more details of chimeric motors in Chapter 2-3) can cooperate with FliG in *E. coli* and work as a sodium stator without MotX and MotY [Asai, 2003].

Rotor and Stator Interactions:

From structural and biochemical studies, it is thought that torque is generated between the C-terminal domain of the rotor protein FliG and the cytoplasmic loop of stator protein MotA. Due to the lack of atomic structure of stators, the detailed mechanism of the torque generation remains unknown. Mutation studies indicate several important functional residues in MotA, MotB and FliG. A conserved Asp residue near the inner end of the MotB membrane segment, Asp 32, is essential for rotation and is likely to be involved in proton transfer [Zhou, 1998]. In MotA, three important conserved charge residues in the cytoplasmic domain (Arg 90, Glu98, and Glu 150) and two residues near the inner end of membrane segments 3 and 4 (Pro 173 and Pro222) [Zhou, 1997; Braun, 1999] are found to be crucial for rotation. The C-terminal domain of FliG also contains conserved charged residues that are collectively important for the rotation [Lloyd, 1997].

Assembling Process:

The bacterial flagellum extends from the cytoplasm to the cell exterior. It is built from inside out and all the external proteins have to be exported by the type III pathway. The type III pathway is also utilized for secretion of virulence factors [Macnab, 2003]. First, the MS-ring and the export apparatus form. Then the stators, rod, and rings assemble. Finally, the hook and filament proteins export through the center of the basal body and form the exterior part. More details of the motor assembly can be found in mini-review [Macnab, 2003].

Known Atomic Structure of Motor Proteins:

Among the ~25 proteins in the motor final structure, some atomic structures are known.

1. Filament polypeptide structure, FliC [Samatey, 2001; Yonekura, 2003]

2. Hook polypeptide Structure, FlgE [Samatey, 2004]

3. Rotor protein, Part of C-ring, FliG [Lloyd, 1999; Brown, 2002]

4. Rotor protein, Part of C-ring, Switching complex, FliM [Park, 2006]

5. Rotor protein, Part of C-ring, Switching complex, FliN [Brown, 2005]

2-2-2 Performance

Rotation speed:

The proton motor in *E. coli* can rotate ~300 Hz (18,000 rpm) while the sodium motor in *V. algibilyticus* can rotate up to ~700 Hz (42,000 rpm) in room temperature. The record for the fastest rotation rate is ~1700Hz (~100,000 rpm) in the *V. algibilyticus* polar motor at 35 ^{o}C [Magariyama, 1995]. The sodium motor and proton motor have structural similarity. However, the reason for the faster rotation rate of sodium motor remains unknown. It could be that more stators exist in sodium motors or that there is a faster ion transfer rate in sodium motor stators.

Compared to the car engine (~6,000 rpm) and Formula 1 racing car (~22,000 rpm in 2006), the flagellar motor is an amazing natural rotary molecular machine.

Switching:

In *E. coli*, the motor can rotate in either direction, counterclockwise (CCW) or clockwise (CW), when watching from the filament end. When all of the motors rotate CCW, the filaments can form a bundle and propel the cell body forward (swim state). While one or more motors rotate CW, the filaments will fall apart and the cell body will stop (tumble state). In the tumble state, the cell will change direction randomly before returning to the swim state. Switching rate is associated with the chemotactic network by CheY binding to the switching complex of the motor. In a homogenous environment, the cells swim as a

'random walk'. In a gradient of attractant, cells extend the swim state as a 'positive biased random walk'. Thus, bacteria can sense the external condition and swim toward favorable environments [Berg, 2003]. The motor can output almost equal torque in CCW and CW states [Blair, 1988]. This is an important constraint for the models. In two states, stators operate in the same way but the rotor changes it's interactions with stators to change the rotation direction.

The detailed switching mechanism is unknown. Recent high time resolution experiments of single motor switching show the time scale of the switching is about a few milliseconds [Fan, B., personal communication]. The present 'Ising' model of switching describes the system as a ring of protomers (switching protein molecules) undergoing phase transition where the CheY binding affects the protomers' conformation/state [Duke, 2001]. Detailed atomic structures of the motor are needed to resolve this puzzle.

Torque-speed relation:

The torque-speed relationship of the BFM is informative. Previous studies of the wild-type proton-motor in *E. coli* show that, at 23 ^{o}C, the torque is nearly constant in the low-speed region up to ~170 Hz and drops rapidly to a zero-torque speed of ~350 Hz [Chen, 2000a], Figure 2-6 (A). In the plateau region, the estimated torque is about 1260 pN·nm in *E. coli* [Reid, 2006]. In this region, the torque generation is not limited by the internal processes, such as ion binding or torque generating conformation changes, but limited mechanically by the load on the motor. Further evidence, including that torque is independent of temperature and isotope, supports this conclusion. However, in the high speed and light load region, the torque is reduced rapidly and depends on temperature and hydrogen isotope, indicating that the internal processes are now rate limiting. A similar torque-speed relationship is also reported in *Vibrio alginolyticus* [Sowa, 2003] but the torque plateau region extends further to 450 Hz and a zero-torque speed at ~710 Hz, Figure 2-6 (B). The microscopic mechanisms in both proton- and sodium-motors may be similar but the reason for the higher speed and torque of the sodium motor remains unknown. The torque speed relationship of the chimeric motor may provide new insight (see Chapter 2-3, chimeric motor).

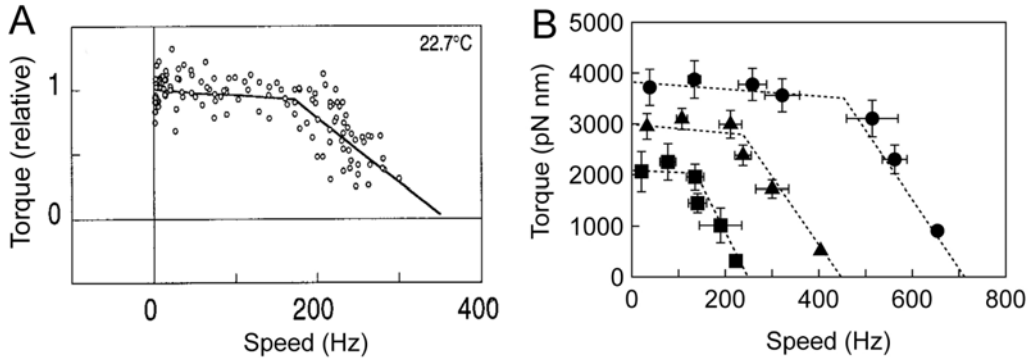

Figure 2-6 Torque-speed relationship of BFM. (A) Wild-type proton-motor in *E. coli*. The motor can generate nearly constant torque up to the 'knee speed' and drops rapidly at high speed. This figure is adapted from [Chen, 2000a]. Two linear fits are shown for speeds lower and higher than the knee speed. (B) Wild-type sodium motor in *V. alginolyticus*. Circle, triangle, and square is the data from $[Na^+]_{ex}$=50 mM, 10 mM and 3 mM respectively. Dash lines are the linear fit in two regimes. Figure is adapted from [Sowa, 2003].

Resurrection and Duty ratio:

One motor contains several stator complexes. Freeze-fracture EM images show there are 10-12 "studs" surrounding the rotor. In the *ΔmotA/B* strain, these studs are disappearing. In the non-motile cells of *motA* or *motB* mutant, the tethered cells' rotation can be restored after the wild-type MotA or MotB are expressed from the inducible plasmids [Block, 1984; Blair, 1988]. The motor speed shows stepwise increases and equal speed increments over the course of several minutes, Figure 2-7 (A). More recent and careful resurrection experiments of a 1 μm polystyrene bead attached to the truncated flagellar filament show that at least 11 levels can be seen [Reid, 2006], Figure 2-7 (B).

Using a bead assay, Ryu et al. extended the resurrection experiments to the light load region [Ryu, 2000]. In the high load region (1 μm beads), the speed increment is equal during the resurrection. However, in the light load region, the speed increment is

decreased and the speed is saturated. These results can be understood in terms of the 'duty ratio' of the stators, where the duty ratio is defined as the fraction of time that a stator binds to the rotor. If the duty ratio is low, the stators work independently, thus the motor speed increment should be equal in high and low load. If the duty ratio is high and the load is high, each stator can reach thermodynamic equilibrium and exert the same torque. The motor speed should increase linearly with stator number. However, in low load, the bound stators will limit motor speed. These results indicate that the duty ratio of the stator is high.

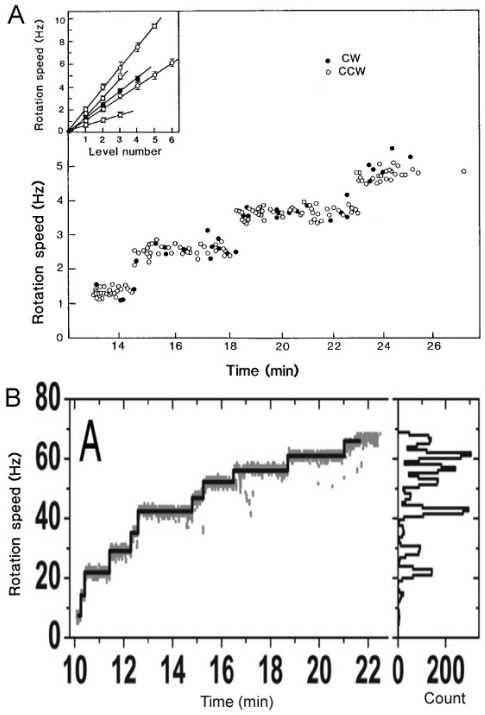

Figure 2-7: Resurrection experiments. (A) Rotation speed of a tethered motA cell restoring speed by expressing MotA from a plasmid. Stepwise speed indicates individual torque-generating units functioning in the motor. Inset shows speed of levels in different cells. Due to the difference in viscous drag from cell to cell, the slopes are different. Figure is adopted from [Blair, 1988]. (B) Rotation speed of 1 μm beads attached to motor of a similar strain. At least 11 discrete speed levels can be observed. Figure is from [Reid, 2006].

Stepping:

In the ATP-driven molecular motor system, single mechanical steps have been observed corresponding to the hydrolysis of a single ATP molecule. Kinesin walks 8 nm per step while hydrolyzing one ATP. In the rotary motor, F_1-ATPase takes 120^o-steps while hydrolyzing one ATP, corresponding to the three-fold symmetry of the motor. In later experiments in low-load, substeps (90^o and 30^o) of rotation were observed.

It is likely that transit of a quantized number of ions through the stator can cause a single movement of the motor. By comparison to the structure of the BFM with ~ 11 stators and ~ 24-26 fold symmetry of MS-ring and ~32-36 fold symmetry of C-ring, one might expect seeing ~ 14^o or ~ 11^o stepwise rotation corresponding to the stator interacting with rotor proteins.

The difficulties of direct observation include high speed (~ few hundred Hz) rotation and the flexible hook acting as an elastic damper. Because we observe the motor motion through a 'marker' such as beads linked to the motor, the stepwise motion of the BFM will be smoothed out through the elastic linker, hook. To reach a successful condition, we need to reduce the motor speed and increase the response speed of the marker, e.g., a motor with a low-stator number driving in low viscous load.

Beside these physical requirements of seeing a single step of the BFM, physiological conditions of cells are also important. We need to slow down the motor without irreversible damage to the cell. Thus it is desirable that we can control and measure ion-motive force at the same time. This is one of the original motivations of my chimeric motor research.

Analyzing motor speed fluctuation can shed some light on the step number of the motor. If n steps occur randomly over each revolution, the ratio of the standard deviation to the mean should be $n^{-1/2}$ [Samuel, 1995, 1996]. The estimated step number is ~400 with all of the stators. In the resurrection process, the number of steps per revolution was found to increase by 50 steps per level. However this method could be incorrect if the stators are cooperative and clocked to generate torque. Direct observation of steps and dwell time distribution can provide more information.

Technical difficulties defied direct observation of rotation steps for many years until the recent physical and biochemical developments of laser traps and chimeric motors. More details of the direct observation of stepwise rotation of the BFM will be discussed in Chapter 2-3.

2-2-3 Energetics

Ion Motive force (imf), Proton Motive Force (pmf), Sodium Motive Force (smf):

The BFM is powered by either proton or sodium ion flux rather than ATP hydrolysis. The electrochemical potential across the membrane defines the energy one ion can gain by transport through the membrane. The imf of a specific ion consists of two components, membrane potential (V_m) and a contribution from the ion concentration gradient ($2.3\ kT/q\ \Delta$pI, where ΔpI = $log_{10}\{[C^+]_{in}/[C^+]_{ex}\}$, k is Boltzmann's constant, T absolute temperature, q the unit charge, $[C^+]_{in}$ intracellular ion concentration, and $[C^+]_{ex}$ extracellular ion concentration),

$$imf = V_m + \frac{2.3kT}{q} \bullet \log_{10} \frac{[C^+]_{in}}{[C^+]_{ex}}. \qquad (2\text{-}1)$$

The equation is known as Nernst equation and valid in dilute ionic solution where the activity of ions is equal to their concentration. At higher concentration, this equation is an approximation.

If the coupled ions are protons, the imf can be re-written as proton-motive force (pmf),

$$pmf = V_m + \frac{2.3kT}{e}[pH_{ex} - pH_{in}]. \qquad (2\text{-}2)$$

In the case of the sodium-driven motor, the sodium-motive force (smf) is,

$$smf = V_m + \frac{2.3kT}{e} \bullet \log_{10} \frac{[Na^+]_{in}}{[Na^+]_{ex}}. \qquad (2\text{-}3)$$

***E. coli* Energetics:**

Membrane potential is the primary biological energy source for a cell to perform cellular functions such as signaling, regulation, energy balance and movement. In *E. coli*, the V_m is maintained at ~140 mV at pH 7 that is the ion balance of proton influx and proton efflux. The proton permeability of the cell membrane increases in acidic environments resulting in a decrease in V_m. However, internal pH (pH_{in}) decreases but not as much, so that the inward-directed ΔpH increases. The overall result is that the pmf increases only 20% from pH 7 to pH 5 [Minamino, 2003].

Motor speed vs imf:

The relationship between motor speed and ion-motive force has been reported in different bacteria with different methods. Note that swimming speed does not directly reflect motor function in *E. coli* because swimming depends upon the cooperation of flagella in bundles, and therefore early experiments with swimming *E. coli* cells are difficult to interpret. Berg's group showed a linear relationship between motor speed and pmf up to -85 mV in tethered *Streptococcus* cells, using a K^+ diffusion potential and a pH gradient to drive motors on starved cells [Manson, 1980; Khan, 1985]. Further studies on glycolyzing tethered *Streptococcus* cells suggested that the linear relationship between speed and pmf extends up to -150 mV [Meister, 1987]. Manson et al. also showed that the pH gradient and V_m were equivalent in tethered *Streptococcus* cells [Manson, 1980]. Using a micropipette to energize filamentous *E. coli* cells, with bead acting as markers attached to flagellar motors, Fung and Berg demonstrated the proportionality between speed and V_m up to -150 mV [Fung, 1995]. By observing a cell tethered to the coverslip by one motor (operating under high load) and measuring simultaneously the rotation of a second motor on the same cell (operating under lower load, marked by a 0.4 μm bead), Gabel and Berg showed that the speeds of the two motors were proportional when the pmf was gradually eliminated by adding the ionophore CCCP [Gabel, 2003]. The high-load motor in this experiment acted as an indicator of the pmf of the cell, as previous work had shown that speed is proportional to pmf under high load. Thus the experiment

demonstrated that speed varies linearly with pmf under both load conditions, although the relative contributions of V_m and pH gradient were not known. The motor speed of sodium-driven motors in *V. alginolyticus* has a linear dependence upon $log([Na^+]_{ex})$ but the smf was not measured [Sowa, 2003]. It is clear that the imf measurements are very important for the understanding of the motor energetics.

Difficulty of pmf manipulation:

Because pmf is the most important bioenergetic source in *E. coli*, it is difficult to manipulate it without damage to the cells. The cell size is too small for micro-pipettes to perform a patch-clamp experiment. The use of chemicals such as proton carriers will eliminate the membrane potential but hardly reverse the process. Changing the external pH will change V_m directly. However, the internal pH homeostasis would maintain internal pH in a range that would compensate the V_m change. Berg's group has showed that the pH has a weak effect on motor speed in *E. coli* [Chen, 2000b].

Ion flux through the motor:

The ion flux through the bacterial flagellar motor has only once been measured successfully using *Streptococcus* cells [Meister, 1987]. The proton uptake rate by a population of cells in weak-buffered medium can be monitored by measuring external pH. The difference of the proton uptake rate between swimming cells and cells exhibiting suddenly stopping flagella is the proton flux associated with motor rotation. The motor can be stopped by adding anti-filament antibody to crosslink the filaments in the bundles. The estimated number is about 1200 protons per revolution per motor.

In the ion-driven F_o motor, the ion flux has been measured by a similar method. The major difficulty is estimating the number of functional F_o proteins, which causes the large variation of the estimated flux, from 70 $H^+/s/F_o$ to 10^5 $H^+/s/F_o$ [Franklin, 2004].

2-2-4 Models

Physical Model

Combining current knowledge of the BFM, torque is thought to be generated between the interface of the stator complex (MotA/B) and rotor protein (FliG). Due to the lack of detailed structural information of the motor, especially of stators, the microscopic mechanism of the torque generation remains unknown. For example, without the structure of stator complex, the ion transit process and binding site are unknown. Thus, current physical models are still conceptual rather than exact. A model must be constrained within the true motor performance such as torque output, energy consumption, switching behavior etc. Several models have been proposed such as 'Turnstile model', 'Turbine model' and 'Crossbridge model' [Berry, 2000].

In the turnstile model (Figure 2-8 (A)), ions from outside the cell are deposited onto the rotor by one ion-channel in a stator, and are carried by diffusion of the rotor to the second ion-channel on the stator that allows them to exit into cell [Khan, 1983]. The rotor is bound to a stator and unable to move unless ions arrived. In this model, the ion transition through the membrane and rotation of the rotor occur in separate steps. There is not sufficient structural information to support this model.

In the turbine model (Figure 2-8 (B)), ions pass through stator channel and interact with charges on the rotor which are distributed as tilted lines of positive and negative charges [Berry, 1993]. These electrostatic forces keep the line of negative charges close to the ion as it passes into the cell, which leads to rotation. In this model, the energy from the influx ions is directly coupled to the torque-generation, which is the 'power stroke' type of mechanism. However, the structure of the rotor is not known in sufficient detail to clarify the existence of the charge distribution on the rotor. In a switching event, either the ions must flow in the opposite direction or the tilt direction of rotor charge distribution must change.

Blair's group has proposed a cross-bridge model based upon current biochemical and structural knowledge of the BFM [Kojima, 2001], Figure 2-8 (C). In this model, the rotation is driven by cyclic conformational changes in the stator, which are related to

transition of one or more ions through the stator channels. For a cycle, the stator binds to the rotor, the ion energy is used to move the rotor forward, and the stator detaches the rotor and relaxes to its original conformation. For switching the rotation direction, the rotor proteins, FliG, must change their interaction with stators.

We cannot rule out any of these physical models due to the lack of the atomic structures of the motor. Further analysis of these models requires mathematical treatments to predict reasonable physiological performance such as the torque-speed relationship. Comparing these to experimental results can limit the models. On the other hand, new conceptual models may suggest the direction of experiments.

From the Physical Model to Mathematical Model:

A motor can be viewed as the motion in a multi-dimension space of potential and physical coordinates [Bustamante, 2001]. We do not have this detailed knowledge yet. However, a physical model can be represented by several key variables such as rotation angle and potential profiles. With a proper assumption of physical parameters and potentials of the motor, one can write down the equation of motion and make a simulation of the performance of the motor. Xing et al. present a simulation based on the cross-bridge model. The torque-speed relationship can be reproduced in this mathematical model [Xing, 2006].

A further simplification can be done by assuming the motor stays in only a few important states. The motor transits between these states and the properties can be represented by transition rate. This is a so called kinetic model. There are several examples of using a kinetic model to catch key aspects of the bacterial flagellar motor, see reference [Berry, 1999; Sowa, 2003].

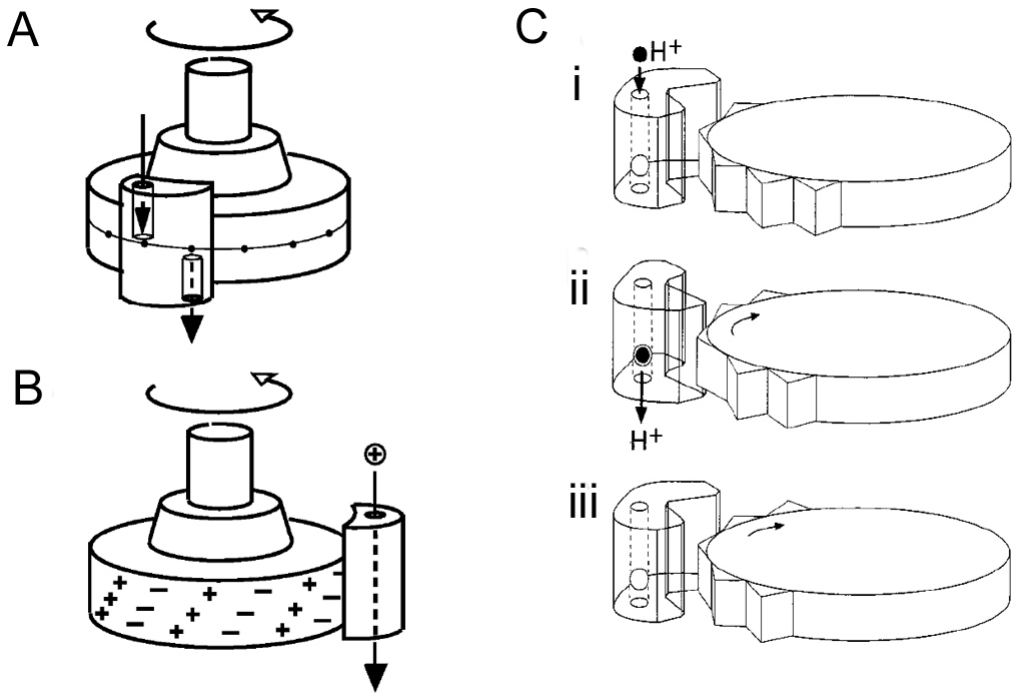

Figure 2-8: (A) Turnstile model. (B) Turbine model. (C) Cross-bridge model of bacterial flagellar motor torque generation. (i) Proper alignment of stator and rotor triggers the opening of the ion channel of stator. (ii) Ion binding to the Asp32 forces a conformational change and interacts with rotor to drive the rotation. (iii) The ion dissociates to the cytoplasm and the stator returns to the original state for the next cycle. Figure (A, B) and (C) is adapted from [Berry, 2000] and [Kojima, 2001].

2-3 *E. coli* and Chimeric Motors

History and aims of chimeric motors:

In the proton-driven motor, only MotA, MotB, and FliG are directly involved in the torque generation. Biochemical analysis suggests that $MotA_4MotB_2$ form a complex as a stator [Kojima, 2004]. In the *ΔmotAB E. coli* background, an inducible plasmid containing *motAB* can restore the motor speed in stepwise increments up to 11 levels. In

the sodium-driven motor, PomA, PomB, FliG, MotX, and MotY are essential for the torque generation. PomA and PomB are homologous to MotA and MotB. The C-terminus of FliG is important for the interaction with the stator complex while the N-terminus of FliG is essential for motor assembly. MotA and PomA have four transmembrane regions and a large cytoplamic loop. This cytoplamic loop is thought to interact with the C-terminus of FliG and generate torque. MotB has a large periplasmic domain that contains a sequence motif to bind peptidoglycan. The C-terminal domain of MotB is thought to be important for periplasmic membrane binding. The N-terminal domain of MotB has a transmembrane part to form an ion channel with MotA. In order to understand ion-conduction and ion selection, many experiments have been designed to construct hybrid or chimeric motors. These experiments are mainly focused on stator proteins (MotAB, PomAB) and the rotor protein (FliG).

Selectivity determinant:

(1) Hybrid motor

Homma's group has shown that a hybrid motor system consisting of MotA from proton-driven *Rhodobacter sphaeroides* and PomB, MotX, MotY from sodium-driven motor *Vibrio alginolyticus* can work using sodium ions in *Vibrio alginolyticus* host cells [Asai, 1999]. This result suggests that MotA and PomA cannot determine the ion selection.

(2) FliG chimeric motor example

A chimeric FliG (FliG-EV) protein composed of the N-terminal domain of *E. coli* FliG and C-terminal domain of *Vibrio cholerae* FliG can function in *E. coli* host cells [Gosink, 2000]. Also, the chimeric FliG (FliG-VE) protein composed of N-terminal domain of *V. cholerae* FliG and C-terminal domain of *E. coli* FliG can function in *V. cholerae* host cells. This suggests similar mechanisms of torque generation in these two strains, in which stators of one bacteria can interact with rotors of another bacteria.

(3) MotB chimeric motor

Homma's group has made a chimeric protein, MomB, which has the N-terminus of MotB (*Rhodobacter sphaeroides*) and C-terminus of PomB (*Vibrio alginolyticus*) [Asai, 2000]. MomB has the entire transmembrane part of MotB of a proton-driven motor and can

cooperate with MotA as a sodium motor in *Vibrio alginolyticus*. MomB can also cooperate with PomA as a sodium motor in *Vibrio alginolyticus*. These chimera motors indicate that the transmembrane part of MotB can not determine the ion selection.

(4) PotB chimeric motor

Another chimeric protein, PotB, with the N-terminal domain of PomB (*Vibrio alginolyticus*) joining to the C-terminal domain of MotB (*E. coli*) functioned with PomA as a sodium stator in *E. coli* without MotXY [Asai, 2003], Figure 2-9. This chimeric motor system suggests several important results. First, MotXY are not essential for the sodium driven motor. Second, the C-terminal domain of MotB, rotor, MotXY can not determine the ion selection.

All these hybrid and chimeric motors show the complexity of the ion selectivity and the functional similarity of the BFMs. In particular, no single component alone determines ion selectivity.

The new insight of PotB chimeric motor from a physicist's point-of-view:

Among all these chimera motors, one is very special and useful for further investigation: the chimeric stator comprising PomA and chimeric PotB proteins that can function as a sodium stator in wild-type *E. coli* host cells. In these sodium-driven *E. coli* cells, the motor speed is even faster than the wild-type proton-driven BFM of *E. coli*. We are interested in this chimeric motor for the following reasons. First, if the torque generation occurs at the interface of stator and rotor, it would be useful to know the torque-speed relationship of sodium-stator to proton-rotor. Torque-speed relationships of wild-type proton-driven motors of *E. coli* and sodium-driven motors of *V. alginolyticus* have been reported. Comparing these results would be informative.

Second, the sodium chimeric motor in *E. coli* is driven by sodium-motive force while proton-cycle plays a major role in *E. coli* energetics. We can simply take away sodium ions from the medium and the cells can maintain cellular functions but motors stop. Third, because the smf comprises of contributions from both the membrane potential and sodium gradient across the membrane, it is possible to manipulate smf to control the BFM and to study the sodium energetics of *E. coli*.

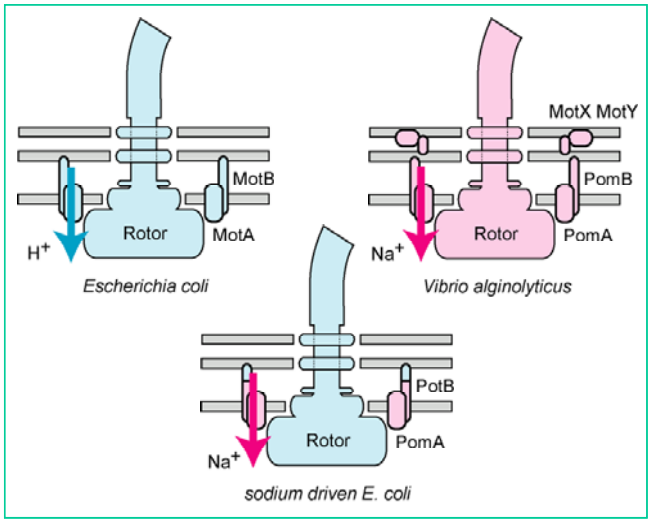

Figure 2-9: Schematic illustration of a chimeric flagellar motor in *E. coli*. In wild-type *E. coli*, the proton stators are formed by MotA/MotB and interact with the rotor. In *V. alginolyticus*, the sodium stators are formed by PomA/PomB and extra MotXY proteins are required for the motor function. A chimeric PotB protein has the N-terminal domain of PomB fused in frame to the periplasmic C-terminal domain of MotB. In *ΔmotaA/B E. coli* background, the expression of PomA and PotB can restore the rotation. This chimeric motor is driven by sodium ions in *E. coli* without MotXY. (Figure courtesy of Sowa, Y.)

Direct Observations of Steps in BFM Rotation:

From the structural knowledge of the bacterial flagellar motor, one would speculate that the fundamental motion is stepwise rotation. This stepwise rotation had not been observed for thirty years because the BFM rotates at several hundred hertz with many stators. Using the sodium chimeric motor in *E. coli*, for the first time we can observe stepwise rotation in the BFM. Rowe and Sowa used two different methods to perform this observation. Precise observation of the motor can be made by attaching sub-micron polystyrene beads to the truncated flagellum. High speed back-focal-plan (BFP) interferometry using a 1064 nm laser can measure 0.5 μm beads with sufficient angular

resolution, Figure 2-10 [Sowa, 2005; Rowe DPhil Thesis]. A fluorescence microscope with a high-speed sensitive CCD can measure 0.2 μm fluorescence beads. The latter method has greater laser damage to the cell due to the use of a blue light for fluorescence excitation. Applying a very low sodium concentration (0.1 mM) in the medium to the chimeric motor in *E. coli* cells, motor speed can be slowed and then stopped. Steps in rotation can be observed during this transit time. However, the motor is not stable in these low sodium conditions. Also, the stator number and sodium motive force are unknown. Thus we cannot give further physical and statistical results from this data.

Our Goals for the Chimeric Motor:

The direct observation of steps bacterial flagellar motor with sodium chimeric stator is a milestone [Sowa, 2005]. To make further progress, the fundamental understanding of sodium-energetics of the chimeric motor should be gained first. We also need a clear picture of how we can control and manipulate the motor speed to reach stable conditions for step observation. Additionally, how the extra sodium influx affects *E. coli* is another interesting bio-energetics questions. Due to the lack of proper methods to measure single cell sodium motive force, we decided to develop new methods to investigate intracellular sodium concentration and membrane potential in single cells. Two fluorescence measurements of intracellular sodium concentration and membrane potential of single bacterial cell were developed during my DPhil.

Single BFM speed measurements can probe the motor function in different smf and various loads. Two major goals are the torque-speed relationship and speed-smf relationship of the chimeric BFM. It is hoped that this fundamental knowledge will enable a better understanding of the characteristics of this chimeric system.

Our ultimate goals for the chimeric motor are fully controlling the motor rotation and understanding the motor mechanism through the stepwise rotation. We need to control stator number and motor speed in low load conditions. All this background knowledge for future step observations was learned in this thesis. Preliminary results of step

observation in stable rotation are also presented at the end of this thesis. Table 2-2 lists basic and important *E. coli* information of this study [Berg, 2003].

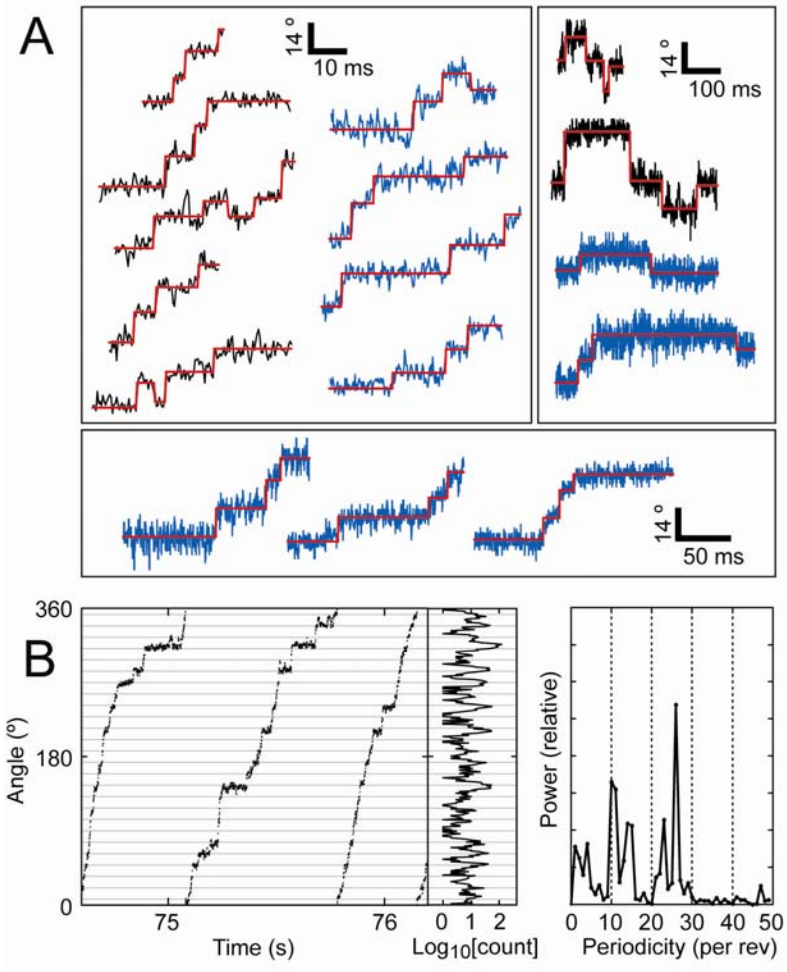

Figure 2-10: Stepwise rotation in BFM. (A) Selections of rotation traces from BFP (blue trace) and fluorescence experiments (black traces) with step-finding algorithm output (red lines). The step size is ~ 14°. (B) An angle vs time trace of a 200 nm bead on the motor. A histogram of dwell angle and the power spectrum of that histogram are also shown. A peak at 26 per revolution corresponding to a step size of 13.8°. Figure is adapted from [Sowa, 2005].

Table 2-2 Specification of *E. coli*	
Cell width	0.8 - 1 μm
Cell length	2 - 3 μm
Number of flagella	4 - 8
Membrane potential (pH_{ex} 7)	(-120) – (-140) mV
pH_{in} (at pH_{ex} 7)	7.6 – 7.8
ΔpH	0.6 (-35 mV) – 0.8 (-47 mV)

2-4 Research Techniques

2-4-1 Motor Speed Measurement

In the past three decades, several different experimental methods have been developed to measure bacterial flagellar motor speed. They can be classified into three methods. First, a common technique which allows direct observation of the rotation by tethering the BFM filament to the glass surface using antibodies [Silverman, 1974], Figure 2-11 (A). The motor is working against very high viscous load and can rotate at only a few Hz. Thus, speed measurement can be made by video imaging. However, because the motor position is randomly distributed, the viscous drag coefficient of rotation is different from cell to cell and there will be a correspondingly large error in the estimation of viscous drag.

Second is the laser dark field method, Figure 2-11 (B). The cell could be immobilized on glass or be free swimming [Magariyama, 1995]. The motor is working in natural and low viscous load conditions. The fastest bacterial flagellar motor record was measured by this method in *V. alginolyticus* cell in 35^{o} C. In this method, the angle resolution is not possible.

Third is so called bead-assay in which cells are immobilized on glass and a known size of polystyrene beads attached to the truncated flagellar filaments [Ryu, 2000; Sowa, 2005]. The motor speed can be measured by recording bead movement either by the BFP interferometry (see Chapter 3) or fluorescence microscopy (using fluorescent beads). The viscous load can be varied by using difference sizes of beads. In the fluorescent beads speed measurement, CCD frame rate and laser damage are the major concerns. In the BFP experiment, the laser wavelength constrains the bead size. In this thesis, we measured motor speed by beads assay with the BFP speed measurement.

2-4-2 Fluorescence Microscopy

Fluorescence labelling of specific molecules and specific ion sensitive fluorophore has proved extremely useful in many fields. Gene engineering can also provide specific fluorescent proteins connected to target proteins allowing precise molecule tracking. In excitable cells, ion channels control the ion flux and membrane potentials. Using calcium sensitive fluorophores, the spatial distribution of calcium within the cell can be observed. Also, several new fluorescence techniques have been introduced to study biophysical questions such as Total-internal-reflection fluorescence (TIRF), Forster resonance energy transfer (FRET) and fluorescence recovery after photobleaching (FRAP). In this thesis, we measure intracellular sodium concentration and membrane potential by using a sodium sensitive dye (Sodium Green) and Nernstian dye respectively.

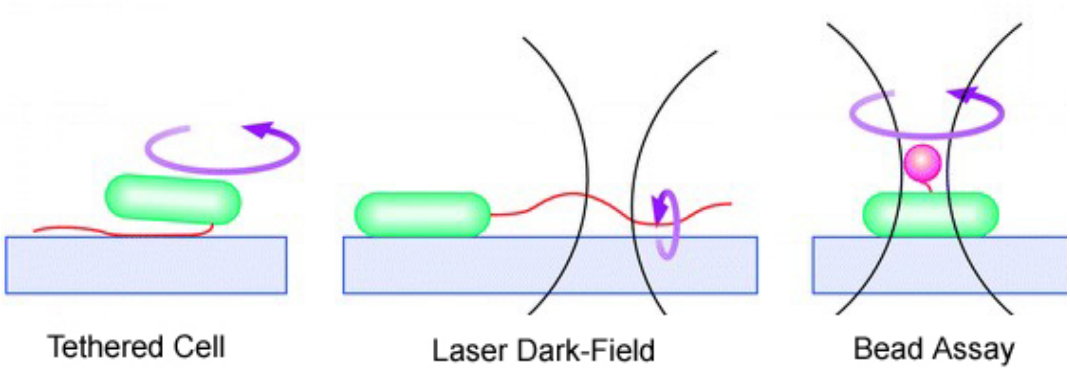

Figure 2-11: Speed Measurement Methods. In the tethered cell method, the motor operates in high load and motor speed is up to 20 Hz only. In the laser dark-field method, fast rotation can be observed. In the bead assay, viscous load can be controlled by using different sizes of bead attached to motors. With BFP speed measurement, the motor rotation rate and radius can be recorded. Figure is adapted from [Berry, 2005]

CHAPTER 3

EXPERIMENTAL TECHNIQUES

The results discussed in this thesis were obtained using a fluorescence microscope to measure membrane potential and intracellular sodium concentration and back-focal-plane interferometry to measure single motor speed. The strains used in this thesis were YS34 [Sowa, 2006; Asai, 2003] with different inducible stator plasmids, listed in Table 3-1. YS34 was derived from strain RP4979 (*ΔcheY*) [Scharf, 1998] thus the motor rotates counterclockwise exclusively.

While the principle ideas of fluorescence microscopy and back-focal-plane interferometry are quite simple, our experimental aims require a customized setup for the single cell measurements. The first section will focus on the design and usage of fluorescence microscopy and the second on back-focal-plane interferometry. The third section contains a description of the bacterial strains, growing conditions and sample preparations.

3-1 Fluorescence Microscopy

The single-cell fluorescence measurements in this thesis were measured in a custom-built fluorescence microscope (designed and built by M. Leake and R. Berry). The design of the fluorescence microscope was optimized for single bacterial cell fluorescence

observation and single molecular measurements including epi-fluorescence mode, total internal reflection fluorescence mode and photo-bleaching recovery mode. In this thesis, we mainly use epi-fluorescence mode.

3-1-1 Apparatus

We used a custom-built inverted fluorescence microscope (see Figure 3-1) with a Plan Fluor 100×/1.45 oil immersion objective (Nikon UK Ltd., Kingston-upon-Thames, UK) and a xyz nanopositioning stage (E-503.00, Physik Instrumente, Germany). A tungsten halogen lamp was used for low-intensity brightfield illumination. For intracellular sodium concentration measurements, Sodium Green was excited in epi-fluorescence mode at 488 nm by an Ar-ion Laser (Melles Griot, Carlsbad CA) via a filter (475 nm bandpass) and a dichroic mirror (505 nm long-pass). For membrane potential measurements, the TMRM dye was excited in epi-fluorescence mode at 532 nm by a Diode Pumped Solid State Laser (LCMT111-20, Laser2000, Northants, UK) via a dichroic mirror (530 nm long-pass). The total illuminated area was $(20\ \mu m)^2$ and the illumination intensity at the sample was varied in the range 7-19 W/cm^2 (± 2 %) for Sodium Green and ~ 5 W/cm^2 (± 2 %) for TMRM. Fluorescence emission was passed through a dichroic mirror, an emission filter (535 nm band-pass for Sodium Green, 580 nm band-pass for TMRM) and a notch rejection filter (488 nm for Sodium Green, 532 nm for TMRM). Images (128x128 pixels, ~6x6 μm) were acquired using a back-illuminated Electron Multiplying Charge Coupled Device (EMCCD) camera (iXon DV860-BI, Andor, Belfast UK). Each image takes 1 second exposure for Sodium Green and 10-30 ms exposure for TMRM. All experiments were performed at 23^oC.

3-1-2 Fluorescence Images Acquisition

Fluorescence Intensity Measurements:

This section aims to describe the general method we used for calculating the fluorescence intensity of a single cell (or single object) from the fluorescence images. Images of each cell were taken at the middle height of the cell.

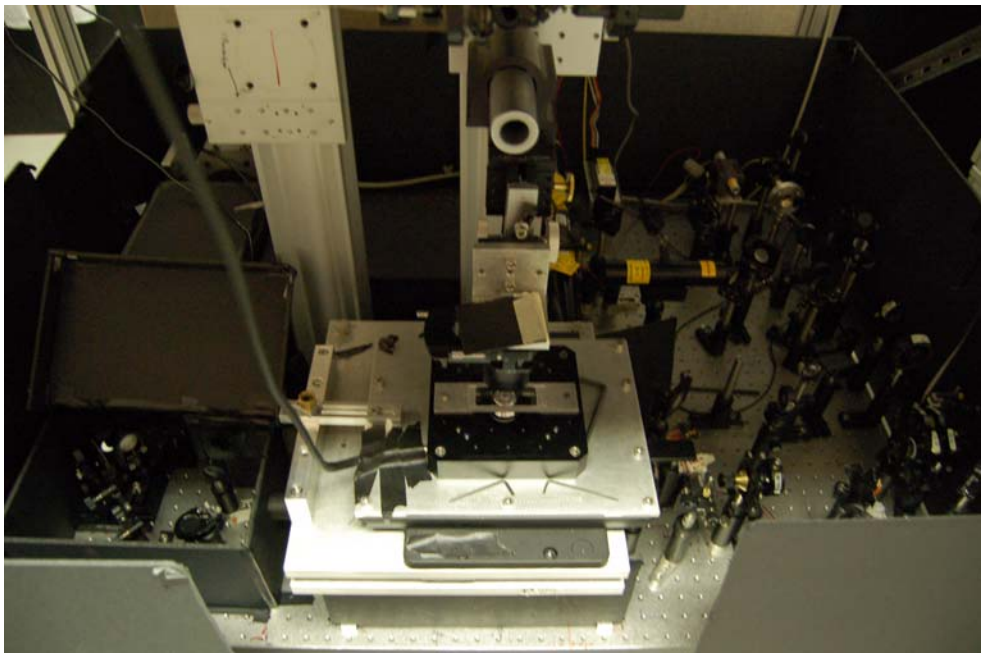

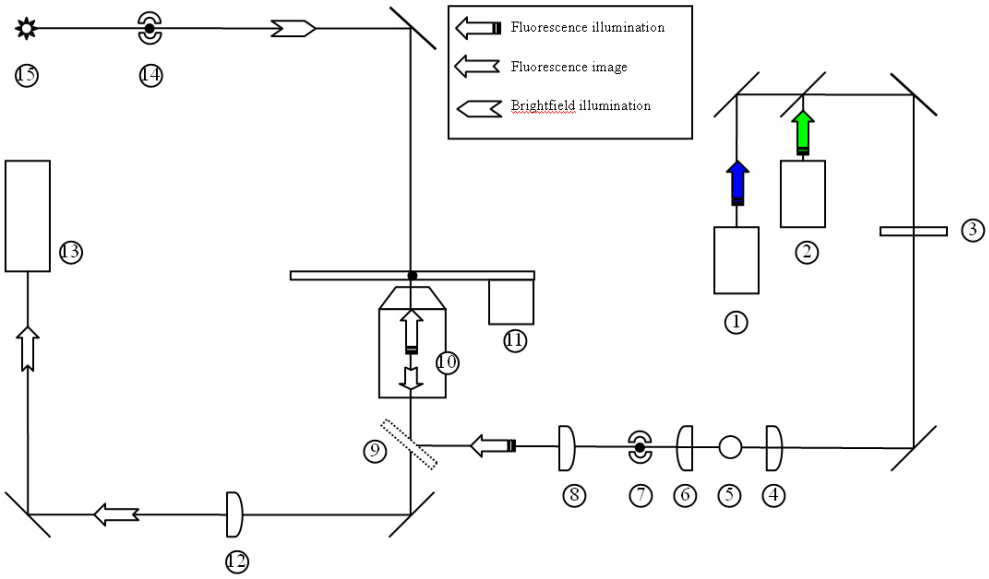

Figure 3-1: Schematic Diagram of Fluorescence Microscope. (1) 488 nm Laser. (2) 532 nm Laser. (3) Neutral density filter. (4, 6, 8) Lens. (5) Electrical Shutter. (7) Field iris. (9) Dichroic mirror. (10) Objective. (11) Piezo-electric stage. (12) Lens. (13) EMCCD. (14) Field iris. (15) Tungsten halogen bulb.

Figure 3-2 (A) and (B) show typical brightfield and fluorescence images respectively of a single *E. coli* cell loaded with Sodium Green. Figure 3-2 (C) shows the fluorescence image divided into three areas: white, background region ($I < T_{bg}$); red, marginal area ($T_{bg} < I < T_{cell}$); yellow, cell area ($I > T_{cell}$), where I is pixel intensity. Figure 3-2 (D) shows the pixel intensity histogram, including the thresholds T_{bg} and T_{cell} and a Gaussian fit to the lower half of the background peak. The average fluorescence intensity was calculated as

$$F = \left\langle I - I_{bg} \right\rangle_{I>T_{cell}}, \tag{3-1}$$

where I_{bg} is the average background intensity and T_{cell} is the threshold intensity defining the central part of the cell image. Smaller cells will have a relatively larger marginal area and thus a lower average intensity if the entire cell image is included; by measuring the average pixel intensity of the central part only, ignoring the marginal area of the cell, our fluorescence signal is less sensitive to cell size. The main peak in the histogram of pixel intensity contains mostly background and some marginal area. I_{bg} is obtained by fitting the number of pixel values less than the peak value with the Gaussian function, $g(I) = A_0 e^{-\frac{(I-I_{bg})^2}{2A_1^2}}$, as shown in Figure 3-2 (D). To define T_{cell} first we define an upper threshold for the background, $T_{bg} = I_0$, where I_0 is the smallest I for which $I > I_{bg}$ and $g(I) < 1$, and then $T_{cell} = (I_{max}+T_{bg})/2$. Figure 3-2 (E) shows the image intensity profile along the x-axis indicated in Figure 3-2 (B).

3-2 Laser Trap and BFP rotation measurement

3-2-1 Laser Trap

The Basic Principles and Idea of an Optical Trap:

By focusing a laser beam down to a diffraction-limited spot, a laser trap can be made to hold a micron size dielectric particle at a fixed point in three dimensions. The laser beam is focused to the diffraction limit using a high numerical aperture (NA > 1) microscope objective lens. A dielectric particle with a refractive index greater than the medium faces a potential well close to the focus spot. Due to the gradient of the focused light, the

particle scatters more photons in the direction away from the beam center and the net force is always towards the beam center unless the particle is just in the middle of the focused laser beam, see Figure 3-3.

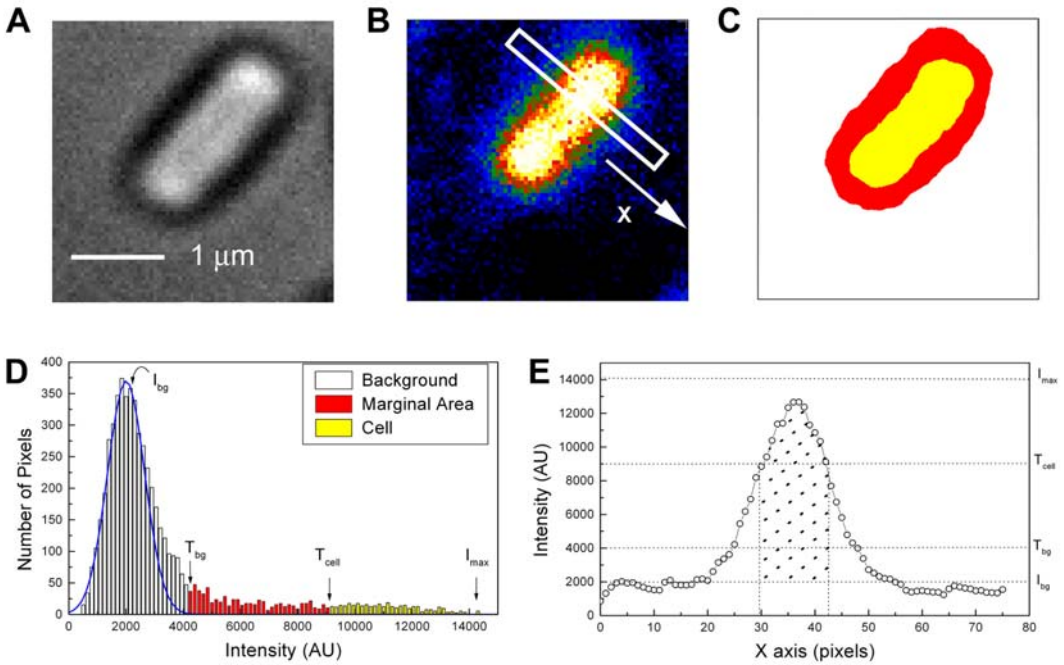

Figure 3-2: Images and Fluorescence Intensity Calculation. (A) Typical brightfield image of a YS34 *E. coli* cell. (B) Sodium Green fluorescence image of the same cell. Laser power 7.35 W/cm^2, exposure time 1 s. (C) The fluorescence image is divided into three regions: white, background region; red, marginal area; yellow, cell area. (D) Pixel intensity histogram illustrating the method of determining the different image regions used to obtain the Fluorescence signal. See text for details. (E) An image intensity profile along the x-axis in (B) (average of five pixel lines). The shaded area contributed to the fluorescence intensity signal.

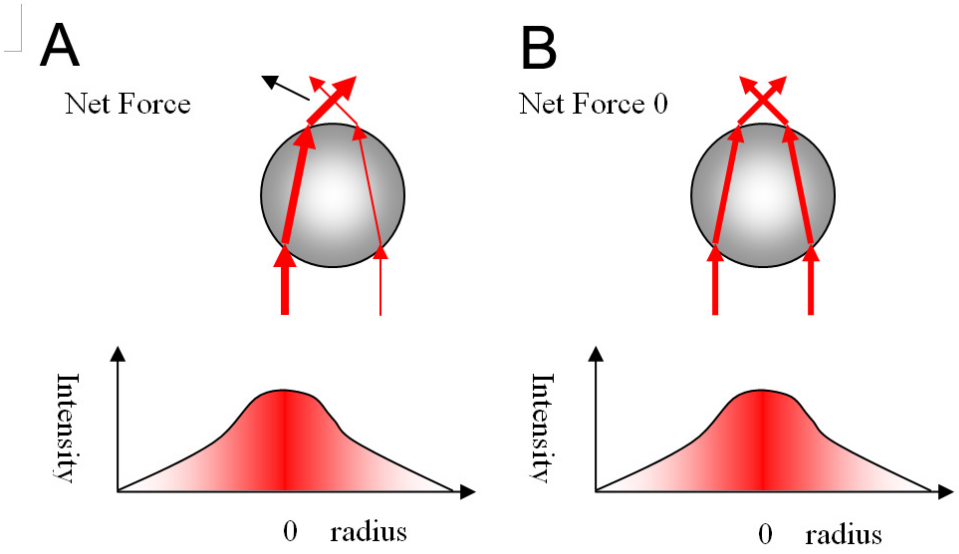

Figure 3-3: Optical trap, ray optic illustration. (A) A particle near the center of laser beam focus. The deflected beam is stronger on one side and as a result the restoring force is to the left hand side and pushing the particle back to the center of the laser trap. (B) The particle in the center of the laser trap. The net force is zero in the xy plane.

Laser traps have been used for non-invasive manipulation of cells and viruses. More recently, they have been extensively employed in the investigation of molecular motors due to their working range of pico-Newton forces and nanometer positioning. In this thesis, we used a weak trap for position detection rather than applying force to the particles. The displacement of the particle from the center of the trap can be measured by the deflection of the trap beam [Ryu, 2000; Rowe, 2003]. In this method, the transmitted laser beam is collimated by a condenser lens and the back-focal-plane of the condenser is imaged onto a quadrant photodiode.

3-2-2 BFP Rotation Measurement

Apparatus:

In this thesis, we used a custom-built inverted microscope and a single beam and single-focused laser trap for bead position detection, Figure 3-4 (designed and built by Pilizota and Berry). The microscope consists of an oil-immersion NA. 1.4 objective (CFI plan-fluo 100x, Nikon, Japan) and a 3-axis piezo-electric stage. A tungsten halogen lamp was used for low-intensity brightfield illumination. For the experiments with bead size larger than 0.5 μm, a diode-pumped solid-state laser (Elforlight, Northants, UK) with 1064 nm wavelength beam was used for the bead position detection. For other experiments, a helium-neon laser (Coherent, USA) with 632 nm beam was used. The laser power can be varied by passing different neutral-density filters. The focused beam at the image plane forms the weak trap.

The transmitted beam is collimated by a condenser lens, and the condenser back-focal-plan is imaged to fill the surface of a quadrant photo-diode (Pin-SPOT 9DMI, UDT Sendors, CA, USA). The photo-current from each quadrant is amplified using a home-made current-to-voltage amplifier. A PC with A/D card (National Instruments) can acquire the voltage from the diode at up to 20 kHz.

The coordinate of the trapped beads deflected in the x direction *Px* and y direction *Py* are calculated as

$$P_x = \frac{(V_a + V_b) - (V_c + V_d)}{V_a + V_b + V_c + V_d}, \tag{3-2}$$

$$P_y = \frac{(V_a + V_c) - (V_b + V_d)}{V_a + V_b + V_c + V_d}, \tag{3-3}$$

where, V_a, V_b, V_c, and V_d are the acquired voltages from the 4 quadrants of the diode.

Rotation and Speed Measurement:

For the bacterial flagellar motor speed measurement, P_x and P_y are combined to form a complex signal $P_z = P_x + iP_y$. For stable rotation at frequency ω, the Fourier power spectrum of P_z has a single peak at frequency $+\omega$. Figure 3-5 (A) shows the typical P_x and P_y data of a 0.2 μm polystyrene bead attached to a sheared flagellum using the

632 nm wavelength laser. Figure 3-5 (B) shows the complex power spectrum of P_z of the same signal with a peak at 600 Hz.

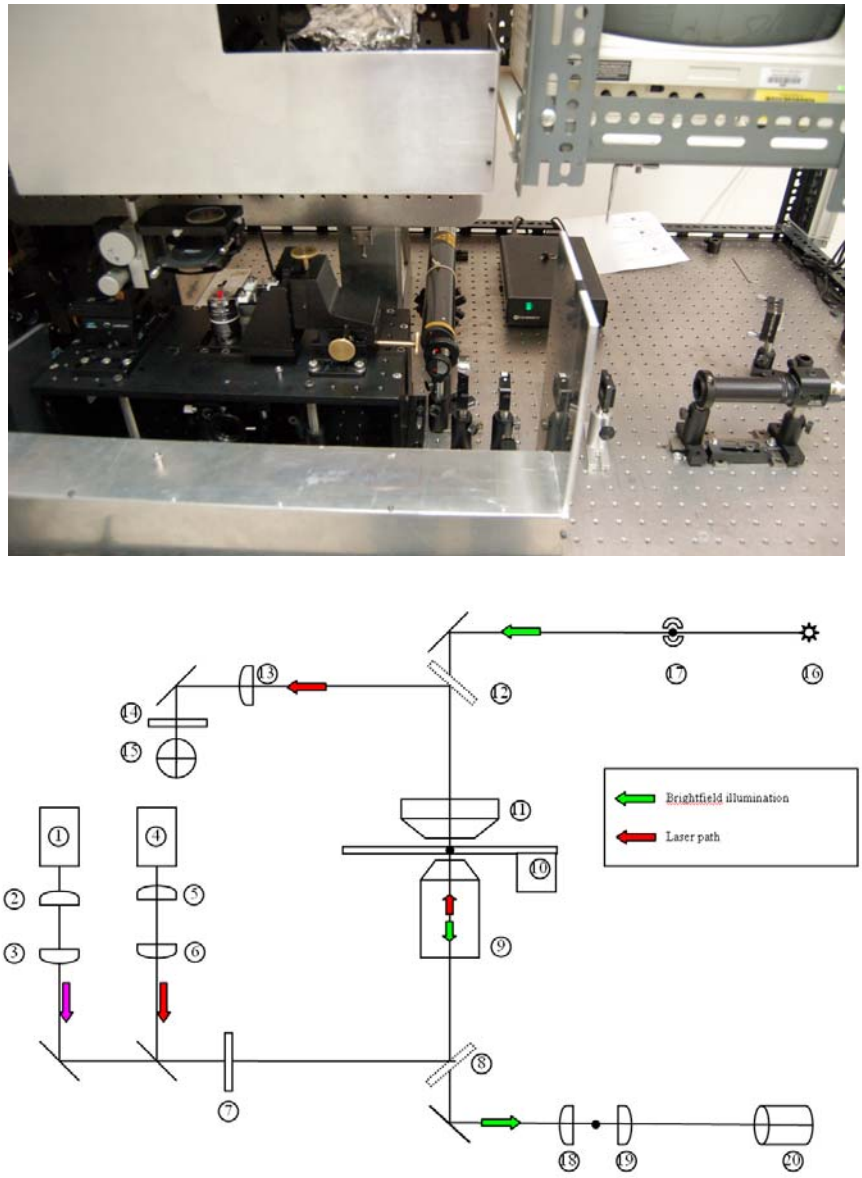

Figure 3-4: Schematic Diagram of Laser trap and BFP measurement. (1) 1064 nm Laser. (4) 632 nm Laser. (2, 3, 5, 6) Lens. (7) Neutral density filter. (8, 12) Dichroic mirror. (9) Objective. (10) Piezo-electric stage. (11) Condenser. (13) Lens. (14) Filter (15) QPD. (16) Tungsten halogen bulb. (17) Filed iris. (18, 19) Lens. (20) CCD.

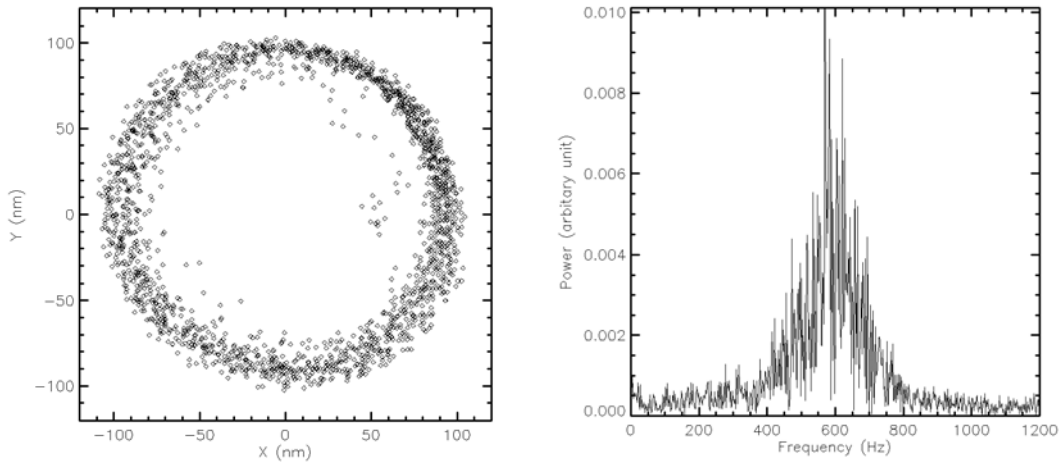

Figure 3-5: Motor speed measurement. A 0.2 μm bead attached to the truncated flagellar filament of YS34 cells with fully-induced PomA/PotB stators. (A) QPD xy data sampled at 10k Hz and (B) raw complex power spectrum with peak ~ 600 Hz.

Laser Damage:

The drawback of the laser trap is the optical damage to the biological sample. Infra-red wavelengths, 1064 nm in our case, are chosen for the low level of photodamage [Neuman, 1999]. However, sensitivity of the BFP measurement is limited by the wavelength of the laser. Smaller beads required a shorter wavelength laser to achieve high angular resolution. For beads smaller than 0.5 μm, we used a HeNe laser of wavelength 632 nm to perform the back-focal-plane position detection. The laser damage can be quantitatively measured by monitoring motor speed under continued laser illumination. For the 1064 nm wavelength laser, the speed slows down by an amount of ~0.01% per second per mW laser [Rowe, DPhil thesis]. In our measurement condition, with a laser power of 200 μW, the time for the motor slowing down by 10% is 83 min. For the 632 nm wavelength laser, the motor speed slows down steadily by an amount of ~1.88% per second per mW. For speed measurements, 10 μW laser power is sufficient. For high angle-resolution experiments, we use laser power of 88 μW, the time for the motor

slowing down by 10% is ~60 s. The motor speed in general has 5% fluctuation. Figure 3-6 shows a typical case of motor speed slowing down by laser illumination.

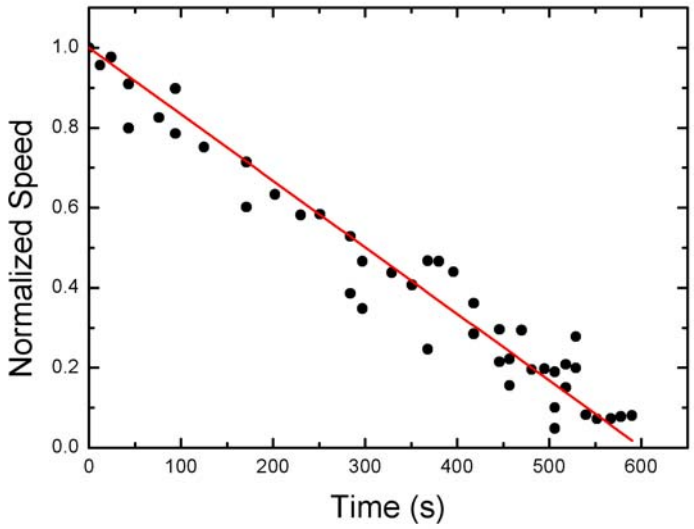

Figure 3-6: Single motor speed slowing down by 632 nm wavelength laser. The laser power is 88 μW.

3-3 Cells and Cultures

3-3-1 Bacteria strains

Chimeric strains were originally made in Homma's group for the understanding of ion selection of the motor [Asai, 2003]. The YS34 strain with proper plasmids for the speed assay was made in Nagoya University by Sowa and brought to Oxford in 2003. Table 3-1 lists the strains and plasmids used in my thesis.

3-3-2 Growing Condition

Cells were *E. coli* strain YS34 (*ΔcheY, fliC::Tn10*, *ΔpilA*, *ΔmotAmotB*) with plasmid pYS11(*fliC* sticky filaments) and a second plasmid for inducible expression of stator

proteins. Chimeric stator proteins were expressed from plasmid pYS13 (*pomApotB7*^{E}), induced by isopropyl-ß-D-thiogalactopyranoside (IPTG). *CheY* deletion ensures the motor rotates counterclockwise exclusively. The filament is replaced by a sticky filament for the bead assay. *PilA* deletion decreases the cell membrane surface interaction with the beads. The stator genes, *MotA* and *MotB*, are also deleted. Wild-type stator proteins were expressed from plasmid pDFB27 (*motAmotB*), induced by arabinose. Cells were grown in T-broth [1% tryptone (Difco, Detroit, MI), 0.5% NaCl] containing IPTG (20 μM) and arabinose (5 mM) where appropriate at 30 °C until mid-log phase, harvested by centrifugation and sheared as through gauge 26 needles fifty times to truncate flagella. The bacteria were washed three times at room temperature by centrifugation (2000 × g, 2 min) and resuspended in sodium motility buffer (10mM potassium phosphate, 85mM NaCl, 0.1mM EDTA, pH 7.0).

Table 3-1. Strains and plasmids

Strains	Relevant genotype/phenotype	Reference
YS34	*ΔcheY, fliC::Tn10*, *ΔpilA*, *ΔmotAmotB*	[Sowa, 2005]
Chimera	*YS34, pYS11, pYS13*	[Sowa, 2005]
MotAB	*YS34, pDFB27, pFD313Cm*	[Reid, 2006]
Plasmids		
pYS11	*fli*Cst, Ap^{R}	[Sowa, 2005]
pYS13	P $_{LAC}$*pomApotB*, Cm^{R}	[Sowa, 2005]
pFD313Cm	*fli*Cst, Cm^{R}	[Reid, 2006]
pDFB27	P $_{ARB}$*motAmotB*, Ap^{R}	[Reid, 2006]

3-3-3 Sample Preparation and Flow-Cells

For measurements without medium-exchange, the cells were loaded into a simple custom-built flow-cell (a double-sided-tape-sealed chamber), Figure 3-7 (A). For the measurements regarding fast medium exchange, a flow-cell with 2-5 connected pipes was used, Figure 3-7 (B, C). For the experiments regarding more solutions, a flow-cell with one pipe connected to a changeable syringe reservoir was used. The time needed to change the medium of the chamber is about 5 s for multiple pipes and ~2 min for single pipes.

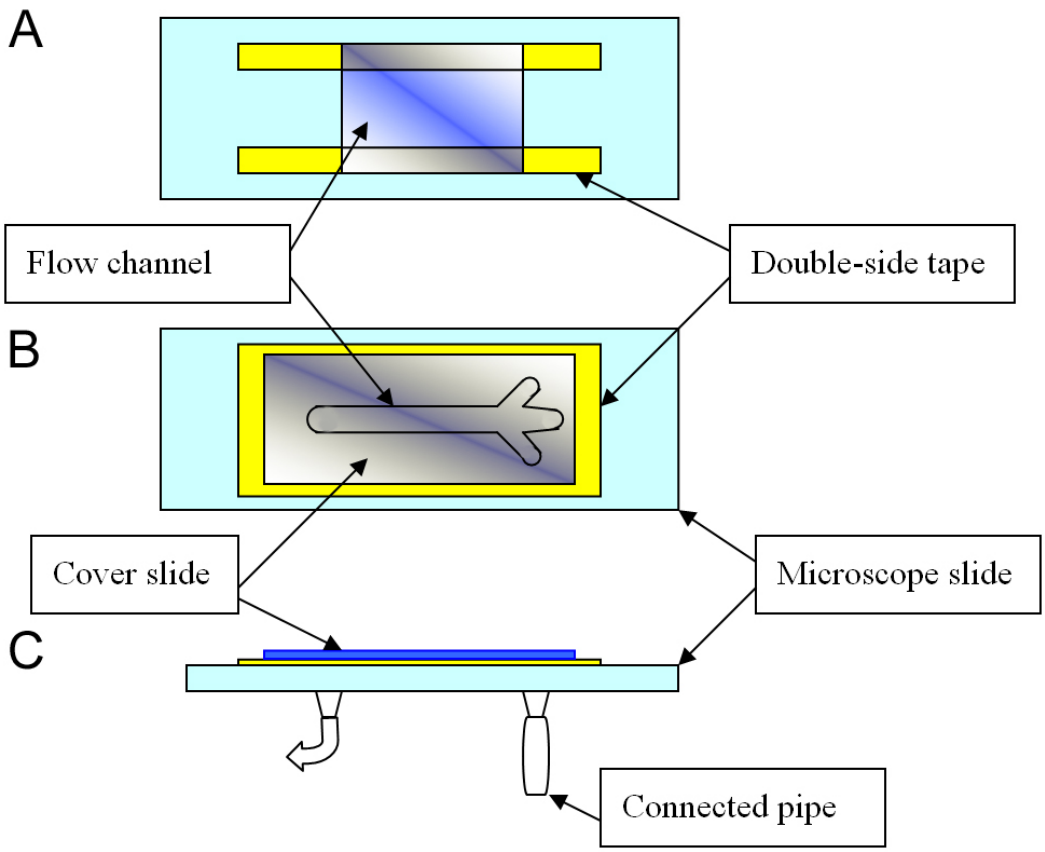

Figure 3-7: Illustrations of two different types of flow-cell. (A) Simple flow-cell with double-sided tape. (B) Multi-piped flow-cell for fast medium exchange. A microscope slide has holes drilled and connected with pipes. The flow channel was drawn by cutting double-sided tape and covered by a cover-slide. (C) Side view of (B).

3-3-4 Bead Assay

In order to achieve a high accuracy speed measurement in different load conditions, bead assays and BFP measurements were carried out (see Chapter 2-4 for the illustration and introduction of the bead assay). The protocol is as follows:

Flow-cells were treated with 0.1 % polylysine solution for 30 s and then washed with motility buffer (200 μL). Cells were then injected into the flow-cells and wait for 15 min. Beads (1 μm, 0.75 μm, 0.5 μm, 0.35 μm or 0.2 μm) were then loaded into the flow cells. Simple flow-cells were sealed by vacuum grease to avoided evaporation. Multiple pipe flow cells were connected with different media according to the experiment's design.

CHAPTER 4

SINGLE CELL INTRACELLULAR SODIUM MEASUREMENTS

4-1 Introduction

The BFM is driven by either proton (H^+) or sodium ions (Na^+). *E. coli*, *Salmonella typhimurium* and *Bacillus subtilis* have proton-driven motors [Blair, 1990; Shioi, 1980]. The polar flagella of *Vibrio alginolyticus* and *Vibrio cholerae* have sodium-driven motors [Yorimitshu, 2001; McCarter, 2001]. The chimeric stators (PomA/PotB) support sodium-driven motility in *⊿motA/motB E. coli* with a swimming speed higher than the original MotA/MotB stators. To investigate the motor mechanism and its dependence on sodium-motive force (smf) we have developed a method for rapid measurement of internal sodium concentration ($[Na^+]_{in}$) in a single *E. coli* cell that is compatible with simultaneous speed measurements of the flagellar motor. Dye toxicology, motor stability, experimental limitation and best conditions of experiments were all investigated with care. Thus, we can measure sodium chemical potential *⊿pNa* of single *E. coli* cells and use it to investigate the response of $[Na^+]_{in}$ to $[Na^+]_{ex}$ in *E. coli* strains expressing either PomA/PotB, MotA/MotB or no stator proteins. Also we measure *⊿pNa* in different $[Na^+]_{ex}$ and pH_{ex} conditions for the investigations of motor energetics in Chapter 6.

Other methods of $[Na^+]_{in}$ measurement:

$[Na^+]_{in}$ has been measured in *E. coli* by flame photometry [Epatein, 1965], ^{22}Na uptake in inverted vesicles [Reenstra, 1980], and ^{23}Na NMR spectroscopy [Nagata, 1995; Castle, 1986]. Other techniques have been reported to measure $[Na^+]_{in}$ in eukaryotic cells, for example flow cytometry of hamster ovarian cells [Amorino, 1995] and fluorescence spectroscopy of sea urchin spermatozoa [Rodrigues, 2003]. However, these methods measure ensemble averages from large numbers of cells using a static environment. For fast, dynamic single cell measurements we have devised a method based on the sodium-ion fluorescence indicator dye, Sodium Green [Amorino, 1995; Molecular Probes].

4-2 Materials and Methods

4-2-1 Sodium Green

The chemical structure of Sodium Green:

Sodium Green is a sodium sensitive fluorescent dye that can be excited by green light (excitation spectrum peak at 507 nm). We used the cell permeant form of Sodium Green (S-6901, Molecular Probes) with a clever design of cellular sodium concentration measurement, Figure 4-1 (A). The dye will freely diffuse across cell bilayer membranes. Once inside the cell, intracellular esterases cleave off the acetate moieties to convert the dye molecules into the sodium responsive acid form. The negatively-charged groups of the acid form prevent leakage from the cell. The dye molecule consists of a sodium binding site and fluorophore, connected with a spacer. In this system the electron lone pair on the nitrogen atom acts as a donor to quench the emission of the fluorophore. Once the sodium ion binds, it will reduce the delocalization of the electron pair to the fluorophore and quenching. Thus the fluorescence emission increases, Figure 4-1 (B).

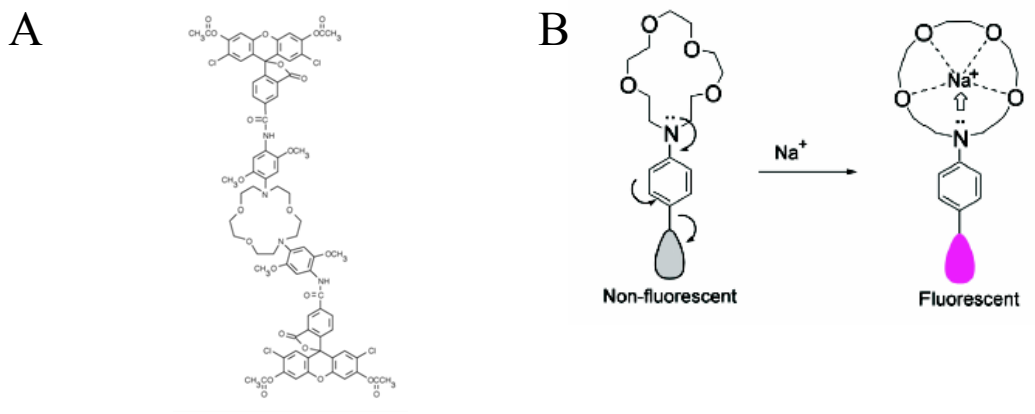

Figure 4-1: (A) Sodium Green molecular structure. (B) Smart dye mechanism. Figures are adapted from Molecular Probes web site.

4-2-2 Increasing Membrane Permeability

E. coli are gram-negative bacteria with an outer membrane containing lipopolysaccharide (LPS) that acts as a barrier to hydrophobic molecules such as Sodium Green. We investigated conditions for loading cells with the dye, choosing a balance between a sufficient fluorescence signal for single-cell measurements and minimal damage to the cell caused by disruption of the LPS.

There are many reports of increasing membrane permeability of bacteria [Vaara, 1992]. Many of them intend to weaken, or even kill bacteria for the food and animal husbandry industries. Here we apply a classical and mild method using ethylenediaminetetraacetic acid (EDTA) that chelates divalent cations that stabilize molecular interactions in the outer membrane and thus LPS will be released. We examined EDTA treating time and concentration for the best loading condition concerning fluorescence intensity and cell damage. For an EDTA concentration higher than 100 mM, even with short treating time of 10 min, many cells show unstable rotation. For the concentration lower than 0.1 mM, the membrane permeability would not increase. Thus, we decided to use 10 mM with a short treating time of 10 min. After this EDTA treating, the motors of these cells can rotate as stably as before.

4-2-3 Loading Protocol

Dye Loading:

Cells were attached to polylysine-coated coverslips in custom-made flow-chambers (volume ~5 μl) which allowed complete medium exchange within 5 s (see Chapter 3-3-3). For the speed measurement, polystyrene beads (0.97 μm diameter, Polysciences, Warrington PA) were attached to flagella as described [Ryu, 2000; Sowa, 2006].

Cells were suspended in high EDTA motility buffer (sodium motility buffer plus 10 mM EDTA) for 10 min (in order to increase the permeability of the outer LPS membrane), washed three times in sodium motility buffer and resuspended at a density of 10^8 cells/ml in Sodium Green loading buffer (sodium motility buffer plus 40 μM Sodium Green (Molecular Probes, Inc., Eugene, OR)) and incubated in the dark at room temperature for 30 min. Cells were washed three times and resuspended in sodium motility buffer, to remove excess Sodium Green. Sodium Green was added to sodium motility buffer as a stock solution of 1 mM dissolved in dimethyl sulfoxide (DMSO).

Fluorescence Intensity and Motor Stability:

Figure 4-2 shows the fluorescence intensity of *E. coli* after different incubation times in 40 μM Sodium Green loading buffer. Each point is an average of ten cells for which fluorescence was measured immediately after loading. We selected 30 min as the optimal loading time. Under this loading condition the fluorescence signal is more than 5 times the background, and measurements of flagellar rotation indicated that the motor and smf are unaffected by the dye, Figure 4-3. The mean and standard deviation of measured speeds of a 0.97 μm bead attached to a motor were determined for each of 28 loaded and 26 non-loaded cells in 85 mM Na^+. For loaded cells the average mean speed was 89 ± 6 Hz and the average speed deviation was 1.8 ± 0.6 Hz, indistinguishable from the corresponding values, 90 ± 7 Hz. and 2.1 ± 0.9 Hz respectively, for non-loaded cells. Only a small increase in fluorescence intensity is seen for incubation times between 30 min and 50 min in 40 μM Sodium Green. For incubation times longer than 60 min we observed differences between cell shapes in fluorescence and brightfield images, consistent with broken cells from which the cytoplasm was leaking activated

fluorophores. Concentrations above 40 μM increased the number of broken cells for a given loading time > 60 min. Shorter loading times and/or lower concentrations of Sodium Green gave reduced fluorescence intensity and thus more noisy measurements of $[Na^+]_{in}$.

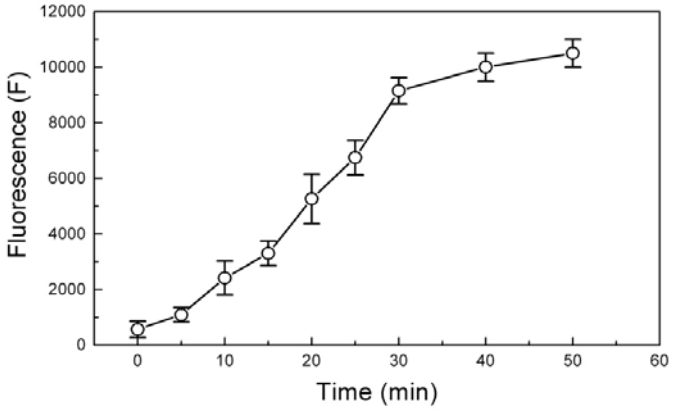

Figure 4-2: Fluorescence intensity of cells expressing chimeric motor proteins, *vs* time of loading with 40 μM Sodium Green in motility buffer. The measurements were made immediately after loading; 30 min was chosen as the optimal loading time. Mean and S.D. of ten cells are shown.

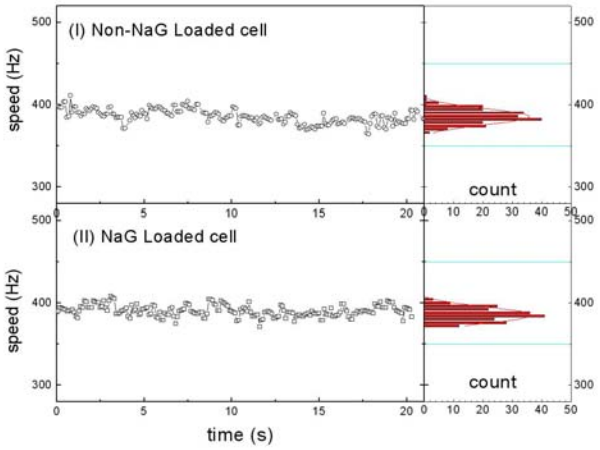

Figure 4-3: Motor speed stability. Speed and stability of chimeric flagellar motors without (upper) and with (lower) optimal Sodium Green loading. Each trace shows 20 second speed measurements of a 0.5 μm bead attached to the flagellum.

4-2-4 Calibration

Intracellular Sodium Concentration:

Average fluorescence intensity (*F*) of individual cells was determined as described (see Chapter 3-1-2). $[Na^+]_{ex}$ was varied by mixing sodium motility buffer with potassium motility buffer (10 mM potassium phosphate, 85 mM KCl, 0.1 mM EDTA, pH 7.0), maintaining a constant ionic strength ($[Na^+] + [K^+] = 85$ mM). After fluorescence measurements, calibration of $[Na^+]_{in}$ for each cell was performed as follows. Fluorescence intensity (*F*) was measured in media of at least three different sodium concentrations containing the ionophores gramicidin (20 μM, Molecular Probes, Inc., Eugene, OR) and carbonyl cyanide 3-chlorophenylhydrazone (CCCP, 5 μM, Sigma, Dorset, UK). Gramicidin forms sodium channels and CCCP collapses the proton-motive force (pmf) preventing the maintenance of a sodium gradient. Thus, after a suitable equilibration period (3 min), $[Na^+]_{in} = [Na^+]_{ex}$. $[Na^+]_{in}$ was calculated, assuming a binding stoichiometry between Na^+ and Sodium Green of 1:1 [Molecular Probes] as

$$[Na^+]_{in} = K_d \frac{F - F_{\min}}{F_{\max} - F}, \qquad (4\text{-}1)$$

where F_{min} is the intensity at $[Na^+]_{in} = [Na^+]_{ex} = 0$, and parameters K_d and F_{max} are obtained by fitting Equation 4-1 to the calibration data.

Photobleaching of Sodium Green:

Several processes could cause the fluorescence intensity of the same cell with the same $[Na^+]_{in}$ to change over time. The Sodium Green dye is converted to its acidic fluorescent form only after entry to the cell, where intracellular esterase activity cleaves off the acetate moieties. The negatively-charged groups of the acidic form greatly reduce the rate of passive leakage from the cell. Continuing activation of dye during observation would lead to increasing fluorescence. Decreasing fluorescence could be caused by leakage of dye out of cells, metabolic or other chemical degradation, or photobleaching. Figure 4-4 (A) shows the fluorescence intensity of a loaded cell in sodium buffer, as a function of time during continuous illumination at an intensity of 9.8 W/cm^2. The curve can be

fitted as an exponential decay with a time constant of 30 ± 0.75 s. The fluorescence intensity decay rate is proportional to illumination intensity (Figure 4-4 (B)) with zero offset, indicating that the main effect in our system is photobleaching. Figure 4-4 (C) shows a combined decay curve for data at different laser powers, illustrating that the effect of photobleaching can be described by $F(x) = F_o \exp(- x/x_o)$, where x is the accumulated laser exposure and $x_o = 310 \pm 20$ $(J/cm^2)^{-1}$. All subsequent measurements of fluorescence intensity used to determine $[Na^+]_{in}$ were corrected for cumulative photobleaching using the formula $F_{corrected} = F_{raw} \exp(x/x_o)$. Photobleaching sets a limit to the number of successive measurements that can be made on a single cell. With a typical illumination intensity of 7.35 W/cm^2 the bleaching time constant is ~50 s. Images with 1 s exposure at this illumination intensity gave fluorescence intensities 5 times greater than noise, which was determined by comparing successive intensities. Thus up to 50 successive measurements can be made before photobleaching causes significant deterioration of the fluorescence signal.

We estimated the signal to noise ratio (s/n) for fluorescence signal F as $(s/n) = \langle F \rangle / \sqrt{\langle F - F_0 \rangle^2}$, where F_0 is the exponential fit to the photobleaching curve (Figure 4-4 (A)). Initial s/n were ~50, and after 50 successive measurements the s/n reduced only by a factor of 2. Here we used a 1 s exposure time throughout, but in practice the time-resolution of our technique is limited only by the frame rate of the camera (up to ~5 kHz for sub-arrays large enough to image a single cell) and the intensity of the illuminating laser, which must be increased to give a large enough photon count within a single frame. Investigations of transient responses should be possible in future, making the trade-off between high time resolution on the one hand and shorter lifetime and/or reduced s/n on the other. Subtle modifications to the technique may allow further optimization. For example in the early stages of bleaching we might use lower exposure times to reach the s/n we need, increasing exposure times in the later stages to maintain the same s/n.

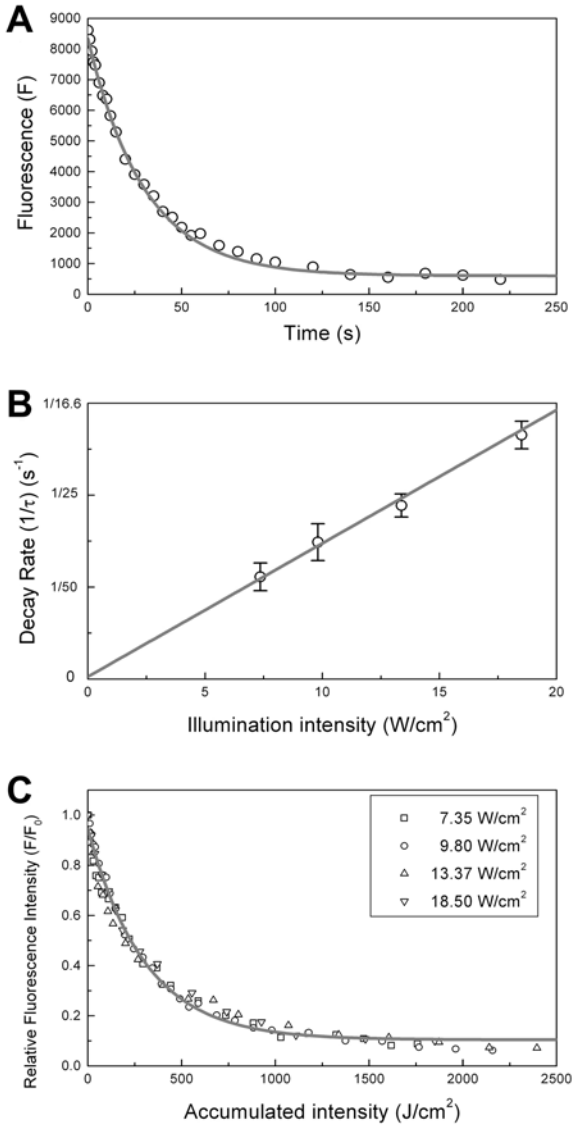

Figure 4-4: Photobleaching of Sodium Green. (A) Fluorescence intensity of a single loaded cell as a function of time during continuous illumination at an intensity of 9.8 W/cm^2, exposure time 1 second. The curve is fitted as exponential decay with a time constant of 30 ± 0.75 s. (B) Photobleaching decay rates as a function of illumination intensity (mean and S.D. of five cells at each intensity). The rates are proportional to intensity as expected for photobleaching (gray line). (C) A combined decay curve for data at different intensities. Photobleaching can be described as $F(x) = F_o \exp(- x/x_o)$, where x is the accumulated laser exposure.

Calibration of Internal Sodium Concentration ($[Na^+]_{in}$):

The Sodium Green fluorescence intensity was calibrated against $[Na^+]_{in}$ for each cell at the end of a series of measurements. The calibration method is illustrated in Figure 4-5. $[Na^+]_{ex}$ was varied in the range 0-85 mM (Figure 4-5 (A)), with gramicidin and CCCP present to collapse the sodium gradient at all times after 2 min. Fluorescence intensity is shown in Figure 4-5 (B). ~3 min was required for equilibration of $[Na^+]_{in}$ following a change in $[Na^+]_{ex}$, after which the fluorescence intensity remained approximately constant. Duplicate measurements at 0 and 85 mM indicate the reproducibility of the fluorescence measurements. The steady-state fluorescence intensity was modeled well by Equation 4-1 (Figure 4-5 (C)). The dissociation constant, K_d, fitted for this cell is 19.0 ± 1.0 mM which compares well to the value of 21 mM quoted by the supplier [Molecular Probes].

Many experimental techniques have been developed to measure intracellular sodium concentrations. However, only fluorescence techniques are currently capable of the sensitivity necessary for accurate measurements at the level of single bacterial cells. There are two methods to determine ion concentrations using fluorescent indicators. Ratiometric methods, in which dual-wavelength measurements detect changes in fluorescence absorption or emission spectra upon ion-binding, are independent of the concentration of the indicator. Monochromatic indicators such as Sodium Green, however, have spectra which change little upon ion-binding and rely instead on differences in fluorescence intensity. This necessitates careful calibration to account for random variation in the concentration of indicator in the sample. Here every cell is calibrated individually following a series of fluorescence measurements, allowing accurate measurement of the response of $[Na^+]_{in}$ in single cells to factors such as $[Na^+]_{ex}$.

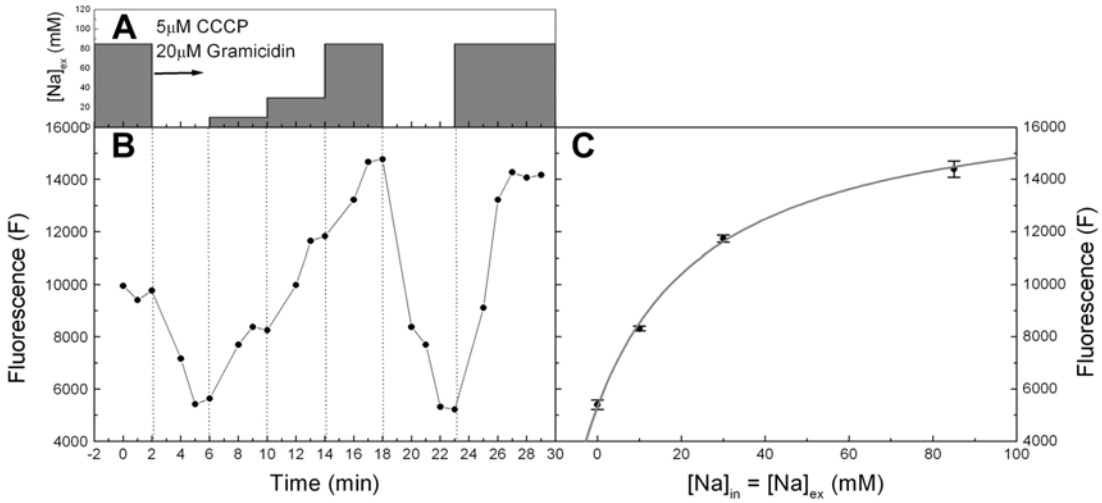

Figure 4-5: Calibration method. (A) $[Na^+]_{ex}$ was varied between 0 and 85mM with gramicidin and CCCP present to equilibrate the sodium concentrations across membrane. (B) Fluorescence intensity in response to changes of $[Na^+]_{ex}$. ~3 min was required for equilibration of $[Na^+]_{in}$. (C) Steady state fluorescence intensity as a function of sodium concentration, with a fit to Equation 4-1. Mean and S.D. of 3 successive measurements of *F* are shown.

4-2-6 Accuracy and Error Estimation

Sources of error in our measurements of $[Na^+]_{in}$ in single cells are as follows.

(1) Random error in measurements of fluorescence intensities *F*. The standard deviation of successive measurements after correction for photobleaching was typically ~5 %, attributable to instrumental noise and bleaching noise. Taking the average of 3 consecutive readings reduces the error to the standard error of the mean, typically ~3 %.

(2) Errors in determining the parameters K_d and F_{max} by fitting calibration data. Variations in these parameters may be due to random errors in the calibration data or to sensitivity of the dye to the intracellular environment in the case of K_d. The standard deviation of fitted K_d was ~9 % (Figure 4-9 (C)). The standard deviations of F_{min} and fitted F_{max} across cells were both ~15 %, however there was considerable co-variance

between fluorescence intensities F from cell to cell due to variable dye loading. The standard deviation of the ratio F_{max}/F_{min}, which determines the contribution to the overall error in $[Na^+]_{in}$ (Equation 4-1), was 9.9 %.

Combining these errors gives error estimates for single-cell measurements of between 22 % and 27 % in the range $[Na^+]_{in}$ = 5-20 mM. The error increases dramatically at high and low values of $[Na^+]_{in}$, reaching 50 % at $[Na^+]_{in}$ = 1 and 50 mM, 100 % at $[Na^+]_{in}$ = 0.4 and 130 mM. Fortunately, the range of sodium concentrations over which Sodium Green is sensitive is similar to that found in *E. coli* cells under our conditions.

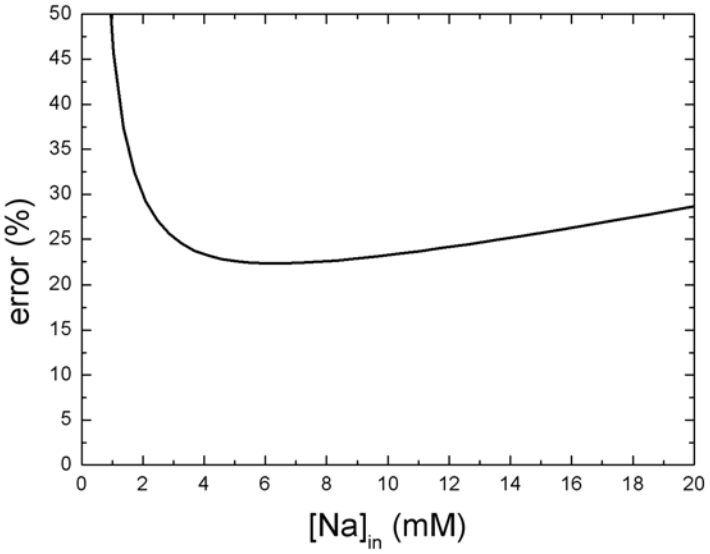

Figure 4-6: Combined error estimation of the Sodium Green measurement. Due to the nature of the calibration equation, this sodium measurement has high error (> 50%) in low concentration ($[Na^+]_{in}$ < 1 mM) and high concentration ($[Na]_{in}$ > 50 mM). In our *E. coli* cell with chimera motor, the intracellular sodium concentration is in the range of 3-20 mM corresponding to the lowest error range.

4-3 Results

4-3-1 $[Na]_{in}$ Response Time

The steady state intracellular sodium concentration is a balance of sodium intake and efflux. The smf contains two parts, membrane potential (V_m) and a contribution from the sodium gradient ($2.3\times kT/e\times\Delta pNa$, where $\Delta pNa = log_{10}\{[Na^+]_{in}/[Na^+]_{ex}\}$, k is Boltzmann's constant, T absolute temperature and e the unit charge), and is maintained by various metabolic processes in *E. coli*. Conventional ion gradient units are in 'P' unit which define that 10-fold concentration difference is 1 (p unit). However, for the conventional comparison to the V_m in terms of its contribution of smf, the corresponding potential in mV, $2.3\times kT/e\times\Delta pNa$ (1 p ~ 59 mV in room temperature) is quoted in parenthesis in the text wherever ΔpNa appears. In the figures, we show ΔpNa in p units on the left scale and the corresponding potential in mV on the right scale.

Single cell measurements of $[Na^+]_{in}$ allow us to determine ΔpNa under a variety of conditions. $[Na^+]_{in}$ reaches a steady state within 2 min after the greatest change of $[Na^+]_{ex}$ in the present study of 1mM-85mM (Figure 4-7 (A)). The gray line in Figure 4-7 (A) is an exponential fit with a time constant t_0 = 29 ± 9 s. Figure 4-7 (B) shows several successive $[Na^+]_{in}$ measurements on a single cell expressing the chimeric flagellar motor, in different $[Na^+]_{ex}$. We changed the external solution every 5 min and measured fluorescence just before each change. $[Na^+]_{in}$ measurements show good reproducibility over the timecourse of nearly one hour during which this cell was observed. Thus, this method is a reliable and reproducible measurement of $[Na^+]_{in}$ in *E. coli*.

Figure 4-8 (A) shows $[Na^+]_{in}$ *vs* $[Na^+]_{ex}$ for one cell with sodium chimeric motors, with the same data plotted as ΔpNa *vs* $[Na^+]_{ex}$ in Figure 4-8 (B). The gray line in Figure 4-8 (A) is the power law fit, $[Na^+]_{in} = A\,([Na^+]_{ex})^{\alpha}$ with concentrations in mM, A = 7.2 ± 0.7 and α = 0.20 ± 0.03.

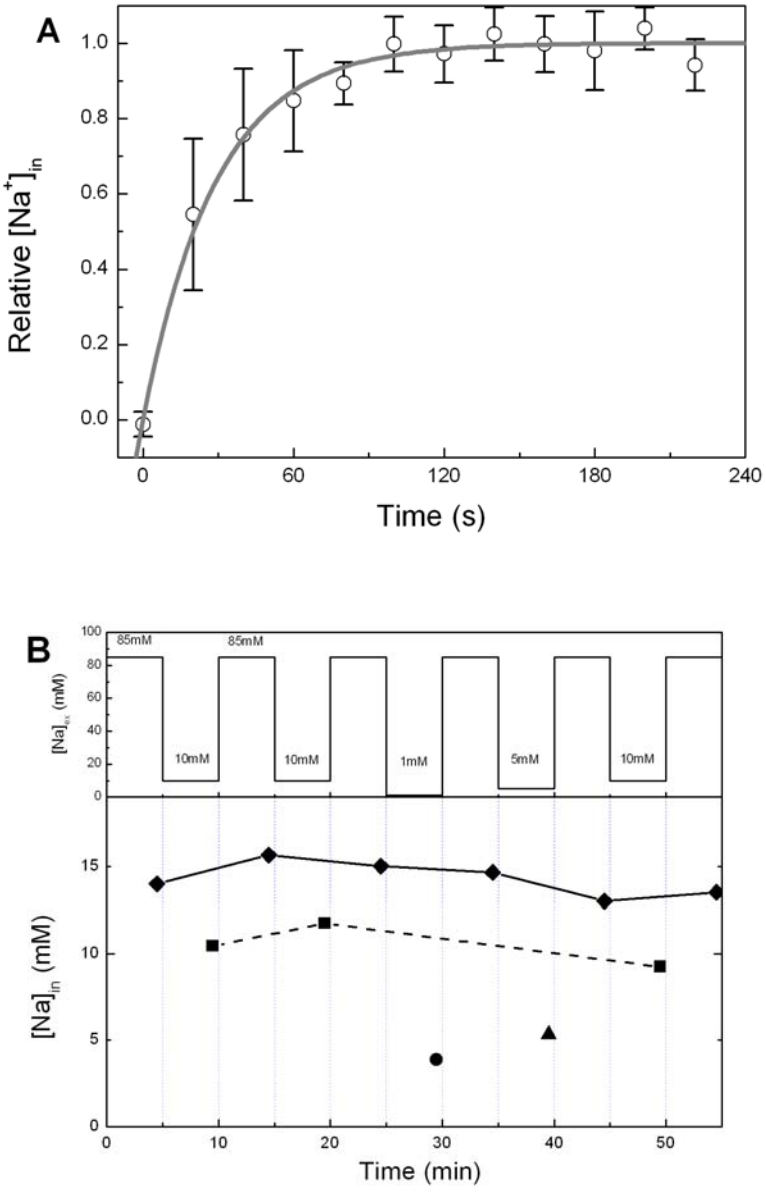

Figure 4-7: In vivo $[Na^+]_{in}$ Measurements. (A) The increase of $[Na^+]_{in}$ in response to a step change of $[Na^+]_{ex}$ from 1 to 85mM. The response for each cell was fitted as $[Na^+]_{in} = A_0 + A_1 (1 - exp\{ -t/t_0\})$ and relative $[Na^+]_{in}$ was defined as $([Na^+]_{in} - A_0) / A_1$. Mean and S.D. of five cells are shown, and an exponential fit with $t_0 = 29 \pm 9$ s. (B) Successive $[Na^+]_{in}$ measurements on a single cell expressing chimeric flagellar motors in different $[Na^+]_{ex}$ as indicated in the upper column (85 mM, diamonds; 10 mM, squares; 5 mM, triangle; 1 mM, circle). Solid and dashed lines connect repeated measurements at the same $[Na^+]_{ex}$, to guide the eye.

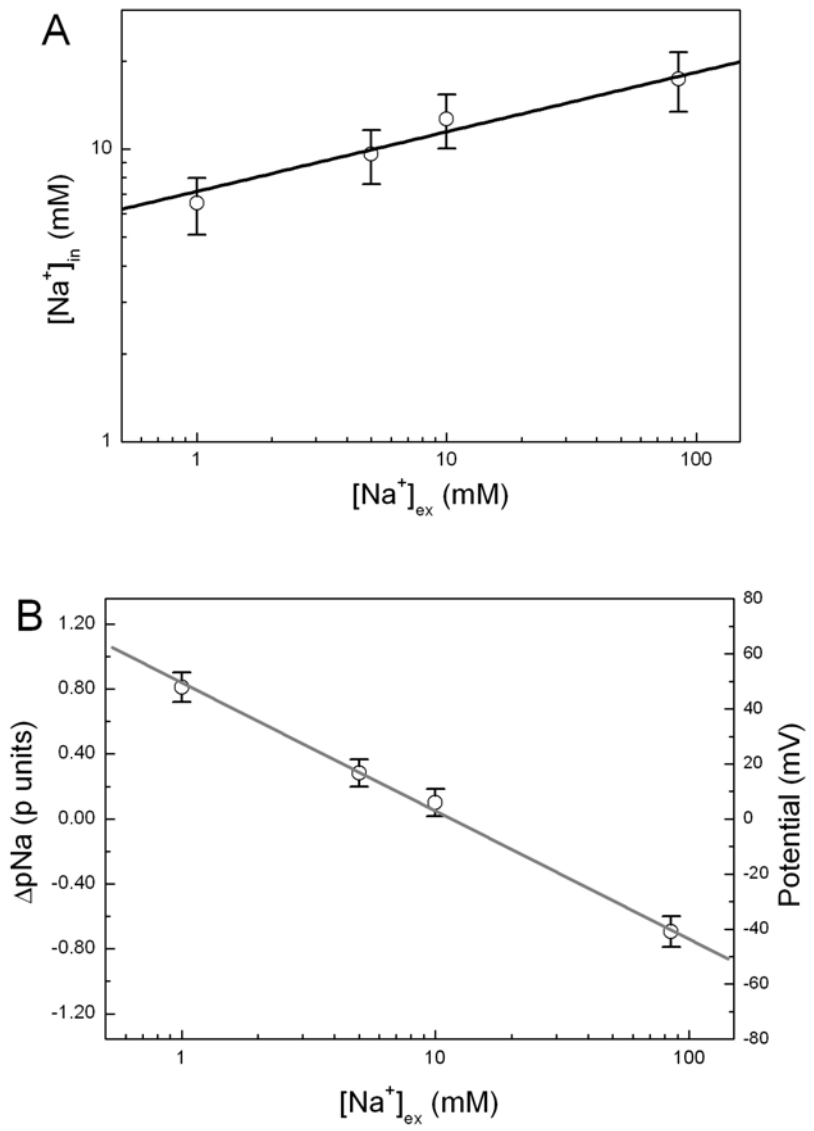

Figure 4-8: Single cell in vivo $[Na^+]_{in}$ measurement. (A) $[Na^+]_{in}$ *vs* $[Na^+]_{ex}$ for one cell with sodium chimeric motors. Each point is an average of three successive measurements, taken at 20 s intervals 5 min after solution exchange at each $[Na^+]_{ex}$. Error bars indicate the combined error, as described in the error estimation. (B) The same data as in (A), plotted as *ΔpNa vs* $[Na^+]_{ex}$. Error bars are converted from (A), assuming no error in $[Na^+]_{ex}$.

4-3-2 $[Na]_{in}$ and ΔpNa vs. $[Na]_{ex}$

Figure 4-9, (A) and (B) show $[Na^+]_{in}$ and ΔpNa respectively as functions of $[Na^+]_{ex}$, measured as in Figure 4-8, (C) and (D) for 8 individual *E. coli* YS34 cells expressing the chimeric flagellar motor. In 85 mM sodium, $[Na^+]_{in}$ was measured in the range 8–19 mM corresponding to a ΔpNa of -0.68 to -1.01 (-40 to -60 mV). The variation of ΔpNa with $[Na^+]_{ex}$ indicates significant but imperfect homeostasis of internal sodium concentration, with $[Na^+]_{in}$ varying only ~ 2.5-fold as $[Na^+]_{ex}$ varies 85-fold in the range 1-85 mM. The sign of ΔpNa reverses at $[Na^+]_{ex}$ between 5 and 20 mM. One interesting feature of the data in Figure 4-9 (A) is the considerable inter-cell variation in the relationship between $[Na^+]_{ex}$ and $[Na^+]_{in}$. For example, values of $[Na^+]_{in}$ measured at $[Na^+]_{ex}$ = 85 mM varied more than 2-fold across our sample of 8 cells (Figure 4-9 (A)), considerably larger than the estimated error of 27 % for each single-cell measurement. Figure 4-9 (C) also shows that there was no strong correlation between $[Na^+]_{in}$ and the fitted calibration parameters, indicating that the variation of $[Na^+]_{in}$ is due to true differences between individual cells rather than an artefact of the measurement procedure.

Effect of Flagellar Motor Proteins on ΔpNa:

The sodium influx through the PomA/PotB stators of the chimeric flagellar motor has not been measured. However, if we assume a similar number of ions pass the motor per revolution as in the proton driven motor [Meister, 1987], then the sodium motor flux could be high compared to other sodium fluxes, for example through a sodium symporter [Hase, 2001]. To investigate this possibility, we compared ΔpNa in *E. coli* strain YS34 expressing chimeric stator proteins, wild-type stator proteins or no stator proteins (Figure 4-10, (A) and (B)). The presence of chimeric stators resulted in an increase in $[Na^+]_{in}$ by a factor of 2-3 across the entire experimental range of $[Na^+]_{ex}$ (1-85 mM), corresponding to an increase of 0.34 (20 mV) in ΔpNa. This suggests that sodium flux through chimeric flagellar motors constitutes a considerable fraction of the total sodium flux in *E. coli*.

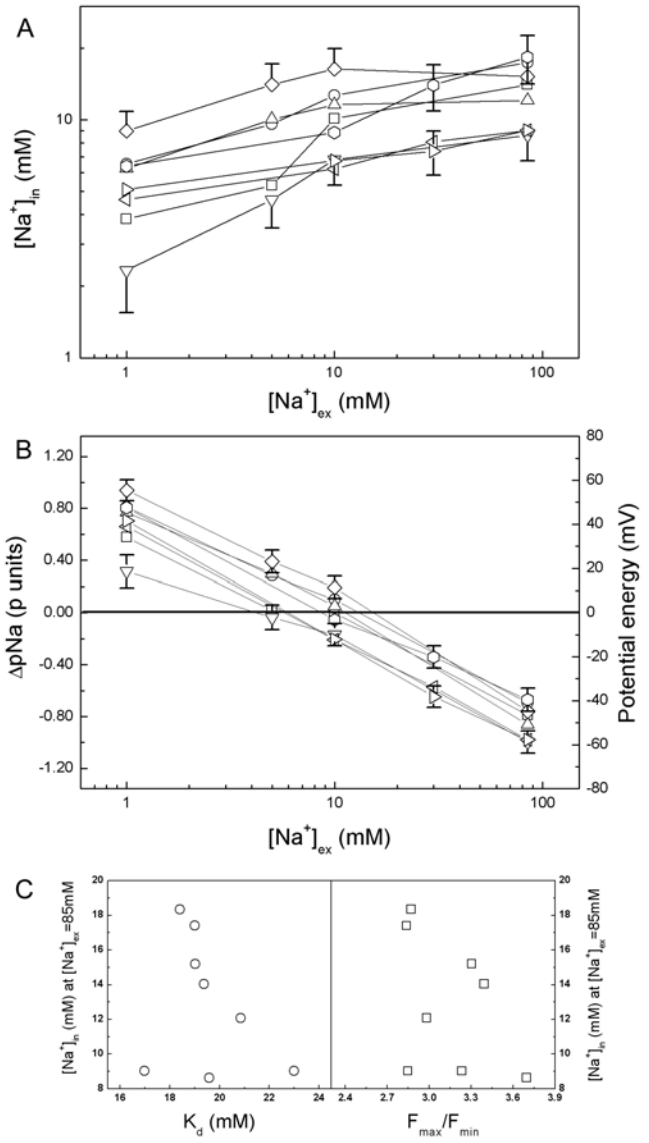

Figure 4-9: $[Na]_{in}$ and *ΔpNa vs.* $[Na]_{ex.}$ (A) $[Na^+]_{in}$ *vs* $[Na^+]_{ex}$ for 8 individual cells expressing the chimeric flagellar motor. (B) The same data as in (A), plotted as *ΔpNa vs* $[Na^+]_{ex}$. (C) Scatter plots of fitted parameters from Equation 4-1, K_d (left) and F_{max}/F_{min} (right), *vs* $[Na^+]_{in}$ at $[Na^+]_{ex} = 85$ mM, for the same 8 cells. There were no strong correlations between calibration parameters and $[Na^+]_{in}$. The standard deviations of K_d, F_{max}/F_{min}, and $[Na^+]_{in}$ were 9.1 %, 9.9 %, and 29.9 % of the mean values respectively. Error bars in (A) and (B) are the same as in Figure 4-8 (A) and (B) respectively.

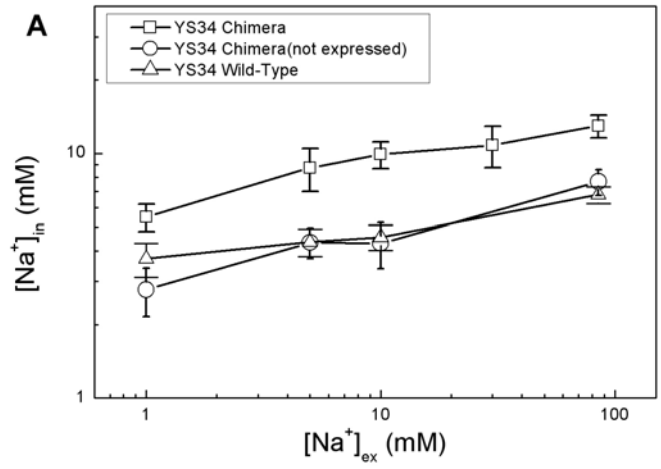

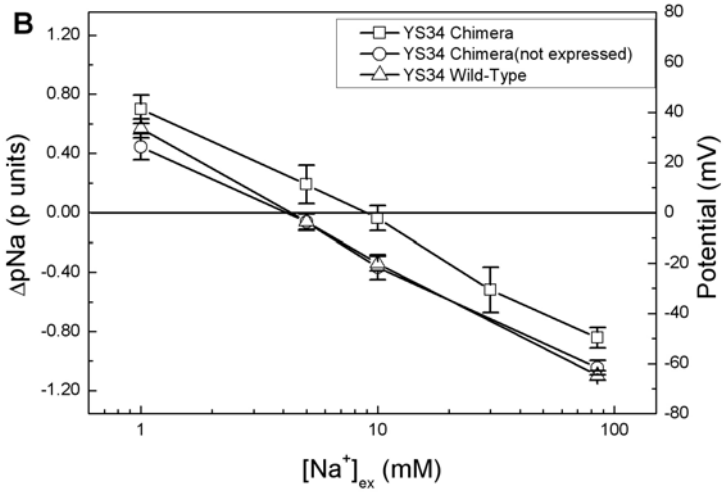

Figure 4-10: Different strain. (A) $[Na^+]_{in}$ *vs* $[Na^+]_{ex}$ in cells expressing chimeric PomA/PotB7 stators (squares, 8 cells), in cells containing the chimeric stator plasmid but grown without induced expression (circles, 5 cells), and in cells expressing wild-type MotA/MotB stators (triangles, 5 cells). (B) The same data as in (A), plotted as *ΔpNa vs* $[Na^+]_{ex}$. Error bars indicate standard errors of the mean for each cell type and $[Na^+]_{ex}$.

4-3-3 $[Na]_{in}$ and ΔpNa vs. pH_{ex} and $[Na]_{ex}$

We extended the $[Na]_{in}$ measurements to different pH_{ex} and $[Na^+]_{ex}$ conditions in which we would like to know ΔpNa. ΔpNa depends weakly upon pH_{ex} (Figure 4-11 (A)) and strongly upon $[Na^+]_{ex}$ (Figure 4-11 (B)). We performed a least-squares global fit of the dependence of ΔpNa upon pH_{ex} and $[Na^+]_{ex}$ to a log-linear model:

$$\Delta pNa = d + e \times pH_{ex} + f \times \log[Na^+]_{ex}, \qquad (4\text{-}2)$$

where d, e, f were fitting parameters and $[Na^+]_{ex}$ is in units of mM. The best fit parameters (expressing ΔpNa in units of mV) were $d = 5 \pm 4$ mV, $e = 5 \pm 1$ mV/(pH unit), and $f = -47 \pm 1$ mV/decade (errors are at 95% confidence limit). The global fits are shown as solid lines in Figure 4-11. Thus to a reasonable approximation ΔpNa depends upon $[Na^+]_{ex}$ but not upon pH_{ex}. This suggests that we have independent control of ΔpNa via $[Na^+]_{ex}$.

4-4 Discussion

Fluorescent Indicator Dye:

We used EDTA to increase the outer (LPS) membrane's permeability to the hydrophobic indicator dye, Sodium Green. Several different protocols for loading dye into cells were tested before our final choice, which was a short incubation with high concentrations of EDTA (10 mM) after cell growth and a subsequent short incubation with Sodium Green at low [EDTA] (0.1 mM). Adding intermediate concentrations of EDTA (0.5 – 5.0 mM) to the growth medium impaired the cell growth rate by a factor of 2. Simultaneous incubation, after growth, with EDTA concentrations (1 – 10 mM) and Sodium Green, increased the proportion of slow spinning flagellar motors, indicating that this approach damages the smf. Using our chosen protocol, we were able to load sufficient dye for accurate fluorescence measurements without any adverse effect on the smf, as assessed by flagellar rotation. Leakage or degradation of dye under these conditions was minimal,

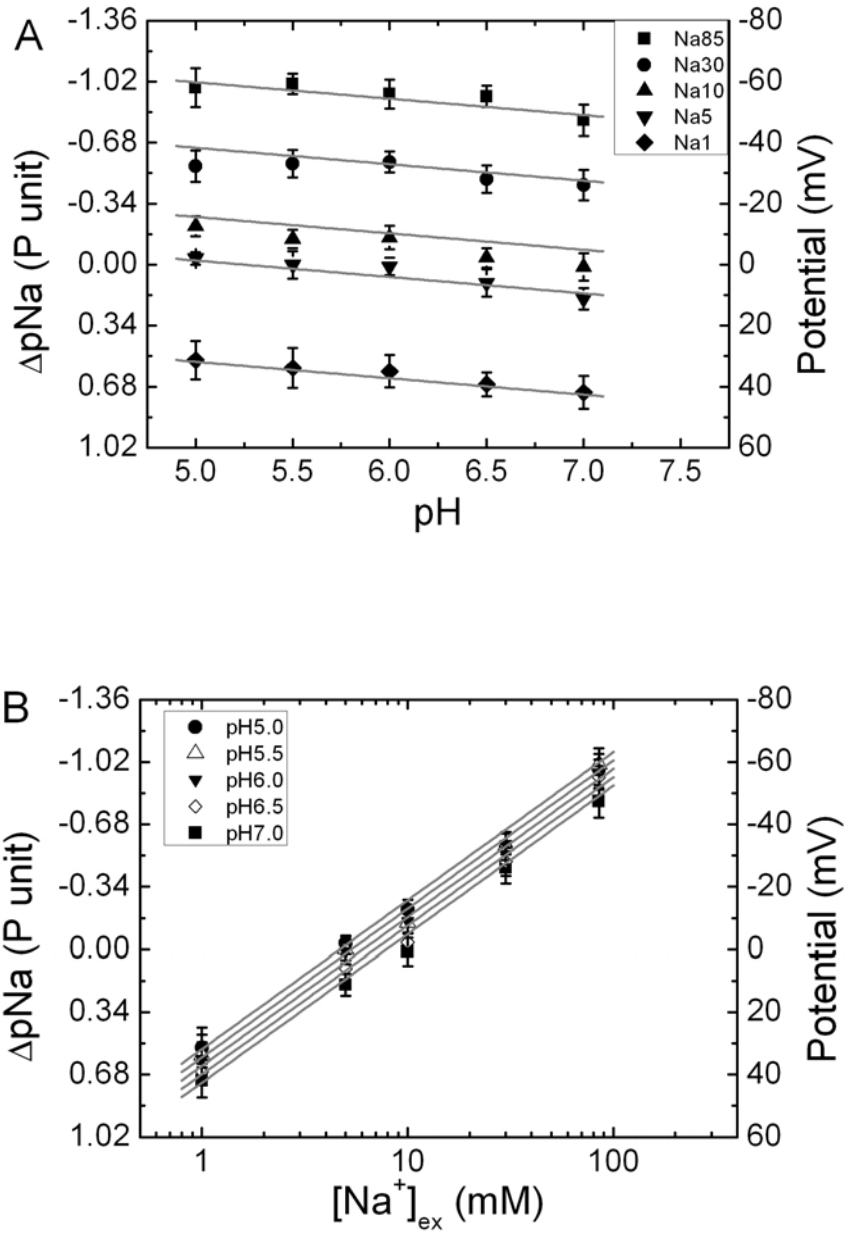

Figure 4-11 *ΔpNa* versus pH_{ex} and $[Na^+]_{ex}$ (A) *ΔpNa* versus pH_{ex} in different $[Na^+]_{ex}$. (B) *ΔpNa* versus $[Na^+]_{ex}$ in different pH_{ex}. Data are from cells expressing chimeric PomA/PotB stators, error bars are standard error of the mean. Lines are global fits of all data to the log-linear model described in the text.

with only a 10 % decrease in fluorescence intensity after 4 hours for cells stored in the dark at room temperature.

Cell-to-cell Variation:

One important advantage of single-cell measurements is that they provide explicit information on variations between individual cells, eliminating this factor as a source of error in multi-cell measurements. We have demonstrated that there is considerable inter-cell variation in the relationship between $[Na^+]_{in}$ and $[Na^+]_{ex}$, which may be due to small number fluctuations in cellular components such as sodium pumps or co-transporters. For example, the number of flagellar motors in one cell is likely to vary in the range 4–8 [Turner, 2000] which may lead to considerable variation of sodium intake.

Comparison to other Measurements of $[Na^+]_{in}$:

The dependence of $[Na^+]_{in}$ on $[Na^+]_{ex}$ has been studied in many bacteria. The relationship can be modeled as $[Na^+]_{in} = A\,([Na^+]_{ex})^{\alpha}$, where $\alpha = 0$ indicates perfect homeostasis of $[Na^+]_{in}$ and $\alpha = 1$ indicates constant ΔpNa. Our present data (for *E. coli* YS34 expressing chimeric flagellar motors at pH_{ex}=7.0, 6.5, 6.0, 5.5, 5.0) are best described by $\alpha = 0.17 \pm 0.02$, implying significant but imperfect homeostasis in the $[Na^+]_{ex}$ range from 1-85 mM. Many previous studies show imperfect homeostasis in *E. coli* [Epstein, 1965], *Alkalophilus Bacillus* [Hirota, 1983], and *Brevibacterium sp.* [Nagata, 1995]. The $[Na^+]_{ex}$ and $[Na^+]_{in}$ ranges for these studies were 50-100 mM and 14-31 mM respectively, similar to our present study. Some reports have suggested that ΔpNa is constant as $[Na^+]_{ex}$ varied in *E. coli* [Reenstra, 1980; Castle, 1986], and in *Vibrio alginolyticus* [Liu, 1990]. In our present experiments the range of ΔpNa is +0.68 to -0.85 (+40 mV to -50 mV) in pH 7.

There are many differences between these experiments: differing strains, growth conditions, measurement sensitivity, additions of various chemicals (for example ^{22}Na, fluorophores or a shift regent in NMR experiments), the timescale of experiments, and whether living cells or lipid vesicles were used. We present here a dynamic, single cell $[Na^+]_{in}$ measurement with fast exchange of the extracellular medium. Previous studies have shown that the flagellar motor speed is proportional to smf [Sowa, 2003] or pmf

[Gabel, 2003]. Motor speed measurements are presented in Chapter 6 combined with measurements of both components of the smf.

Conclusions:

In summary, the monochromatic sodium fluorescence indicator Sodium Green provides a reliable single cell measurement of intracellular sodium concentration. We saw significant inter-cell variation of $[Na^+]_{in}$ at a given $[Na^+]_{ex}$. $[Na^+]_{in}$ was measured in the range 2-20 mM and varied with $[Na^+]_{ex}$ to the power 0.17 ± 0.02. This corresponded to a ΔpNa of +0.68 to -0.85 (+40 mV to -50 mV), varying as the logarithm of $[Na^+]_{ex}$ (~0.85 units [~50mV] per decade) and changing sign at a $[Na^+]_{ex}$ in the range 5-20 mM. Expression of chimeric flagellar motor proteins was associated with a 2- to 3-fold increase in $[Na^+]_{in}$, corresponding to an increase of ~0.34 (~20 mV) in ΔpNa, possibly due to extra sodium influx through the chimeric motors. We found ΔpNa depends strongly upon $[Na^+]_{ex}$ but only weakly upon pH_{ex}. This allows independent control of ΔpNa using $[Na^+]_{ex}$. Future experiments will use this technique to investigate sodium bio-energetics at the single-cell level and the fundamental mechanism of the chimeric flagellar motor.

CHAPTER 5

SINGLE CELL MEMBRANE POTENTIAL MEASUREMENTS

5-1 Introduction

Following the sodium gradient measurement of the previous chapter, we developed a single cell membrane potential (V_m) measurement to obtain smf of chimeric motors in *E. coli*. In this work we studied chimeric sodium-driven flagellar motors in *E. coli*, containing rotors from the proton-driven *E. coli* motor and stators that combine proteins from proton-driven *E. coli* and sodium-driven *V. alginolyticus* motors [Sowa, 2005; Lo, 2006]. *E. coli* cells are too small for direct patch-clamp or micro-pipette V_m measurements. We developed a method to measure V_m in single cells using the Nernstian fluorescent dye, Tetramethyl Rhodamine Methyl Ester (TMRM). We found that V_m in E. coli can be manipulated by external pH (pH_{ex}) and is independent of external sodium concentration ($[Na^+]_{ex}$). Thus we can manipulate V_m by controlling pH_{ex}.

The Nernstian V_m measurement is adapted from a technique for mitochondrial V_m measurement but this is the first time it has been applied to bacterial cells. It could be generally used in many fields as a rapid single cell V_m measurement.

The principle of using a Nernstian V_m dye:

Quantitative measurements of V_m using cationic indicator dyes are based on equilibration of the dye across the membrane according to Boltzmann's law:

$$C_{in}/C_{ex} = exp(-q\ V_m / kT), \qquad (5\text{-}1)$$

where k is Boltzmann's constant, T absolute temperature, q the charge of the dye and C_{in} and C_{ex} are the intracellular and extracellular dye concentration respectively. For a univalent cation, Equation 5-1 can be rearranged to give the Nernst equation:

$$V_m = -2.3\frac{kT}{e}\log\frac{C_{in}}{C_{ex}}. \qquad (5\text{-}2)$$

The dye should have high membrane permeability to ensure rapid equilibration and low toxicity to avoid perturbing the cell. C_{in} and C_{ex} are the concentrations of free dye in aqueous solution, as distinct from any dye molecules that are bound to the cell membrane or otherwise immobilized. Thus minimal binding of the dye to membranes and other intra- or extra-cellular components is desirable, so that the ratio C_{in}/C_{ex} can be determined accurately from fluorescence intensities. A typical bacterial membrane potential is around -150 mV, corresponding to $C_{in}/C_{ex} \approx 350$. This can lead to high concentrations of dye inside the cell, which can in turn lead to aggregation and quenching of fluorescence. Whereas this effect can be used as a qualitative indicator of V_m [Duchen, 1998], quantitative measurements should avoid aggregation by using low concentrations of dye. Thus bright fluorescence, low photobleaching, low aggregation and little self-quenching are further desirable properties of the dye. Many hydrophobic membrane potential dyes have been designed to determine V_m of cells and mitochondria *in vivo* [Ehrenberg, 1988; Loew, 1993; Scaduto, 1999; Fink, 1998]. In particular, the dye TMRM has been shown to be suitable for quantitative measurements of V_m in mitochondria [Loew, 1993].

Because bacteria (and mitochondria) are similar in size to the diffraction limit of a light microscope, the fluorescence intensity of pixels within the image of a single bacterium is not simply proportional to C_{in}, but also includes contributions from adjacent extracellular regions. Typically C_{in} is greater than C_{ex}, thus the brightness of the cell image is reduced compared to a solution of the same concentration and the ratio of internal to external

fluorescence intensities underestimates the ratio C_{in}/C_{ex}. Loew's group has reported the measurement of V_m in individual mitochondria using TMRM fluorescence, correcting for the brightness reduction by measuring the point spread function (psf) of the microscope and modeling the convolution process that reduces the brightness of the cell image [Loew, 1993; Fink, 1998]. In this work we adapted this technique to develop a single-cell fluorescence measurement of V_m in bacteria. We imaged *E. coli* cells immobilized at low density on a microscope coverslip, giving a very well-defined geometry well suited to optical convolution modeling. By using a high quantum-efficiency Electron-Multiplying Charge-Coupled Device (EMCCD) camera, we obtained low-noise images using external TMRM concentrations of 0.1 μM and image exposure times of 10-30 ms. *E. coli* is a gram-negative bacterium with an outer membrane that acts as a barrier to the permeation of hydrophobic molecules such as TMRM. To increase the permeability of the dye with minimal damage to cell function, we pre-treated cells with EDTA as described in section 4-4-2 [Lo, 2006].

5-2 Materials and Methods

5-2-1 Fluorescent Labelling

TMRM:

TMRM is one of the Rhodamine dye family which has been developed for mitochondrial V_m measurement. The chemical structure of TMRM is shown in Figure 5-1. The design of this dye is mainly for the special requirement of Nernstian V_m measurement as discussed in the previous section. The fluorescence of TMRM is weakly pH dependent. However, the pH_{in} of *E. coli* remains at 7.6 as pH_{ex} vary from pH 5 to pH 9 [Slonczewski, 1981]. Therefore, fluorescence from the cell body would not depend on external pH.

Sample Preparation and Dye Loading:

Bacterial cells were prepared as described in section 3-3-2. In order to increase the membrane permeability of TMRM, we used the same protocol as Sodium Green to

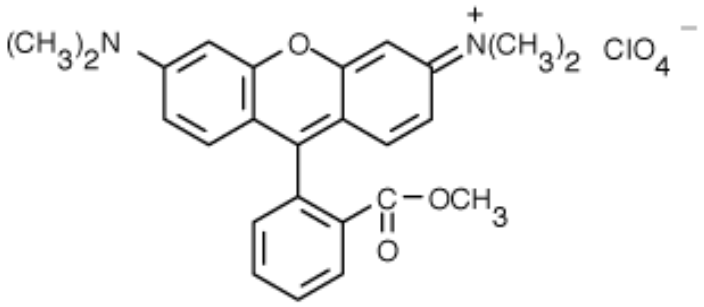

Figure 5-1: TMRM structure.

weaken the outer membrane of *E. coli* by pre-treating with EDTA as described in section 4-2-2. Cells were suspended in sodium motility buffer (10 mM potassium phosphate, 85 mM NaCl, pH 7.0) plus 10 mM EDTA for 10 min to increase permeability to dye, then washed three times in sodium motility buffer. Cells at a density of 10^8 cells/ml were suspended in sodium motility buffer plus 0.1 μM TMRM (MIP, Ann Arbor, MI) and loaded into custom-built flow chambers (volume ~ 5 μl) in which they were immobilized on polylysine-coated coverslips.

5-2-2 Data Acquisition and Processing

Internal Fluorescence Intensity:

Cells were observed in epi-fluorescence using a custom-built microscope as described in section 3-1-1. Images of bacteria with pixel intensities $I(x_i, y_i)$ were obtained with the focal plane passing through the centre of the bacteria and an exposure time of 10-30 ms. The total fluorescence intensity (F_T) of a cell was defined as the average intensity of the central part of the cell, ignoring the marginal area and subtracting the background:

$$F_T = \left\langle I - I_{bg} \right\rangle_{I > I_{cell}} , \tag{5-3}$$

where the background (I_{bg}) and threshold ($\underline{I_{cell}}$) intensities are defined as described Chapter 3-1-2. F_T includes fluorescence due to dye bound to the membrane (F_m) as well

as fluorescence due to free dye (F_{in}). To estimate F_m we treated cells, previously loaded for 30 min with TMRM and $[Na^+]_{ex} = 85$ mM, with 50 μM CCCP for a further 30 minutes (see Figure 5-5). CCCP collapses the membrane potential, under which condition we expect $V_m = 0$ and $C_{in} = C_{ex}$. Any remaining increased fluorescence of the cell compared to the background can be attributed to bound dye. We found that V_m (and therefore also C_{in} and F_m) depended strongly on pH_{ex} but only weakly on $[Na^+]_{ex}$, and we estimated for each value of pH_{ex} studied

$$F_m = \langle F_T \rangle_{cccp}, \tag{5-4}$$

where the average was taken over ~60 cells after loading and CCCP treatment as described above in buffers of the appropriate pH . The internal fluorescence due to free dye was estimated for each single-cell measurement as

$$F_{in} = F_T - F_m. \tag{5-5}$$

External Fluorescence Intensity:

Due to the logarithmic nature of the Nernst equation, C_{in} will be ~350 times greater than C_{ex} when V_m = -150 mV. If the camera exposure time were set to match the pixel intensities within the cell image to the full 14-bit dynamic range of the EMCCD, the external fluorescence intensity (F_{ex}) would be close to the noise level. Therefore we obtained F_{ex} as follows. We filled the flow cell with 0.1 μM TMRM in sodium buffer and imaged empty areas with the focal plane 0.45 μm above the coverslip surface, corresponding to the height of the centre of a cell. (The coverslip surface was easily found by searching for slight scratches.) We defined

$$F_{ex}^* = \langle I \rangle, \tag{5-6}$$

where the average was taken over the entire image. F_{ex}^* was measured at a given illumination laser power with different exposure times in the range 0.1 – 1.0 s (see Figure 5-2), and F_{ex} was defined as the slope of a line fit of F_{ex}^* *vs* exposure time, multiplied by the exposure time for cell images, 10 – 30 ms.

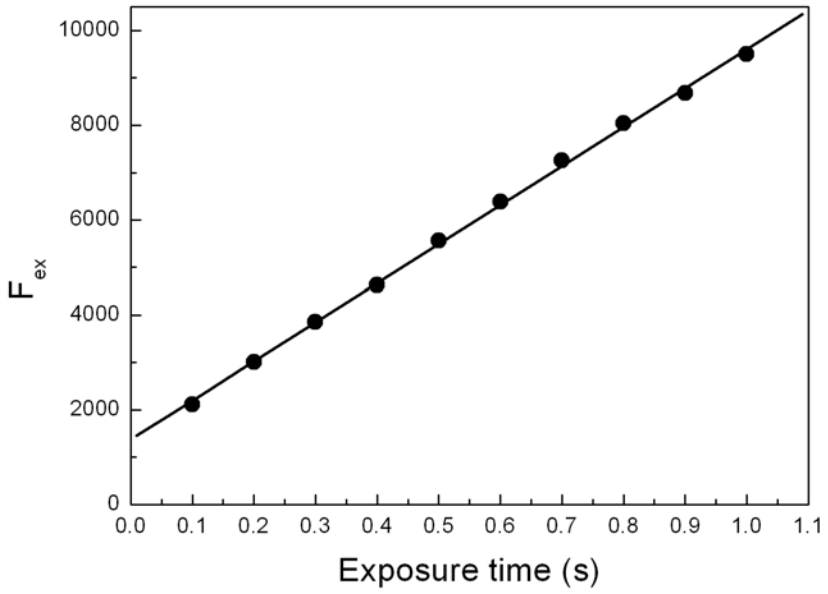

Figure 5-2: External Fluorescence Intensity Measurement. Average fluorescence intensity (F_{ex}*) versus exposure time. The linear fit is F_{ex}*=1381 + 8224×t, where t is the exposure time.

5-2-3 Point-Spread-Function and Calibration

The psf, $P(x_i, y_i, z_i)$, was defined as the pixel intensity $I(x_i, y_i)$ in images of single 20 nm fluorescent beads (Molecular probe, Inc., Eugene, OR) stuck to the coverslip at $x = y = 0$ and at a distance $-z_i$ below the focal plane. The piezo-electric stage was used to scan z_i over the range ± 2.5 μm in 50 nm intervals (the image pixels are 50 nm square, giving a cubic grid). Three images with exposure times of 0.1 s were averaged for each z_i. The psf was normalized after background subtraction and correction for photobleaching (Figure 5-3 (B)).

Optical Convolution Model:

We created a 3D model of a chamber with an *E. coli* cell stuck to the surface, Figure 5-3 (A). The dye concentrations in the model are,

$$C_i(x_i, y_i, z_i) = \begin{cases} 0 : z \le 0, glass \\ C_{ex} : medium \\ C_{in} : cell \end{cases}, \qquad (5\text{-}7)$$

where the subscript *i* indicates $(50\ \text{nm})^3$ voxels filling the model chamber. The cell is a cylinder (2 μm long, 0.9 μm diameter) capped by 2 hemispheres (0.9 μm diameter) and stuck to the surface. The remaining volume of the chamber, which extended for 14 μm, 12 μm, and 3 μm in *x*, *y* and *z*, is filled with medium. The blurred image with the focal plane set at a distance z_0 = 0.45 μm from the coverslip, equivalent to mid-cell height as used for experimental measurements, was calculated as the convolution of the dye distribution and the psf:

$$I_m(x_j, y_j, z_0) = \Sigma_i \left[C_i(x_i, y_i, z_i)\, P(x_j - x_i, y_j - y_i, z_0 - z_i) \right], \qquad (5\text{-}8)$$

where $I_m(x_j, y_j, z_0)$ was the modeled intensity of image pixel *j* (Figure 5-3 (C), lower). The internal fluorescence intensity F_{in} was calculated from the image I_m as described above for experimental data (Equation 5-3 to 5-5), with $F_m = 0$, and the external fluorescence intensity F_{ex} was calculated as the average pixel intensity in a simulated image with $C_{in} = C_{ex} =$ 0.1 μM. Thus, we can simulate the 'blurring' process of the microscope. The relationship of convoluted fluorescence intensity ratio to the dye concentration ratio can be obtained, Figure 5-4. We defined a correction factor $S(F_{in}/F_{ex}) = (C_{in}/C_{ex}) / (F_{in}/F_{ex})$, where C_{in} and C_{ex} are the concentrations input to the model and F_{in} and F_{ex} are the calculated fluorescence intensities, Figure 5-3 (inset).

Calculation of V_m:

We calculated V_m using the Nernst equation (Equation 5-2) and the corrected concentration ratio,

$$C_{in}/C_{ex} = (F_{in}/F_{ex})\, S(F_{in}/F_{ex}), \qquad (5\text{-}9)$$

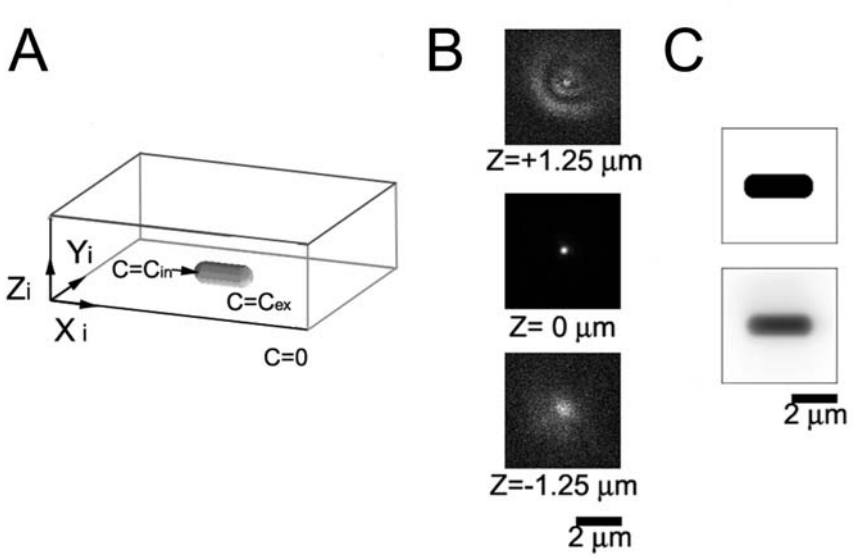

Figure 5-3: Calculation of the correction factor for convolution of the dye distribution with the microscope psf. (A). Model of the dye distribution for a bacterium attached to a glass coverslip. (B). Cross sections of the measured psf at different values of *z*. (C). Dye distribution at mid-cell height (upper) and the corresponding image after convolution (lower).

where F_{in} and F_{ex} were measured experimentally and the correction factor $S(F_{in}/F_{ex})$ was calculated using the optical convolution model.

5-2-4 CCCP Effect and Membrane Binding

Dye Loading and Response Time:

The bacterial outer membrane is a barrier to hydrophobic molecules such as the membrane potential dye TMRM. We increased the membrane permeability by pre-treating cells with EDTA. The external TMRM concentration C_{ex} = 0.1 µM was chosen to balance low membrane binding against sufficient fluorescence. After dye loading, we measured flagellar rotation to confirm that the motor and smf were not affected by the dye. The mean and standard deviation of measured speed of a 1 µm bead attached to the

motor were determined from 26 non-loaded cells and 30 loaded cells in 85 mM Na^+, pH 7. For non-loaded cells the mean speed was 89 ± 6 Hz and the mean value of speed deviation in different cells was 1.8 ± 0.6 Hz; the corresponding values for loaded cells were 88 ± 6 Hz and 1.7 ± 0.8 Hz, indicating no significant effect of dye loading.

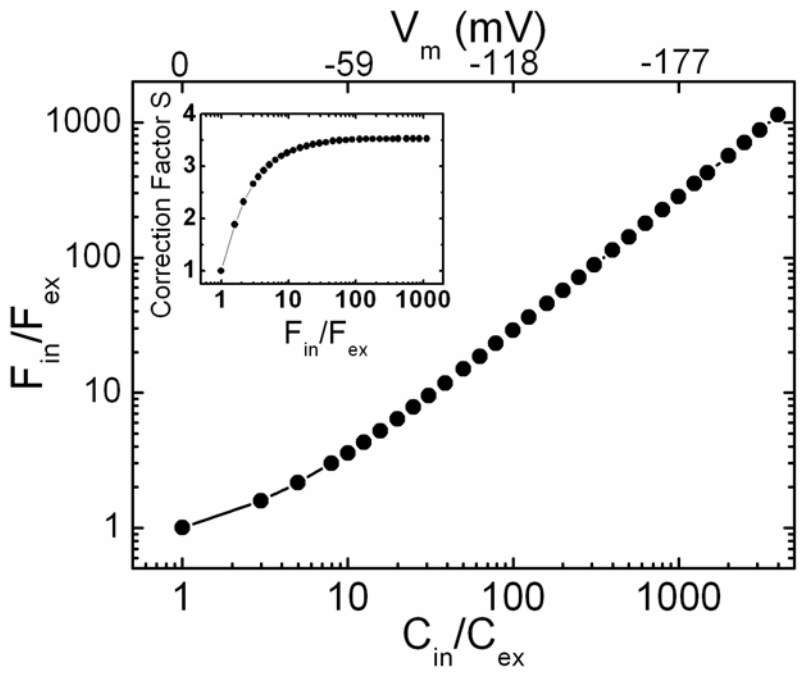

Figure 5-4: Correction Factors. The calculated fluorescence intensity ratio, F_{in}/F_{ex}, versus the concentration ratio, C_{in}/C_{ex}. The correction factor, $S(F_{in}/F_{ex}) = (C_{in}/C_{ex})/(F_{in}/F_{ex})$ is also shown (inset). Fluorescence intensities were calculated from the convoluted image as described in the text.

Figure 5-5 shows the total fluorescence intensity F_T during the loading of dye into live cells in different pH_{ex} (filled symbols). The fluorescence intensities increased exponentially to a steady state within ~30 min, exponential fits gave time constants of 10 ± 0.8 (mean ± SD), 14 ± 2 and 10 ± 2 min for pH 8, pH 7, and pH 6 respectively. The effect of 50 μm CCCP, a proton ionophore which eliminates the membrane potential, is

shown for cells in pH 7 (open circles). F_T decreases exponentially (within ~30 min, fitted time constant 12 ± 3 min) to a stable non-zero value, $F_T = F_M$, indicating membrane binding of the dye (dashed line).

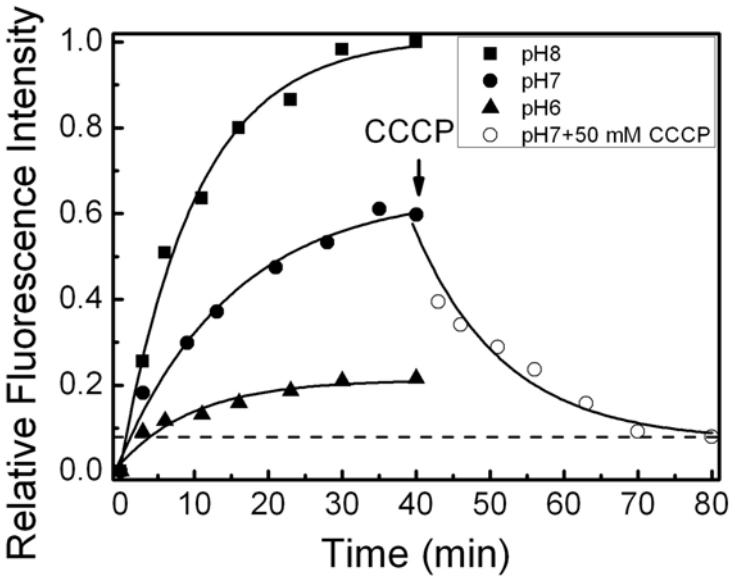

Figure 5-5: Loading and Binding. Total Fluorescence intensity (F_T) of cells versus loading time with 0.1 μM TMRM in sodium motility buffer at different pH_{ex} (filled symbols), and after treatment with 50 μM CCCP at $pH_{ex} = 7$ (open circles). Lines are exponential fits, $F_T = A_0 + A_1 exp\{-t/t_0\}$, time constants t_0 are given in the text. Each point is the mean of measurements of 10 cells.

CCCP effect:

The effect on cell fluorescence of 40 min incubation with a wide range of CCCP concentrations (0.1 - 50.0 μM), at pH 7, is shown in Figure 5-6 (A). As in Figure 5-5, the residual fluorescence intensity at high CCCP concentration is due to membrane binding of the dye. We estimated the fluorescence intensity due to membrane binding, F_m, as the average fluorescence intensity of cells treated with 50 μM CCCP. Figure 5-6 (B) shows the membrane voltage V_m, calculated by Equations 5-2, 5-5, and 5-9, as a function of

CCCP concentration. V_m decreases to zero with increasing [CCCP], indicating that CCCP may be used to achieve low values of V_m in experiments to investigate motor speed or other physiological functions. However, there was considerable intercellular variation in the value of V_m at a given CCCP concentration, as indicated by the large standard deviation (error bars in Figure 5-6 (B). This illustrates the need to measure V_m in each cell if CCCP is to be used to control V_m.

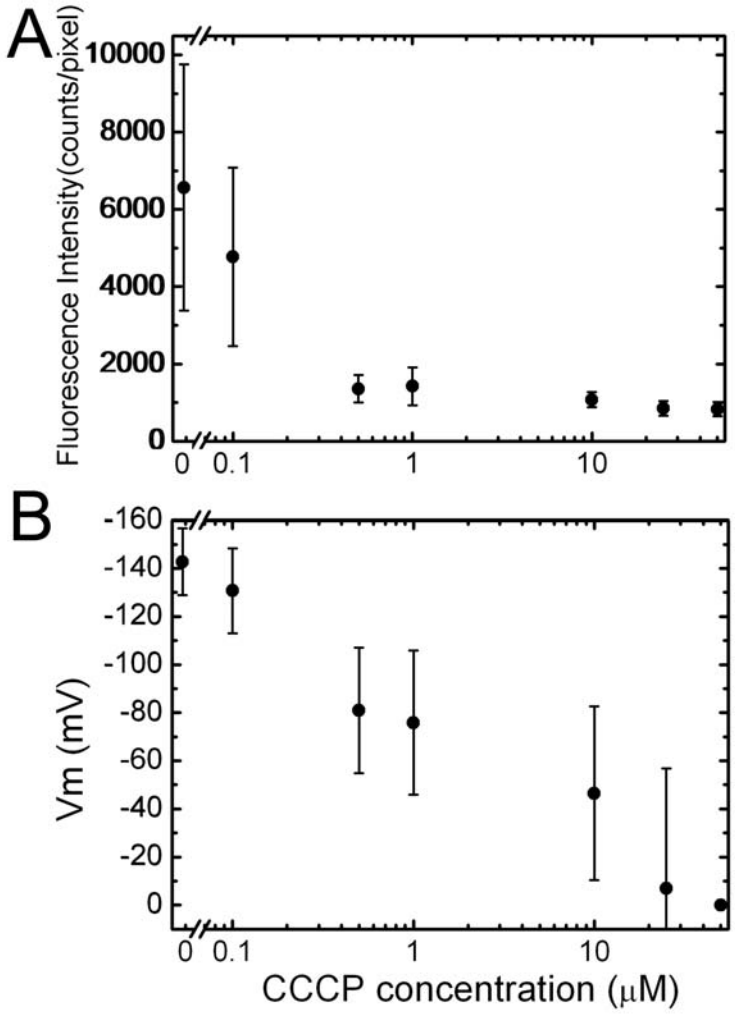

Figure 5-6: CCCP effect. (A) F_T versus CCCP concentration. Cells were loaded with TMRM for 40 min and fluorescence measurements were made 40 min after addition of CCCP. Mean ± SD of 30 cells are shown. (B) V_m calculated from the data in (A) using the method described in the text.

5-2-5 Accuracy and Error Estimation

Accuracy and Error Estimation:

The sources of error in our single-cell fluorescence V_m measurement are as follows.

1. Random error in measurements of fluorescence intensities F_{in}: the standard deviation of successive measurements of the same cell was typically 3 %, attributed to instrumental noise.

2. Focusing error: focusing on the mid-cell plane was judged by the user, introducing a possible source of uncertainty. By repeating the focusing process on the same cell 10 times and reading the z-positions from the piezo-electrical stage driver, we determined a standard deviation of 60 nm in the focusing height. This contributes 2 % uncertainty to fluorescence intensity measurements and a further 2 % to the value of the correction factor $S(F_{in}/F_{ex})$.

3. Cell size effect on the correction factor: the diameter of *E. coli* is about 0.8-1.0 μm and the length is about 3 μm. By varying the dimensions of model cells in the optical convolution calculation, we found that variations of cell length had negligible effect on the correction factor wheras the uncertainty in cell diameter leads to an uncertainty of 11 % in the correction factor.

4. Measurement and fitting error in F_{ex}: the fitting error is typically 1 %.

5. Membrane binding fluorescence intensity F_m: the fluorescence intensity measurements from cells after CCCP treatment showed a standard deviation of 22 %. The relatively high variation may be due to intercellular variation of V_m, the measured standard deviation in V_m of ~15 mV corresponds to a 5-fold variation in dye concentration inside the cell; the higher the dye concentration inside the cell, the higher the expected level of membrane binding.

Combining the contributions of these uncertainties to our estimate of V_m, the uncertainty is less than 3 % at negative values beyond -110 mV, increasing to 5 % at -90 mV, 10 % at -70 mV, 50 % at -40 mV, 100 % at -30 mV, Figure 5-7 (A). Precision at high membrane voltages is helped by the logarithmic nature of the Nernst equation. Under our experimental conditions, V_m in *E. coli* cells had negative values greater than -80 mV and

the uncertainty is below ~6 %. To increase the accuracy of measurements of low values of V_m we can calibrate the membrane binding of each individual cell by applying 50 μM CCCP at the end of an experiment, removing this contribution to the uncertainty. By this method, the estimated uncertainty is less than 5 % at -80 mV, 18 % at -40 mV, 100% at -10 mV, Figure 5-7 (B).

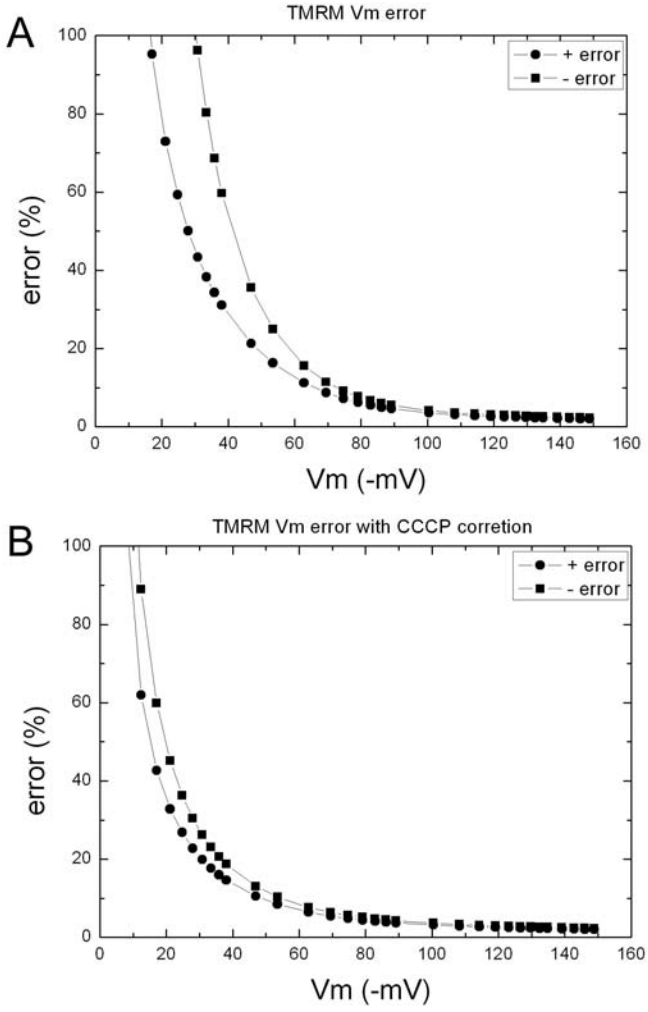

Figure 5-7: Error estimation. (Squire: upper limits; circle: lower limits). (A) Combined error of V_m measurement without individual-cell membrane-binding correction. (B) Combined error of V_m measurement with correction by CCCP treatment of each cell at the end of each experiment. This allows increased precision of measurement in low V_m conditions.

5-3 Results

5-3-1 Dependence of V_m upon pH_{ex}

Figure 5-8 shows the dependence of V_m on pH_{ex} for *E. coli* cells expressing either sodium-driven chimeric or proton-driven wild-type flagellar motors. V_m decreases from -140 ± 14 to -85 ± 10 mV as pH changes from 7 to 5 with chimeric motors, and from -134 ± 17 to -85 ± 13 mV with wild-type motors. We previously showed (Chapter 4) that sodium influx through the chimeric motors is a significant part of the total sodium flux in a cell [Lo, 2006]. The absence of any significant difference in V_m between cells expressing proton- and sodium-driven motors indicates that V_m is not affected by the extra sodium flux though chimeric motors, as expected if V_m is dominated by the proton cycle in *E. coli* and is relatively insensitive to the sodium cycle.

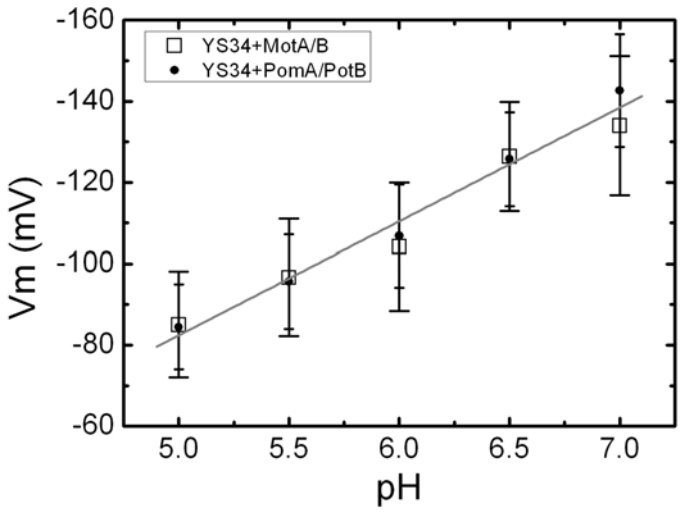

Figure 5-8: V_m versus pH_{ex} at $[Na^+]_{ex}$=85mM in cells expressing chimeric PomA/PotB7 stators (solid dots) and in cells expressing wild-type MotA/MotB stators (open squares). For Each point, Mean ± SD of measurements from 50 cells are shown.

5-3-2 Dependence of V_m upon $[Na^+]_{ex}$

We extended V_m measurement to different $[Na^+]_{ex}$ and pH_{ex} where we are interested to do BFM speed measurements. This indicates that V_m depends on pH_{ex} but not upon $[Na^+]_{ex}$, Figure 5-9. The wide-cap error bars in Figure 5-9 for pH 7 (squares) are standard deviations of measurements of 50 cells and are considerably larger than the estimated single-cell uncertainty in each measurement of V_m (~3 mV, see section 5-2-5). Narrow error bars in Figure 5-9 are the standard error of the mean of measurements of 50 cells. Thus the standard deviation reflects intercellular variation in the value of V_m at a given pH_{ex} and $[Na^+]_{ex}$.

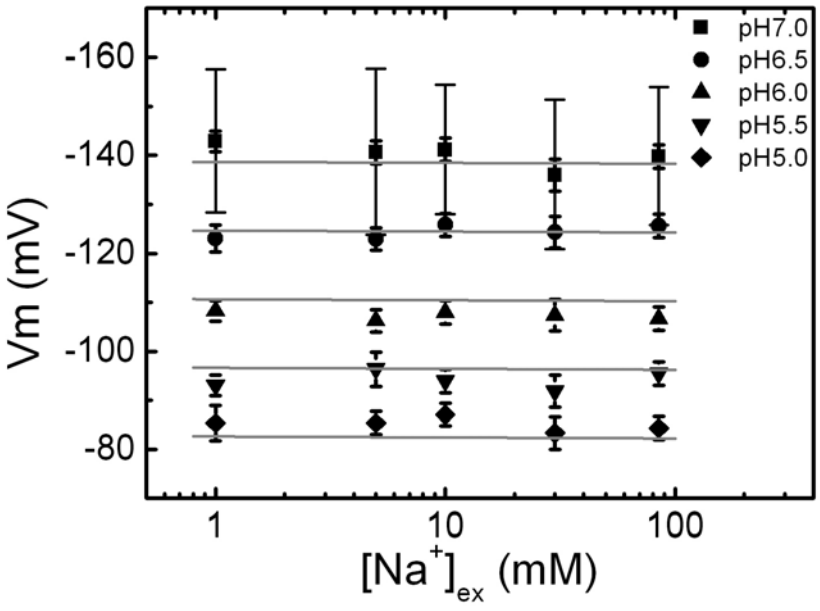

Figure 5-9: V_m versus $[Na^+]_{ex}$ in different pH_{ex}. Wide-cap error bars indicate standard deviations of measurements of 50 cells, narrow-cap error bars show the standard error of the mean.

5-3-3 Smf vs pH_{ex} and $[Na]_{ex}$

We previously reported the dependence of the internal sodium concentration $[Na^+]_{in}$ and the sodium concentration gradient ΔpNa upon $[Na^+]_{ex}$ and pH_{ex} in *E. coli*, Chapter 4. Here, we show the V_m dependency on these two external control parameters, $[Na^+]_{ex}$ and pH_{ex}. We performed a least-squares global fit of the dependence of V_m upon pH_{ex} and $[Na^+]_{ex}$ to a log-linear model

$$V_m = a + b \times pH_{ex} + c \times \log[Na^+]_{ex}, \tag{5-10}$$

where *a, b, c* were fitting parameters and $[Na^+]_{ex}$ is in units of mM. The best fit parameters for V_m (Figure 5-8, 5-9) were $a = 57 \pm 4$ mV, $b = -28 \pm 1$ mV/(pH unit) and $c = 0 \pm 1$ mV/decade. Thus to a reasonable approximation, V_m depends upon pH_{ex} but not upon $[Na^+]_{ex}$, and ΔpNa depends upon $[Na^+]_{ex}$ but not upon pH_{ex}.

Combining the global fitting equation of ΔpNa in Chapter 4,

$$\Delta pNa = d + e \times pH_{ex} + f \times \log[Na^+]_{ex}, \tag{4-2}$$

where $d = 5 \pm 4$ mV, $e = 5 \pm 1$ mV/(pH unit), and $f = -47 \pm 1$ mV/decade, allows independent control of the two components of the smf using pH and sodium concentration as the control parameters. Figure 5-10 shows smf in different $[Na^+]_{ex}$ as a function of pH_{ex}.

5-4 Discussions

Comparison to other V_m measurements:

Our measurements of V_m in single *E. coli* cells are consistent with previous results. Felle et al. measured V_m in *E. coli* using the distribution of radio-labelled permeant cations TPP^+ and $TPMP^+$ [Felle, 1980]. The distribution of these ions follows the Nernst equation and their uptake can be determined by dialysis or filtration. They found that V_m increased linearly from -80 mV at pH 5 to -130 mV at pH 7, a slope of -25 mV/pH unit (compared

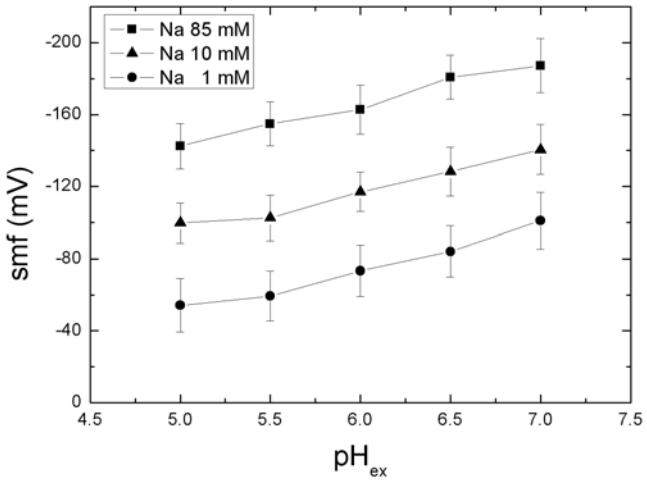

Figure 5-10: smf vs pH_{ex} and $[Na]_{ex}$. smf can be varied from -187 mV to -54 mV by changing pH_{ex} and $[Na]_{ex}$.

to our measured value of -28 mV/pH unit). Also using *E. coli* and the same experimental method, Castle et al. measured V_m = -176 mV at pH 8.5 and -130 mV at pH 6.5 (-23 mV/pH unit) [Castle, 1986] and Minamino et al. measured V_m = -130 mV at pH 8.0 and -54 mV at pH=5.0 (-24 mV/pH) [Minamino, 2003]. Novo et al. measured V_m = -120 mV in *Staphylococcus aureus* and *Micrococcus luteus* using the aggregation and redshift of cyanine dye [Novo, 1999]. Suzuki et al. measured V_m changes induced by a K^+ diffusion potential in *E. coli* and *Rhodospirillum rubrum* using the aggregation and quenching of carbocyanine dye [Suzuki, 2003]. This cationic dye can permeate the membrane freely and redistributes according to the Nernst equation. The high concentration of dye inside the cell at high V_m causes aggregation and thus quenches the fluorescence of the whole sample. However, the authors did not report measurement of the natural V_m in either species.

Unlike our method, all of the above measurements represent ensemble averages of a large number of cells. Felle et al. measured V_m = -135 mV at pH 7 in giant *E. coli* spheroplasts using a patch-clamp micropipette. Although this is a single-cell method, the production of

giant spheroplasts is more disruptive than our method and in particular requires disruption of the cell wall which makes simultaneous measurements of the flagellar motor impossible. Lowe et al. measured $V_m \approx$ -150 mV in individual mitochondria in neuroblastoma cells using a method very similar to ours [Loew, 1993]. Our data show large intercellular variation, ~15 %, in the measured values of V_m at a given pH. We measured similar cell-to-cell variation in ΔpNa at a given $[Na^+]_{ex}$ [Chapter 4; Lo, 2006], indicating that individual variation between genetically identical cells extends to both components of the smf. Based on extrapolation of the linear relationship between motor speed and ΔpNa, we previously predicted that V_m would be -137 mV at pH 7, in close agreement with our measured value of -140 ± 2 mV (mean ± SEM) in this work. We found that ~30 min was required for equilibration of dye concentrations in our experiments, presumably due to relatively low permeability of the outer membrane to dye, after our treatment with EDTA. This limits the time resolution of our technique. Faster response times may be possible by altering our method of permeabilizing the outer membrane, but care would be needed to quantify damage to cells that may be caused by such treatments.

Sodium Energetics in *E. coli*:

We have shown that V_m in *E. coli* varies linearly with pH_{ex}, and is independent of $[Na^+]_{ex}$ and of the sodium flux through chimeric flagellar motors. This indicates that the membrane voltage is dominated by the balance of proton fluxes and varies in such a way as to stabilize the pmf and internal pH as pH_{ex} changes [Minamino, 2003; Castle, 1986]. ΔpNa on the other hand depends strongly on $[Na^+]_{ex}$ and only weakly on pH_{ex}, allowing independent control of the two components of the smf over the ranges -85 to -140 mV in V_m and -60 to +40 mV in ΔpNa. Larger values of V_m are possible using alkaline pH, up to a maximum observed in this work of V_m = -165 mV and smf = -210 mV, but the smf is not stable under these extreme conditions in cells expressing sodium-driven chimeric flagellar motors. There is no strong evidence for the existence of a primary sodium pump in *E. coli*, and the best candidate for maintaining the smf is the sodium/proton antiporter [Padan, 2001]. This is consistent with the weak linkage we observed between the smf

and proton energetics, especially if both components of the pmf are equally effective in maintaining the smf.

Conclusion:

In this Chapter, we have presented single bacterial cell V_m measurements using a Nernst potential dye TMRM. V_m in *E. coli* depends strongly on pH_{ex} but weakly on $[Na^+]_{ex}$. Combining single cell V_m and intracellular sodium measurements, the smf of cells can be determined. In the pH range 5.0-7.0 and external sodium concentration 1-85 mM, the smf varies from -53 to -187 mV. Thus, we can vary each component of smf by controlling external pH_{ex} or $[Na^+]_{ex}$. In the next chapter, we will use this knowledge to study chimeric motor rotation regarding the energetics of the motor.

CHAPTER 6

SPEED, TORQUE, and SMF

6-1 Introduction

The rotational properties of the chimeric motor are an interesting topic because the torque is generated by the interaction between proteins from different species: a rotor from the proton-motor and a stator from the sodium-motor. The rotation speed in the chimeric sodium-driven-motor is even faster than in the wild-type proton-driven motor of *E. coli*. The torque-speed relationship of the chimeric motor should provide valuable information about how these proteins interact. Using the smf control developed in the previous two chapters, here we study the effect of smf on motor rotation.

The knowledge of the physical and mechanical properties of the YS34 chimera strain is also fundamental for the use of the motor for further experiments. For example, the detailed structure of the slow rotation which leads to the discrete stepwise motion in rotation. The direct observation of steps in the rotation of the chimeric motor is an exciting milestone [Sowa, 2005]. However, control of the conditions of the step observations was limited by the knowledge of motor properties at that time: the motors were working in slow but unstable conditions where the energy condition of the motor was not known. The ultimate goal of step observation is statistical results related to the

energy and function of the motor. At the end of this chapter, direct observation of steps in stable rotation and statistical results are presented.

6-2 Steady-State Induction

Aims:

The aim of the experiments in this chapter is to know the rotation speed in different conditions: speed as a function of stator number, load (different bead sizes), pH_{ex} and $[Na^+]_{ex}$. Several conditions must be carefully controlled such as growth conditions, stator-protein plasmid inducer, and filament shearing. Thus, the motor speed can be measured and the torque generated by the motor can be estimated precisely.

Steady State Induction and Speed Calculation:

In *E. coli* YS34 strain with an inducible stator plasmid, we can control the induction level of the stator protein PomA/PotB by adding different concentrations of inducer. Standard bead assay and BFP rotation measurement are applied in this section. For larger beads (1 μm, and 0.75 μm, 0.5 μm beads) and small beads (0.35 μm and 0.2 μm), we used 1064 nm and 632 nm wavelength lasers respectively for the measurements. Each cell was observed for 10 s and the speed was calculated 180 times during this interval.

Different Loads:

When the BFM works in different load, it operates in different mechanical conditions. Figure 6-1 shows the steady state speed histogram of ~ 30 cells with 1 μm beads (high load) at different levels of induction (85 mM $[Na^+]_{ex}$ and pH 7). At medium and low induction (Figure 6-1 (A, B)), the speed histogram shows discrete peaks with roughly equal intervals, corresponding to different numbers of torque generating units in the motor. At high induction (Figure 6-1 (C)), the motor speed saturated at an average ~ 93 Hz. At medium and low induction, the speed histogram can be fitted with a multi-Gaussian function and the intervals are ~ 8.6 Hz, Table 6-1. The saturated speed divided by this interval corresponds to about 11 levels, consistent with a recent report of 11 torque generating units observed in wild-type *E. coli* [Reid, 2006]. However, unlike

wild-type *E. coli*, the chimeric motor shows no reduction in the size of the last few intervals.

In the medium load regime (0.75 μm and 0.5 μm beads), the steady-state speed histograms show similar results. In low induction conditions, larger intervals of 17 Hz and 40 Hz for 0.75 μm and 0.5 μm beads respectively can be observed, Figure 6-2 (A, C). In high induction, the motor speed saturated at 174 Hz and 402 Hz respectively, Figure 6-2 (B, D).

In low load conditions (0.35 μm and 0.2 μm beads) and low induction, multi-peak speed histograms can also be observed with larger intervals, 73 Hz and 111 Hz respectively, Figure 6-2 (E, G). In high induction, the motor speed saturated at 601 Hz and 678 Hz but the relative standard deviations are slightly higher than in high load, Figure 6-2 (F, H).

Multiple Gaussian fitting was applied to these steady-state speed-histograms to obtain the motor speeds with different stator numbers in different load, see Table 6-1. Full induction saturated speed can be measured in high induction samples, listed in Table 6-1. This demonstrates that the steady-state speed measurement is a simple method to assess low stator numbers.

In the 1 μm high load condition, the full induction saturated speed divided by the average interval is about 11 which indicates at least 11 torque generating units in a fully-induced motor. However, in medium and low load conditions, this ratio decreases from 10 to 6 for 0.5 μm and 0.2 μm beads respectively, Table 6-2. Assuming that in full induction conditions all motors have the maximum number of stators, this indicates that the motor speed increases linearly with the torque-generating unit number in high load conditions but saturates with torque-generating unit number in low load conditions. This is consistent with the similar observation of the wild-type proton-driven BFM in *E. coli* which can be explained by high duty ratio [Ryu, 2000].

Table 6-1

Steady-state low and full induction speeds using Gaussian fit to the histogram peaks

Speed (Hz)	1st Level	2nd Level	3rd Level	4th Level	5th Level	Saturated Speed
1 μm Bead	8.8±1.1	16.2±1.7	23.3±2.8	34.2±1.4	41.4±1.6	92.5 ± 3.7
0.75 μm Bead	15.8 ± 2.8	35.8 ± 2.7	52.5 ± 5.5			174 ± 7
0.5 μm Bead	41 ± 7	76 ± 7	122 ± 10			402 ± 21
0.35 μm Bead	73 ± 10	153 ± 21	233 ± 11			601 ± 30
0.2 μm Bead	111 ± 16	213 ± 21				678 ± 41

Table 6-2

Steady-state low and full induction speeds using Gaussian fit to the histogram peaks

Speed (Hz)	Average Interval	Saturated Speed	ratio
1 μm Bead	8.3	92.5 ± 3.7	11.14
0.75 μm Bead	17	174 ± 7	10.23
0.5 μm Bead	40	402 ± 21	10.05
0.35 μm Bead	75	601 ± 30	8.01
0.2 μm Bead	109	678 ± 41	6.22

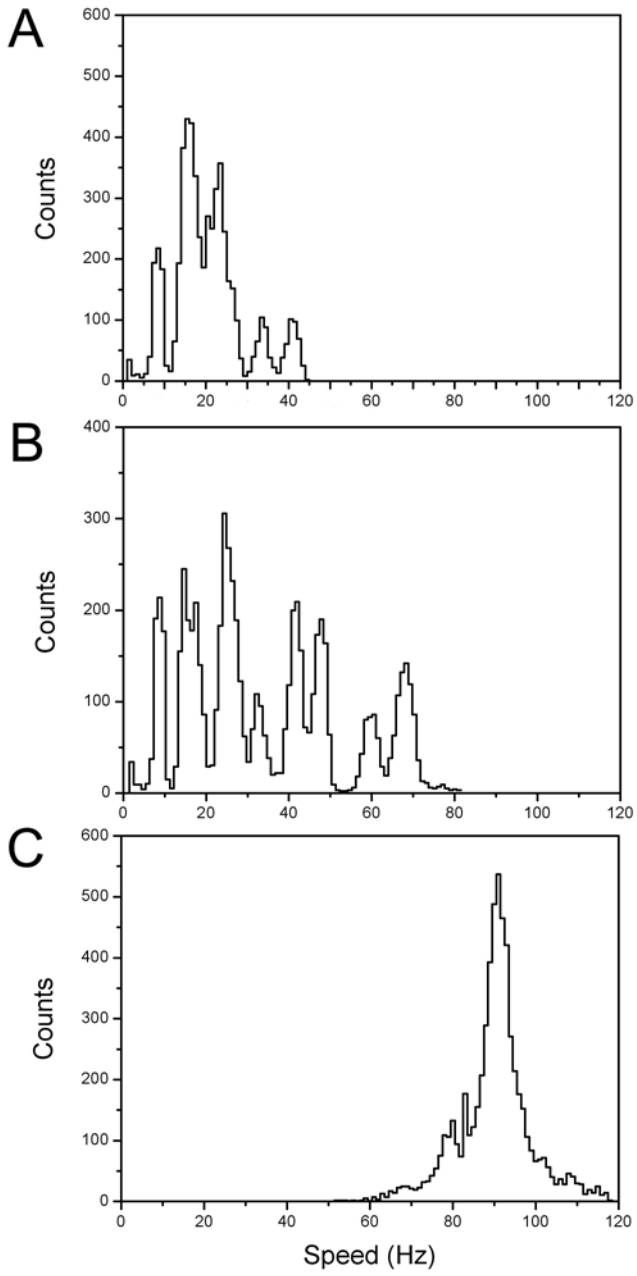

Figure 6-1: Steady-state induction of chimeric stator proteins. The motor speeds were monitored by 1 μm beads attached to the filament stubs in motility buffer with 85 mM $[Na^+]_{ex}$ and pH 7. (A) Speed histogram at low induction (6 μm IPTG, 30 cells). (B) Medium induction (8 μm IPTG, 35 cells). (C) High induction (25 μm IPTG, 30 cells). Each cell was measured 10 s, calculating into 180 speed values with 0.05 s intervals. Speed histograms bin size was 1 Hz corresponding to the power spectrum resolution. At low induction, peaks correspond to discrete numbers of torque-generating units.

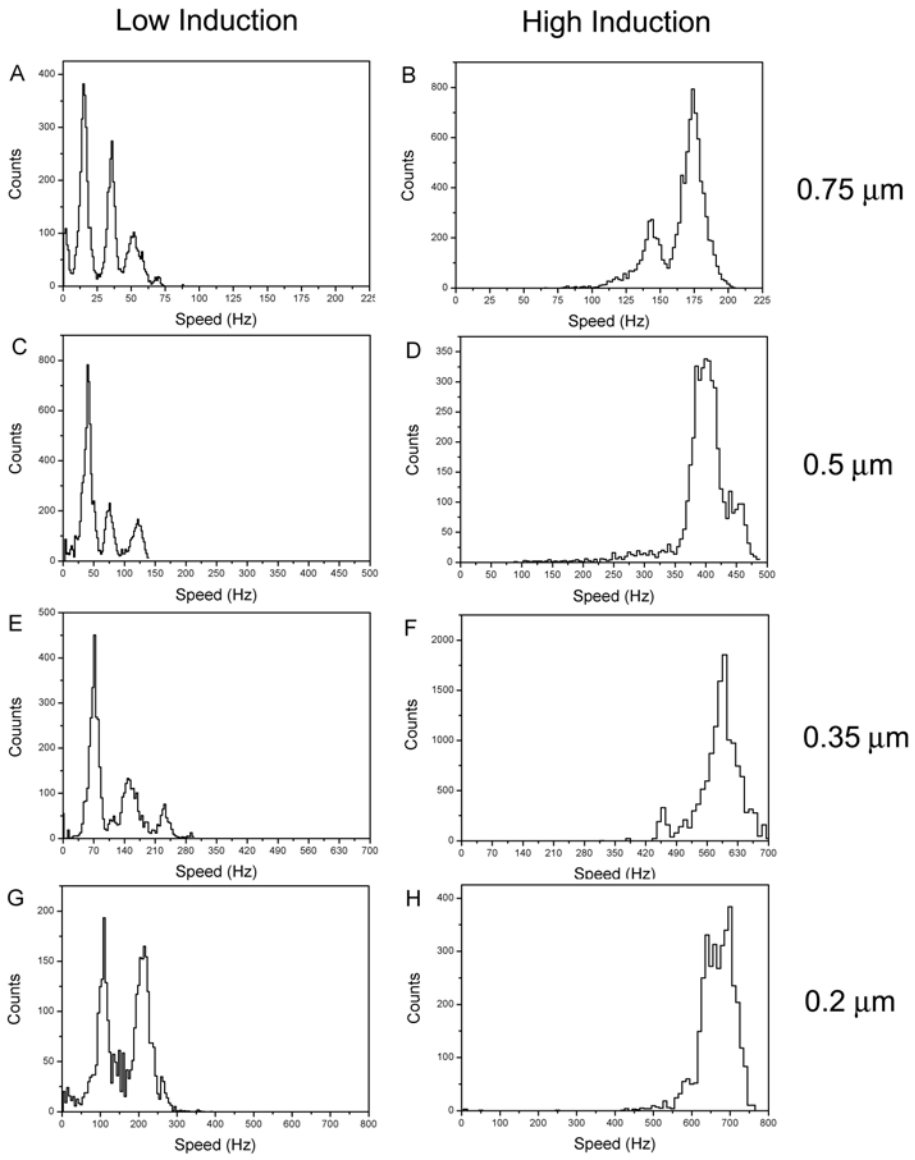

Figure 6-2: Steady-state low induction (6 µM IPTG) and high induction (25 µM IPTG) speed histograms of cells expressing chimeric stator proteins in different load. (A) 0.75 µm beads, low induction, 33 cells and (B) high induction, 50 cells. (C) 0.5 µm beads, low induction, 59 cells and (D) high induction, 26 cells. (E) 0.35 µm beads, low induction, 25 cells and (F) high induction, 70 cells. (G) 0.2 µm beads, low induction, 17 cells and (H) high induction, 21 cells.

6-3 Resurrection

Aim:

In the stator protein deleted strain, we can restore motility by adding an inducer of the stator plasmid, a process known as resurrection. Successive increases of motor speed with discrete speed intervals indicate individual torque-generating unit incorporation in to the motor. Here, we present resurrection experiment results to confirm that the discrete motor speed levels obtained from steady-state measurements indicate different numbers of torque-generating units.

Cell Growth and Sample Preparation:

The cells were grown with a low concentration of inducer (4 μM), resulting in a small number of motors rotating with only one stator. The cells and beads were then loaded into a flow-cell sequentially. After adding a high concentration of inducer (100 μM IPTG) with 10 % TB to the flow-cell, observations of motor rotation were made. In general, the motor shows initial speed increase after ~ 15 min, the time required for the cells to produce stator proteins.

Resurrection:

Figure 6-3 (A) shows a motor resurrection speed trace with a 1 μm bead in 85 mM $[Na^+]_{ex}$ and pH 7. The histogram of the speed shows multiple peaks with roughly equal intervals. Similar to steady state induction experiments, the speed histogram can be fitted with multiple Gaussian functions to obtain the speed of each level. The intervals are slightly smaller than steady state induction speeds. This may be due to the high energy consumption during protein production (as a result the cells may have lower smf).

Motor resurrection with lower viscous load also shows stepwise speed increments, Figure 6-3 (B, C). The speed histogram shows multiple peaks with larger intervals. Resurrection speed levels are very similar to steady-state speeds, listed in Table 6-3. Thus, we can conclude that the speed levels obtained from steady-state speed histograms correspond to different numbers of torque-generating units. Resurrection is another method to assess low stator number speed in different conditions.

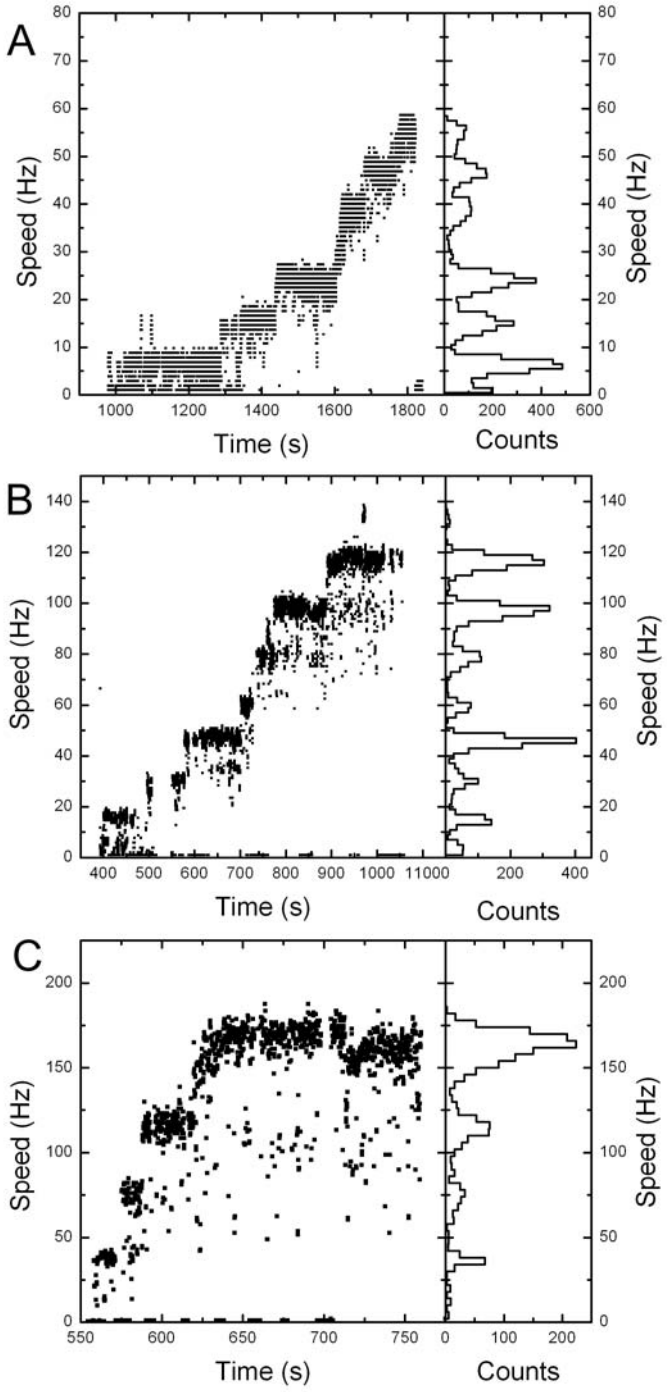

Figure 6-3: Resurrection traces and speed histograms of chimeric motor with different bead sizes. (A) 1 μm beads, histogram bin size is 1 Hz. (B) 0.75 μm beads, histogram bin size is 2 Hz. (C) 0.5 μm beads, bin size is 4 Hz.

Table 6-3

Resurrection speed level of different beads size (1 μm, 0.75 μm and 0.5 μm)

Speed (Hz)	1st Level	2nd Level	3rd Level	4th Level	5th Level	Full
1 μm	6.6 ± 1.6	15.5 ± 1.9	24.4 ± 1.2		39.2 ± 2.5	92.5±3.7
0.75 μm	15.8 ± 1.7	31.3 ± 4	46 ± 2	60 ± 3	79 ± 4	174±7
0.5 μm	38 ± 3	76 ± 10	116 ± 7	166 ± 8		402±21

6-4 Torque-Speed Relationship

Aim of Torque-Speed Relationship, and the Difficulty:

The torque-speed relationship can provide valuable information about the motor function. In steady rotation, the torque generated by the motor is balanced by the viscous drag on the bead. The motor torque has been estimated from tethered cells where the load was very high and the rotation speed was up to few hertz. Because the motor position is random in the cell membrane, the rotation center of a tethered cell is different from cell to cell. Thus, there were large errors in the torque estimated from video images of cells and rotation speeds.

In a bead assay, the viscous load of the motor can be estimated more accurately because the bead-size and the rotation radius are known. To obtain the torque-speed relationship, the speeds of the BFM at different load are required. However, the difficulty is that the torque estimation from high speed rotation measurements with small beads has higher uncertainty as discussed in detail in the next section.

6-4-1 Uncertainty of Torque-Speed Relationship

The torque generated by the motor can be estimated as,

$$T = f_r \times \omega = (f_b + f_f) \times \omega, \tag{6-1}$$

where T is the torque generated by the motor, f_r is the rotational frictional drag coefficient and ω is the angular velocity. The rotational frictional drag coefficient is the sum of the drag coefficient of the bead f_b and of the flagellar filament f_f. f_b can be estimated as

$$f_b = 8\pi\eta r_b^3 + 6\pi\eta r_b r_r^2 = g_b \eta, \tag{6-2}$$

where r_b is the radius of bead used, r_r is the rotation eccentricity of the bead, η is the viscosity of the medium, and g_b collects all the geometric parameters affecting f_b, and will be assumed to be constant for each bead on a particular motor [Berg, 1993]. This assumes no change of orientation of bead and filament with motor speed [Reid, 2006]. The bead size has 2% standard deviation. The rotation eccentricity can be measured from the orbit of the signal from the QPD. An average rotation eccentricity is ~ 200 nm in our preparation and experiments. Table 6-4 and Figure 6-4 shows the estimated rotational frictional drag coefficient f_b with different bead sizes. The drag coefficient increases rapidly with bead size.

In a bead assay, the cells were sheared to truncate the filaments. However, the length of filaments left on the motor is unknown. Assuming a 500 nm long filament rotating perpendicular to the hook (Figure 6-5), the estimated drag coefficient is ~0.5 pN nm/Hz [Berg, 1993]. At high load with a 1 μm bead, the drag coefficient from the bead is 40 times larger than a 500 nm filament and neglecting f_f gives a good estimate of the torque:

$$T = f_b \times \omega \text{ when } f_b >> f_f, \tag{6-3}$$

However, at low load with small beads, the contribution from the filament is more significant and Equation 6-3 would underestimate the torque in the high-speed region because the drag resulting from the filament is comparable to the drag from the bead in this condition. As we go to lower loads, this error becomes larger.

Table 6-4

Rotational Frictional Drag Coefficient of different size of beads.

Bead diameter	970 nm	750 nm	500 nm	350 nm	200 nm
f_b (pN nm /Hz)	20.31	10.10	3.65	1.67	0.63

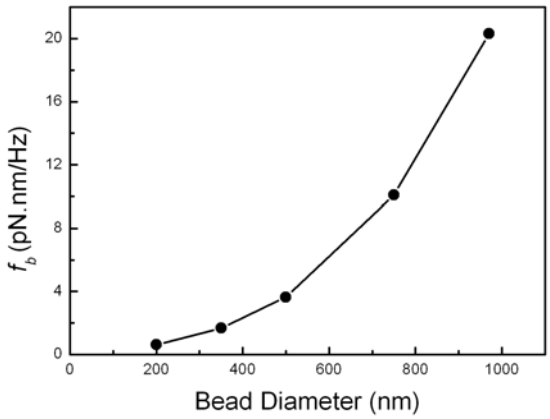

Figure 6-4: Rotational frictional drag coefficient of different size of beads, assuming rotation radius is 200 nm.

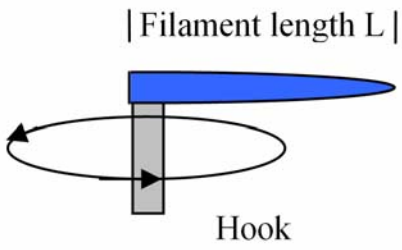

Figure 6-5: Illustration of a filament rotation perpendicular to hook.

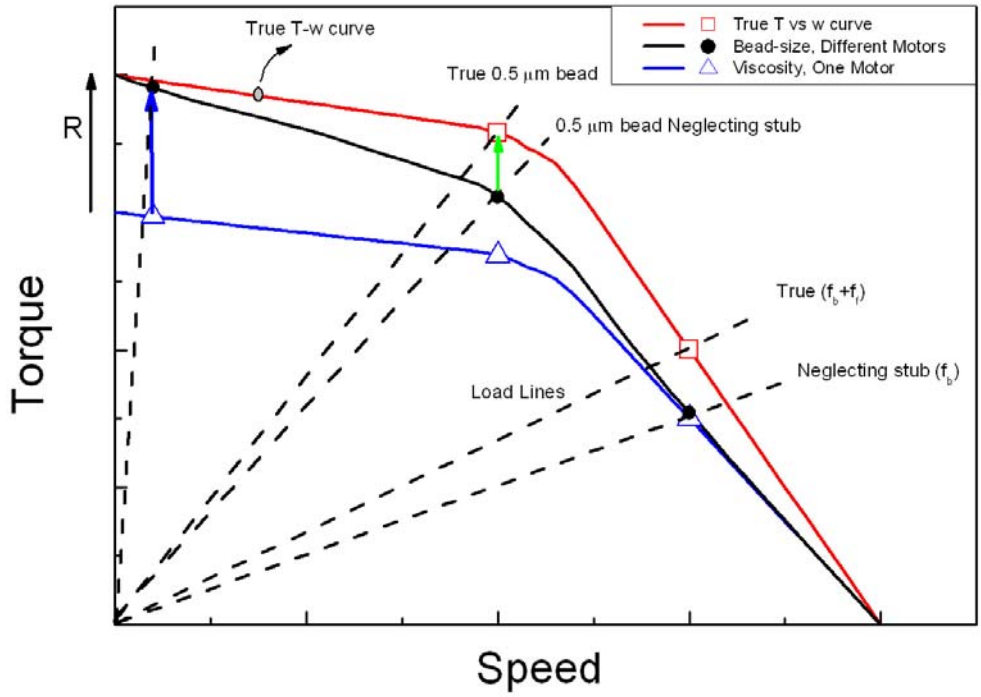

Figure 6-6: Torque-speed relationship correcting method illustration. Red line shows a hypothetical torque-speed curve for the BFM. Using a bead assay with different size of beads and steady-state induction, we can estimate a torque-speed curve from Equation 6-3, black line. In the low-load region, this torque is underestimated due to the neglect of the filament stub. In the Ficoll experiment with a small bead and increasing medium viscosity, we can also estimate the torque-speed relationship from Equation 6-3, blue line. Unlike the black line, the whole blue line has the same error ratio because the filament stub and bead are the same. Thus, the error ratio R is a constant between the red and blue line, (black arrow). By comparing torque estimated at low speed, we can rescale (blue arrows) the blue line to the true torque-speed relationship (red line). Then, by comparing the black and red lines, we can estimate the filament-drag correction coefficient that needs to be applied to torque estimates obtained from Equation 6-3 for each bead size (green arrows). These correction and filament drag coefficients can be applied to subsequent experiments in which smf and stator number are varied without the need for further viscosity experiments, as they depend only upon geometric features which are expected, on average, to be constant.

To obtain a more accurate and absolute torque-speed relationship, we improved the relative torque-speed relationship method from Berg's group [Chen, 2000a]. We can use a small bead with low load and increase the viscosity of the medium to decrease the speed. Thus the whole torque-speed curve calculated by Equation 6-3 has the same ratio of error,

$$R = \frac{f_b}{f_b + f_f} = \frac{g_b}{g_b + g_f}, \tag{6-4}$$

where $f_f = g_f \eta$ and the geometric factor for filament drag, g_f, is assumed to be constant. Because the torque estimated by Equation 6-3 with large beads is accurate, we can rescale the torque-speed relationship obtained from Equation 6-3 by the factor 1/R, given by the ratio of torques estimated by Equation 6-3 at low speed using small beads in high-viscosity and large beads in low-viscosity. Thus, the corrected torque-speed relationship can be constructed, Figure 6-6.

6-4-2 Increasing Medium Viscosity

Berg's group has tested different polymer compounds to increase the viscosity of the medium [Berg, 1979]. They found solutions containing highly branched polymers such as Ficoll [Sigma-Aldrich, Dorset, UK] are more homogeneous without forming gel-like structure. Thus it is an ideal compound for increasing medium viscosity to slow down the BFM. The viscosity versus Ficoll concentration has been obtained from a viscosity meter and sedimentation experiment [Chen, 2000a; Rowe DPhil Thesis], Figure 6-7. In this thesis, we used the same method to increase the viscosity of the medium by adding Ficoll with a small bead attached to the motor.

Experiments were carried out by preparing a motor with 0.35 μm beads in normal sodium motility buffer and then increasing medium viscosity by exchange of the motility buffer with otherwise identical buffer containing different concentrations of Ficoll (0% to 13%). Figure 6-8 shows a motor speed trace of a single motor in buffers with different Ficoll concentrations. As the Ficoll concentration increases, the BFM slows down. The motor speed can recover if the medium is exchanged back to a Ficoll-free buffer, indicating that

there is no damage to the motor. Figure 6-9 shows uncorrected torque estimated by Equations 6-2 and 6-3 which is underestimated due to the neglect of f_f.

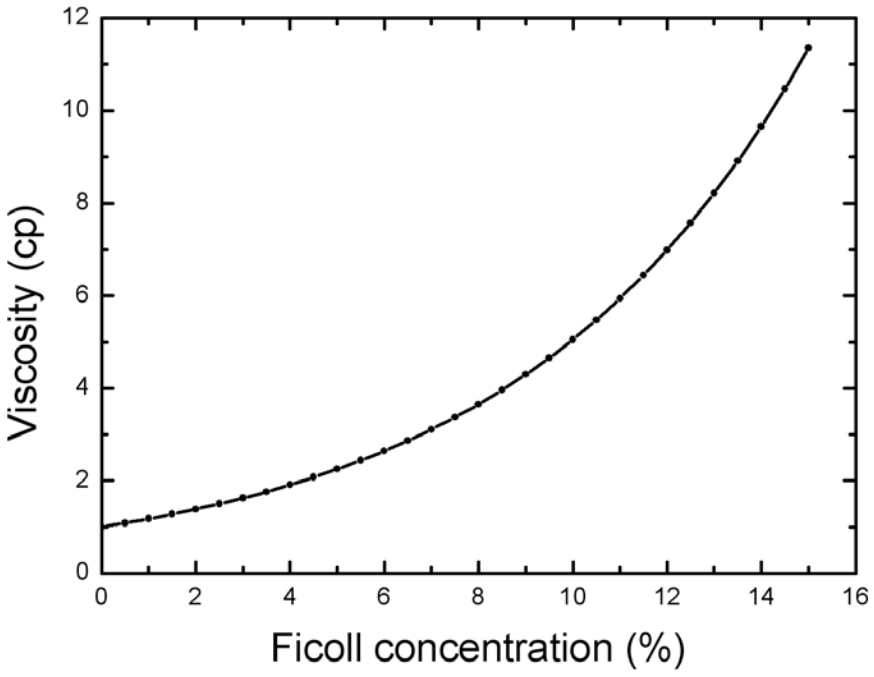

Figure 6-7: Medium viscosity versus Ficoll concentration. The viscosity η of Ficoll solution depends on its concentration C, $\eta=exp(0.162C)$. This relationship was measured by Chen and Berg [Chen, 2000a].

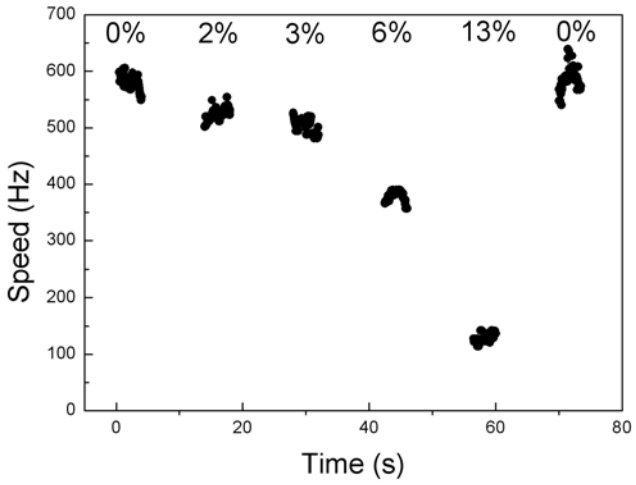

Figure 6-8: Chimeric motor speed with 0.35 μm beads in different viscosity by adding Ficoll, 85 mM $[Na^+]_{ex}$ and pH 7. The speeds of each concentration were measured for 5 s. In the end, the medium is exchanged to Ficoll-free sodium motility buffer.

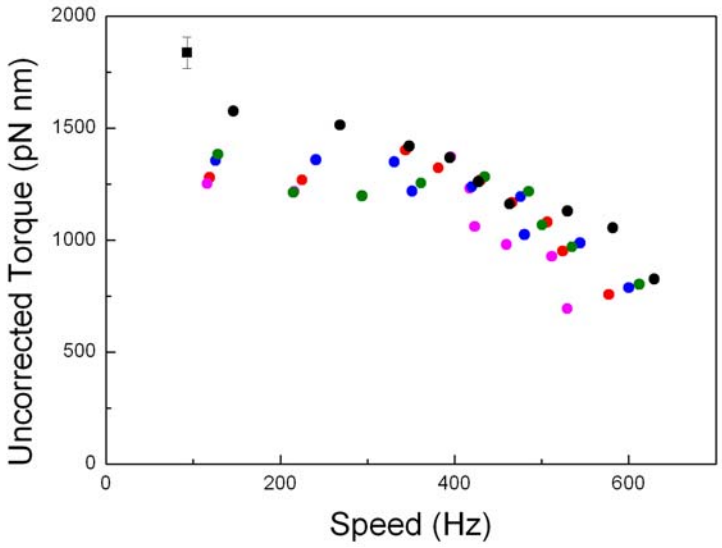

Figure 6-9: Uncorrected torque-speed relationship estimated in Ficoll experiments with 0.35 μm beads in high induction. Ficoll concentrations were varied from 0 % to 13 %. Data (circles) are from 5 different motors, each labelled with a different color. Square point is the torque estimated from 1 μm beads data which is the reference point for rescaling torque.

6-4-3 Torque and Speed

Corrected Torque-Speed Relationship:

The corrected torque-speed relationship is shown in Figure 6-10, black circles. In the high load, low speed region, the torque is about 1900 pN·nm. Two linear regressions fitting with an intersection point, ("knee speed"), are shown in black line. In the fitting, the intersection point is variable to minimize the total error. The output torque drops about 10% from zero to the knee speed of ~ 430 Hz and then decreases to a zero-torque speed of ~ 850 Hz deduced by extrapolation of the second linear fit.

The morphology of the torque-speed relationship is similar to the wild-type proton-motor in *E. coli* and sodium-motor in *V. alginolyticus*, Figure 6-10. In the *V. alginolyticus* sodium driven motor, the plateau region extends to ~ 450 Hz and the torque drops to a zero-torque speed at 710 Hz. In the *E. coli* proton motor, the plateau region extends only to ~ 170 Hz and the zero-torque speed is 350 Hz. The shapes of torque-speed relationships are similar, indicating that the mechanism behind motor rotation is probably similar.

Slower than the knee speed, the motors are believed to operate close to thermodynamic equilibrium without reaching any rate-limiting internal process such as ion-translocation and internal mechanical movement. However, in the high speed regime, the motors operate with rate-limiting internal process and lose torque. Berg's group has shown that the rate-limiting step or steps are strongly temperature dependent [Chen, 2000a] and the use of deuterium for hydrogen also reduces the torque [Chen, 2000b]. Thus, the rate-limiting step is probably related to ion-transfer.

The stall torques of these three strains are different, ~ 3800 pN nm, ~ 1900 pN nm and ~ 1300 pN nm for *V. alginolyticus* sodium motor, *E. coli* chimeric sodium motor and *E. coli* wild-type proton motor respectively. With a 1μm bead load for example, the *V. alginolyticus* sodium motor, *E. coli* chimeric sodium motor and *E. coli* proton wild-type motor rotate at 135 Hz, 93Hz and 62 Hz respectively. The ion motive forces are about -163 mV [Sowa, 2003], -187 mV [Lo, 2007; Chapter 5], and -175 mV [Castle, 1986; Lo, 2007] respectively. From the energy balance, the minimum numbers of ions

required are ~ 900 ions/rev, ~ 400 ions/rev, and ~ 280 ions/rev respectively. It is possible that the stator numbers are different or the fundamental properties of the interaction between stator and rotor are different.

The wild-type proton motor in *E. coli* and chimeric motor in *E. coli* have similar stall torque but the speed responses are different. The speed responses of the chimeric motor in *E. coli* and sodium motor of *V. alginolyticus* are similar. These observations are consistent with the hypotheses that the rate-limiting internal steps involve ion-transfer, and are slower in the proton-motor than in the sodium-motor. This may be because the sodium ion concentration (~ 10^{-2} M) is much higher than the proton concentration (~ 10^{-7} M). In this hypothesis, the ion arrival time is not the rate-limiting process in the sodium motor, at least not below ~ 450 Hz, but could limit the proton motor at speeds above ~ 170 Hz.

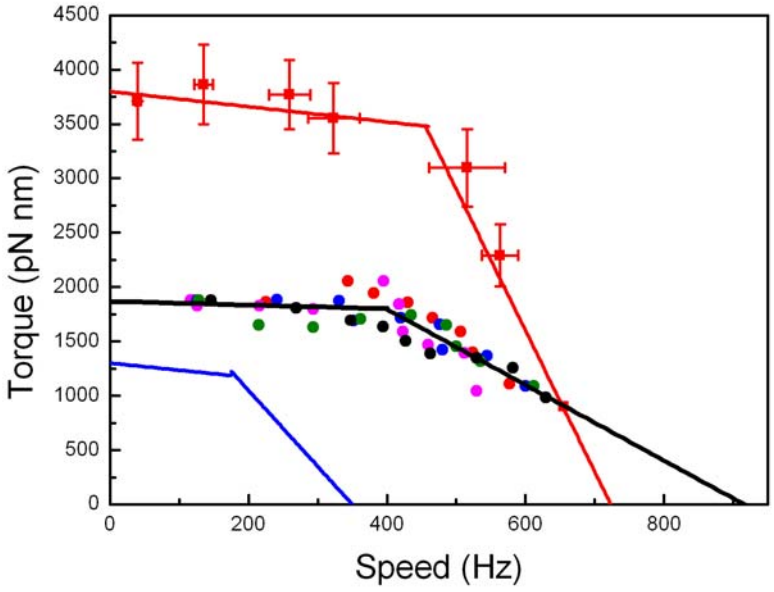

Figure 6-10: Torque-speed relation of three different BFM; sodium motor in *V. alginolyticus* [Sowa, 2003] chimeric motor in *E. coli* [This thesis] and wild-type proton-motor in *E. coli* [Chen, 2000b; Reid, 2006]. The torque-speed relationship for the chimeric motor is derived from the same data and use the same color code as in Figure 6-9.

Filament Drag Corrections:

In rescaling the torque-speed relationship derived from 0.35 μm beads in varying viscosity (blue arrow in Figure 6-6), an average factor (1/R) of 1.35 is applied. From Equation 6-4, we can estimate the average filament drag coefficient of 0.46 pN nm/Hz. By comparing the corrected torque-speed relationship to the torque estimated from different bead sizes (green arrow in Figure 6-6), we can estimate the average filament drag coefficients in each bead size. For 0.75 μm, 0.5 μm, 0.35 μm and 0.2 μm beads, the average filament correction of drag coefficients are 0.44 pN nm/Hz, 0.69 pN nm/Hz, 0.40 pN nm/Hz, and 0.73 pN nm/Hz respectively. These numbers are consistent with a few hundred nanometers of filament rotating with the beads. These corrections are useful for the torque estimation in other smf and stator number conditions without doing any Ficoll experiments.

6-5 Speed vs smf

Aim:

It has been shown that motor speed is linear with membrane potential and pH gradient in high load (tethered cells). In Chapters 4 and 5, we have demonstrated that we understand the contributions to the smf and how to control each component. Here, we examined the relationship of BFM speed and smf in high load and low-load regions. Speeds per stator are from peak-fitting in low-induction speed histogram, Figure 6-1 [Lo, 2007].

6-5-1 Motor speed versus smf in High Load and Low Load

Speed of 1 μm Beads in Different smf:

First we measured the speed of 1 μm polystyrene beads attached to chimeric flagellar motors [Lo, 2006; Reid, 2006] as a function of pH_{ex} and $[Na^+]_{ex}$, Figure 6-11(A). Figure 6-11 (B) shows the data of Figure 6-11 (A), as speed *vs* smf. The motor speed varies linearly with smf, from 8.7 to 2.2 Hz/stator over the range -187 to -54 mV. In this

high load condition the two components of smf, V_m and ΔpNa, are equivalent to within the limits of experimental uncertainty; all these data points fall onto the same linear fit.

Speed of 0.35 μm beads in different smf:

Similar measurements using 0.35 μm beads are shown in Figure 6-12. For a given value of $[Na^+]_{ex}$ (and thus also $[Na^+]_{in}$ and ΔpNa) the motor speed varies linearly with smf as V_m is varied via changes in pH_{ex}. However, the slope, and therefore the motor speed at a given smf, is lower at low $[Na^+]_{ex}$ than at higher $[Na^+]_{ex}$. V_m and ΔpNa are not equivalent as the driving force of the flagellar motor in the low load region.

Non-Equivalence of V_m and ΔpNa as Driving Force in Low Load:

In the high load regime, the speed is a linear function of smf and the two components of smf show equivalent contributions. However, in the low load regime, the motor speed shows different dependence on V_m and ΔpNa, Figure 6-12 (B). Motor speeds in low $[Na^+]_{ex}$ are slower than those in high $[Na^+]_{ex}$ for a given smf. All previous comparisons of membrane voltage and ion gradient as driving forces for the flagellar motor have been under high load and have found that the two are equivalent, consistent with high efficiency and near-equilibrium behaviour. At high speed and low load, we are observing the rates of reactions in the motor cycle far from equilibrium, and under these conditions the ion gradient and membrane voltage are not equivalent. The simplest explanation is that the diffusion-limited binding of sodium ions is the rate-limiting step at low load and low $[Na^+]_{ex}$, consistent with the argument of section 6-4-3.

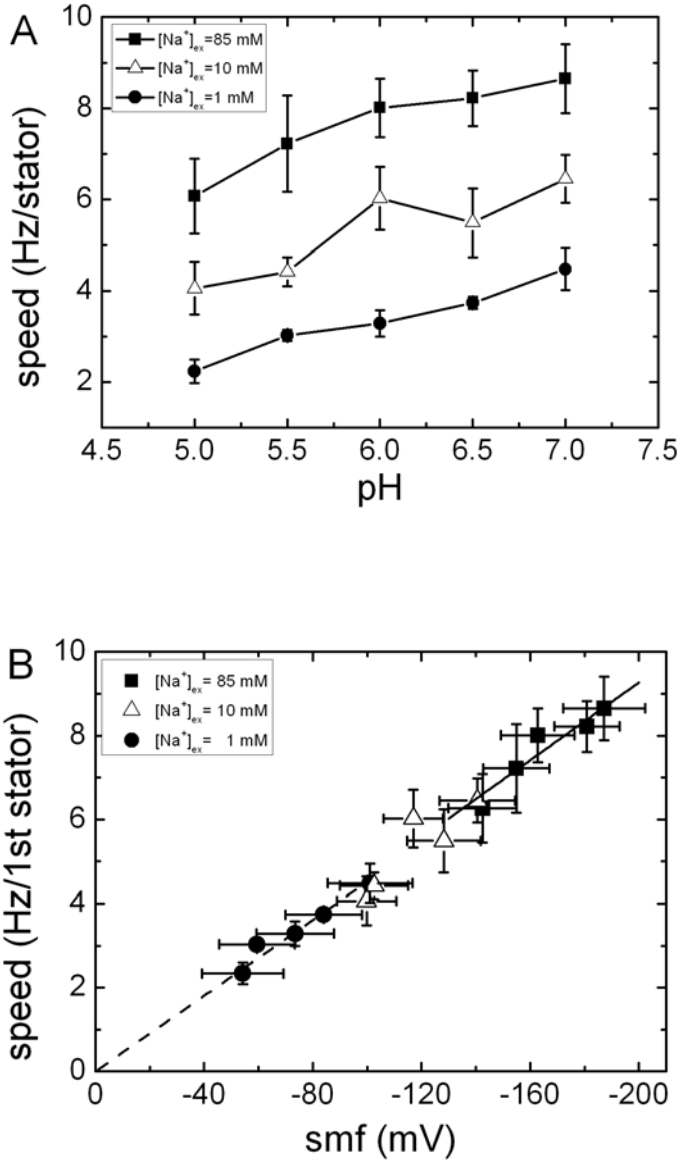

Figure 6-11: Motor speed in high load with 1 μm beads. (A) Average motor speed of chimeric motors driving 1 μm beads, versus pH_{ex} for different $[Na^+]_{ex}$. (B) Speed versus smf for pH_{ex} = 7.0, 6.5, 6.0, 5.5, 5.0 and $[Na^+]_{ex}$ = 1, 10, 85 mM. smf values in different media are from Figure 5-10. Linear fits are constrained to the origin for data at 1 mM (dashed lines) and 85 mM (solid lines) $[Na^+]_{ex}$. Fitted slopes for 1 mM and 85 mM $[Na^+]_{ex}$ respectively are -0.045 ± 0.001 Hz/stator/mV and -0.046 ± 0.001 Hz/stator/mV.

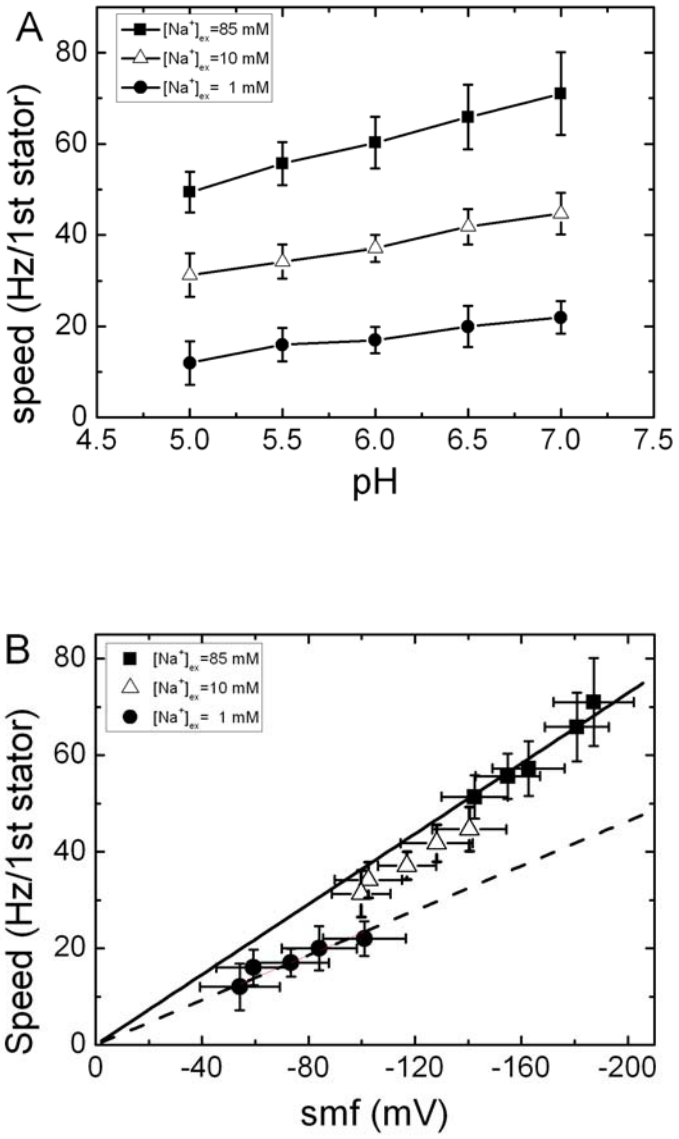

Figure 6-12: Speed vs smf of 0.35 μm beads. (A) Average speed of the first stator unit with 0.35 μm beads, versus pH_{ex} for different $[Na^+]_{ex}$. (B) Speed versus smf for the data in (A). Also shown in (B) are linear fits constrained to the origin for data at 1 mM (dashed lines) and 85 mM (solid lines) $[Na^+]_{ex}$. Fitted gradients for 1 mM and 85 mM $[Na^+]_{ex}$ are -0.23 ± 0.01 Hz/stator/mV and -0.36 ± 0.005 Hz/stator/mV.

6-5-2 Motor Instability in alkaline pH_{ex}

The pH range 5 to 7 (Figure 5-10, 6-11, and 6-12) was chosen because motor rotation was stable over this range. Figure 6-13 (A, B) shows the results of experiments in which motor speed and V_m were measured in the same cell and pH_{ex} was increased to 8. In these experiments we measured the speed of 1 μm beads attached to motors by video analysis of movies taken at 2000 frames per second [Sowa, 2005], and there were 10 s delays between successive measurements of speed and V_m. When we changed pH_{ex} from 7 to 8, some motors speeded up stably and V_m measured in the same cell increased to around -165 mV, as predicted by Equations 4-2 and 5-10 (Figure 6-13 (A), $[Na^+]_{ex}$ = 85 mM, smf = -210 mV). However, as illustrated in Figure 6-13 (B, C), many motors were unstable at pH_{ex} = 8. The motor of Figure 6-13 (B) had stopped rotating by the time of the first speed measurement, 5 minutes after the switch to pH_{ex} = 8, indicating collapse of the smf. The slow decay of V_m measurements reflects the slow response of the dye to a collapse of V_m which was probably complete within 5 minutes of the pH change. To investigate in more detail the behavior of cells at pH_{ex} = 8 we measured the speed of 0.5 μm beads attached to the motor, using the bfp method (Figure 6-13 (C)). V_m was not measured in these cells, due to technical limitations. The motor of Figure 6 (C) speeded up as we changed pH_{ex} from 7 to 8, as in Figure 6-13 (A). Within 2 minutes, however, the speed had dropped to zero as in Figure 6-11 (B). After restoring pH_{ex} = 7 the motor recovered in a stepwise manner, similar to the resurrections observed by Sowa et al. after transient de-energizations caused by removal of $[Na^+]_{ex}$ [Sowa, 2005]. We observed 11 cells out of 51 cells that maintained rotation after 20 min in pH_{ex} = 8. Thus it appears that many cells are unable to maintain rotation of chimeric flagellar motors at the high smf associated with pH_{ex} = 8, leading to a reversible collapse of both smf and V_m.

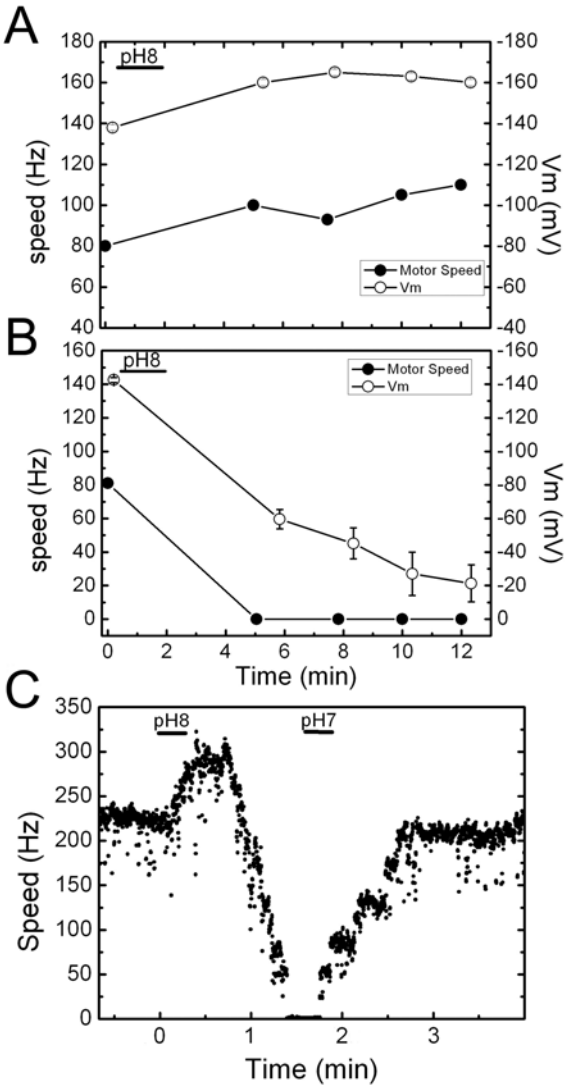

Figure 6-13: Transient responses to high pH_{ex}. (A, B). V_m and speed of 1 μm beads attached to the motor, versus time, measured in the same cell. The bar indicates the flow of buffer with $pH_{ex} = 8$; initially $pH_{ex} = 7$. After the change to $pH_{ex} = 8$, the motor and cell in (A) maintained increased speed and V_m, whereas the motor in (B) stopped, indicating zero smf and V_m. The apparent slow decay of V_m in (B) is due to slow equilibration of the dye. (C). Speed of a 0.5 μm bead attached to the motor. The change to $pH_{ex} = 8$ caused a transient increase in speed followed by a rapid collapse to zero. Return to $pH_{ex} = 7$ caused step-wise recovery to the original speed, typical of re-activation of stator units following transient de-energization.

6-6 Direct Observation of Steps in Stable Rotation

6-6-1 Experimental Conditions

The chimeric motor in *E. coli* can be slowed down by decreasing smf. The slowest stable rotation we can reach now is about 12 Hz for the first stator with 0.35 μm beads in 1 mM $[Na^+]_{ex}$ and pH_{ex}=5. In this condition, the smf is about -54 mV (~2 kT/e). The estimated relaxation time of 0.35 μm beads attached to the filament is about 0.55 ms. Given a factor of 4 and ~26 steps per revolution, the maximum speed of the motor we can observe steps with is about 17 Hz. Using the BFP position measurement with 632 nm laser, we can reach the angle resolution of 1 degree. This is an ideal condition for the steps observation.

Figure 6-14 shows the speed histogram of low induction cells in this condition. Two discrete peaks indicate motors with one and two stators. The positions of beads were recorded and ellipse fitting was made if necessary [Rowe, DPhil thesis]. The positions of beads were then converted into angle with time. Raw angle versus time data was passed through the Chung-Kennedy filter [Leake, 2004].

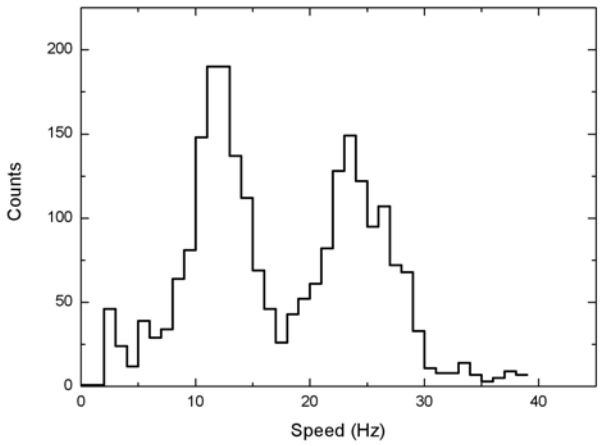

Figure 6-14: Steady-state speed histogram of the chimeric motor in low induction, low load (0.35 μm bead) and 1 mM $[Na^+]_{ex}$ and pH_{ex}=5. Two clear peaks can be observed at 12.5 Hz and 24.6 Hz by multi-Gaussian fitting.

6-6-2 Rotation Periodicity

Many motors can rotate stably in this low smf condition. Figure 6-15 (A) shows a motor angle trace versus time for 7.5 s. Average velocity of this motor is 11.43 Hz. Figure 6-15 (B) shows the instant-speed (every 0.1 s) histogram of the same trace with standard deviation of about 55 %. From the simulation of a Poisson stepper rotating 26 steps per revolution for 10 s, the standard deviation of instantaneous speed is about 50 %. Real motors probably also have smf fluctuations causing higher speed fluctuation. Figure 6-16 (A) shows the motor angle of three revolutions of the same cell. The power spectrum of the angle histogram of these three revolutions has a peak at 27/rev, Figure 6-16 (B). We also find different motors have different step periodicity from 25-27. Recent EM images of the *Salmonella enterica* motor show that the symmetry of the MS-ring varied from 24-fold to 26-fold [Thomas, 2006]. Our current data supports the variation of MS-ring symmetry and it is likely the stators interact with M-ring to generate torque.

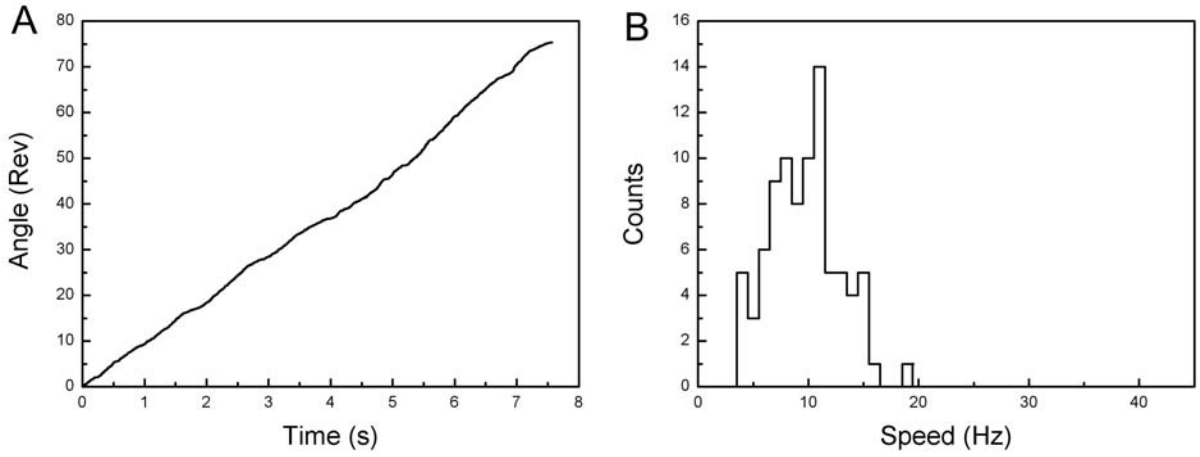

Figure 6-15: Stable rotation of the chimeric motor in low smf and low load. (A) An example of motor rotation of a 0.35 μm bead for 7.5 seconds. (B) Instantaneous speed histogram of the same trace shows a single peak at ~ 10 Hz. Speeds are calculated every 0.1 s.

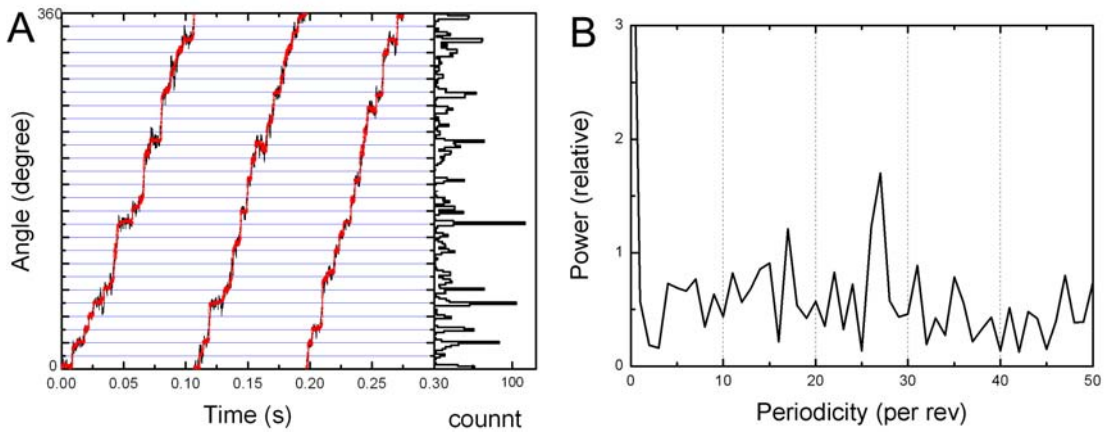

Figure 6-16: Step Periodicity. (A) Left: An example of motor rotation of a 0.35 μm bead for three revolutions. Black line and red line are raw data and Chung-Kennedy filtered data respectively. Right: Angle histogram of C-K filtered trace. (B) Power spectrum of angle histogram of three revolutions. The peak at 27 per revolution corresponds to a step size of 13.3^{o}.

6-6-3 Dwell Time Distribution

Further analysis of dwell time distribution of the same trace was presented. The trace was passed through the Chung-Kennedy filter with a window size of 25 points (2.5 ms). The histogram of angle of each revolution shows discrete and separated peaks. Each peak indicates the time the motor stays in a certain angle. Thus the distribution of the sum of data points in each peak is the dwell time distribution, Figure 6-17. The dwell time distribution can be fitted with single exponential decay with exponent t_0=3.27 ± 0.1 ms.

Assuming a Poisson stepper with stepping rate γ, the average waiting time would be τ=1/γ. The average motor speed in this period is 11.43 Hz and we found 27 steps per revolution. There are 27 step/rev × 11.43 rev/s = 308.61 steps/s. The average waiting time is 3.24 ms which is consistent with the exponential fitting of dwell time distribution. Our data suggest the single Poisson stepper mechanism behind the BFM.

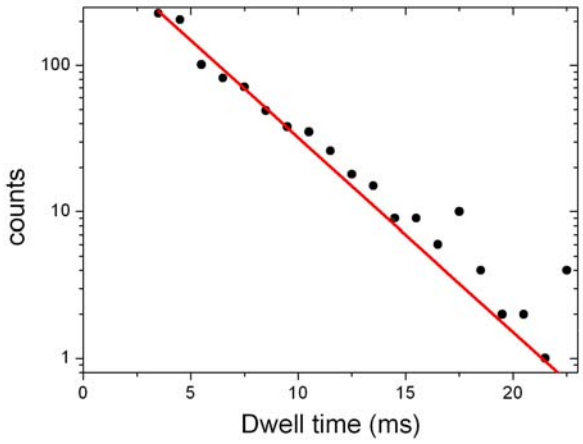

Figure 6-17: Dwell time distribution. The dwell time distribution of the same data trace in Figure 6-15. The dwell time distribution can be fitted with single exponential decay with exponent t_0=3.27 ± 0.1 ms.

6-6-4 Discussions

In this stable rotation condition, we can have a rotation trace long enough for statistical analysis within the same motor such as dwell time distribution and forward/backward steps ratio. A simple treatment of forward/backward ratio as exp(-ΔG/kT), where the ΔG is the free energy driving one step, is inaccurate because the motor probably has more than one process to complete one step cycle. More careful treatments have been proposed recently [Tsygankov, 2007; Linden, 2007]. We are cooperating with these groups for the details of the forward/backward step analysis.

In the current stable rotation condition, motor speed with one stator is ~12 Hz. When the motor rotates at 24 Hz with two stators, it is more difficult to resolve single steps. We are trying different approaches to slow down the motor by using anaerobic cells [Sowa, personal communication] or lower pH. Both of these methods are reducing membrane potential. Another approach is lowering the temperature and internal processes. Hopefully we can have step data from a motor with two stators in the near future.

6-7 Discussions

6-7-1 Ion Consumption

How many ions are needed per step?

Driving a 1 μm bead, the motor works in the high load regime close to thermodynamic equilibrium and the efficiency is close to 100 %. For cells in a medium of pH 7 and $[Na^+]_{ex}$ = 85 mM, the motor speed is 8.6 ± 0.8 Hz per stator and the smf is -187 ± 15 mV. The drag coefficient is 20 ± 2 pN nm Hz^{-1} and the work done against viscous drag in one revolution is $1087 \pm 144 \times 10^{-21}$ J per stator. By energy balance, the minimum number of ions needed for one revolution is 36 ± 6, given by the work done divided by the free energy per ion ($-e \times smf = 30 \pm 2 \times 10^{-21}$ J). Under conditions where the torque is proportional to smf, the number of ions needed to drive the motor is constant. With the motor driving 0.35μm beads at low smf ($[Na^+]_{ex}$ = 1 mM and pH 5), the minimum number of ions required for one revolution is 20 ± 9 based on the same calculation. Direct observation of 26 steps per revolution in the chimeric flagellar motor at low load and low smf [Sowa, 2005] therefore indicates that the number of ions required for one step is more than one in high load, unless the step-size is smaller at high load. At low load it is likely that the efficiency drops and that the actual number of ions per revolution is greater than the minimum required by energy balance. Alternately, the gearing stoichiometry could changes with load. Sowa et al. observed steps under conditions where motor rotation was unstable. In this work we have found conditions for stable slow rotation which will allow investigation of the statistical properties of motor stepping.

6-7-2 Torque-speed relationship

Further experiments under various loads are needed for better understanding of the motor. In particular, it will be interesting to measure torque-speed relationships with different magnitudes and components of the smf and to use these to test models of the motor mechanism that distinguish between the contributions of electrical and chemical potential.

6-7-3 Motor function and smf or pmf

The BFM speed and ion-motive force relationship has been studied in different bacteria by different methods. The primary conclusions are that V_m and ΔpI have the same contribution to the driving force in high load. In F_1F_o ATP synthesis, V_m is required to generate rotation of F_o [Kaim, 1999] which shows that V_m and ΔpNa are not equivalent. There is only one previous experiment exploring the low-load region of the BFM [Gabel, 2003]. Two motors of the same cell working at different load can be recorded simultaneously by observing a tethered cell (high load) with another motor attached to a 0.4 μm bead (low load). pmf was gradually eliminated by adding the ionophore CCCP. The high-load motor in this experiment acted as an indicator of the pmf of the cell, as previous work had shown that speed is proportional to pmf under high load. Thus the experiment demonstrated that speed varies linearly with pmf under both load conditions, although the relative contributions of V_m and pH gradient were not known. CCCP is a proton carrier that will collapse the membrane potential and thus destroy the whole proton cycle including the maintenance of internal pH. It is difficult to know in detail the disruption of each component of pmf during the application of CCCP.

By controlling the smf via $[Na^+]_{ex}$ and pH_{ex}, it is possible to drive the motor purely by V_m, setting $\Delta pNa = 0$. It may also be possible to drive the motor purely by ΔpNa, using CCCP to collapse V_m and transient changes in $[Na^+]_{ex}$ to generate a sodium gradient.

6-8 Conclusions

We can control the stator number by using different induction levels. Using the steady-state speed histogram, the speed of the motor with different numbers of stators and load can be obtained. In the resurrection experiments, we confirm the motor speed with different stator numbers. We have constructed torque-speed relationships with the steady-state speed histogram and Ficoll experiments on single motors. We have compared the motor torque with other motors and shown that the external ion arrival is probably rate-limiting at low load.

Combining single cell V_m and intracellular sodium measurements, the smf of cells can be determined. In the pH range 5.0-7.0 and external sodium concentration 1-85 mM, the smf varies from -53 to -187 mV. We can identify chimeric motor speed under different combinations of pH_{ex} and $[Na^+]_{ex}$. In high load with 1 μm beads, the motor speed is stable and varies from 2.2 to 8.7 Hz/stator. The motor speed is proportional to sodium-motive force (smf), and V_m and ΔpNa are equivalent in driving the motor, consistent with tight coupling between ion flux and rotation.

Under low load with 0.35 μm beads, the motor can rotate between 12.1 to 71.0 Hz for the first stator. The motor speed was greater with high $[Na^+]_{ex}$ and a larger ΔpNa component of the smf than with lower $[Na^+]_{ex}$ and a larger V_m component of the smf. Thus V_m and ΔpNa are not equivalent as driving forces for the flagellar motor, possibly indicating that the arrival of sodium ions is the rate-limiting step in low sodium concentrations in low load. Further experiments with different loads are needed to build up a complete motor model. Integration of the fluorescence methods we have described will be a valuable tool to understand the energetics and mechanism of the flagellar motor.

The 632 nm wavelength trap with 0.35 μm beads provides very good angular resolution. In the low smf condition, such as 1 mM $[Na^+]_{ex}$ and pH 5, the motor rotates at ~ 12 Hz. Direct observation of stepwise rotation in stable states can be achieved in these conditions. Using the Chung-Kennedy filter, we have observed 25-27 steps per revolution and a single-exponential dwell time distribution.

CHAPTER 7

CONCLUSIONS and OUTLOOK

7-1 Conclusions

Experimental Techniques:

(1) In this thesis we have developed two different single-bacterial-cell fluorescence measurements to obtain sodium-motive force. The novel intracellular sodium concentration measurements provide an example of applying fluorescence techniques to single bacterial cells. Rapid intracellular sodium measurements could be applied to other bacteria with sodium-driven motors. The membrane potential measurement was adapted from a similar method applied in mitochondria. The technique itself is not novel but the protocol we developed would be very useful for research into single-cell bacterial energetics.

(2) In the BFM speed measurements, we showed that the motor speed with different stator numbers can be determined either by resurrection or steady-state histogram with proper control of shearing and inducing stator proteins. The mechanical properties of the BFM with one or a few stators will be informative.

Chimeric Motor Energetics:

Cellular energetics is a dynamic and interesting system. Using the two fluorescence measurements, we can obtain V_m and ΔpNa of *E. coli* containing chimeric sodium motors. From $[Na^+]_{in}$ and V_m measurements, we learned,

(1) In *E. coli* cells with chimeric sodium motors, changing external sodium concentration ($[Na^+]_{ex}$) in the range 1-85 mM resulted in changes in $[Na^+]_{in}$ between 5-14 mM indicating a partial homeostasis of internal sodium concentration. Expression of chimeric flagellar motor proteins was associated with a 2- to 3-fold increase in $[Na^+]_{in}$, corresponding to an increase of ~0.34 (~20 mV) in ΔpNa, possibly due to extra sodium influx through the chimeric motors.

(2) $[Na^+]_{in}$ was measured in the range 2-20 mM and varied with $[Na^+]_{ex}$ to the power 0.17 ± 0.02. This corresponded to a ΔpNa of +0.68 to -0.85 (+40 mV to -50 mV), varying as the logarithm of $[Na^+]_{ex}$ (~0.85 units [~50mV] per decade) and changing sign at a $[Na^+]_{ex}$ in the range 5-20 mM.

(3) *E. coli* cells have $V_m = -140 \pm 14$ mV at external pH 7.0 (pH_{ex}), decreasing to -85 ± 10 mV at pH_{ex} 5.0. There is no significant difference in V_m between *E. coli* cells with chimeric sodium motors or proton motors. This indicates the V_m maintaining system is not affected by the sodium flux.

(4) Significant inter-cell variation of $[Na^+]_{in}$ at a given $[Na^+]_{ex}$ and V_m at a given pH_{ex} was observed. The number of ion pumps in one cell is small. The small number fluctuation of these pumps may cause the variation of $[Na^+]_{in}$ and V_m from cell to cell.

(5) The relationship of $[Na^+]_{in}$ to $[Na^+]_{ex}$ in different $[Na^+]_{ex}$ and pH_{ex} can provide the knowledge of ΔpNa in these conditions. We found ΔpNa depends upon $[Na^+]_{ex}$ but only weakly upon pH_{ex}. We also found V_m depends upon pH_{ex} but not upon $[Na^+]_{ex}$. This allows independent control of ΔpNa and V_m using $[Na^+]_{ex}$ and pH_{ex} respectively.

The dependence of ΔpNa upon pH_{ex} and $[Na^+]_{ex}$ and the dependence of V_m upon pH_{ex} and $[Na^+]_{ex}$ can be described by a log-linear model:

$\Delta pNa = (5 \pm 4)$ mV + (5 ± 1) mV/(pH unit) × pH_{ex} – (47 ± 1) mV/decade × $\log[Na^+]_{ex}$

$V_m = (57 \pm 4)$ mV – (28 ± 1) mV/(pH unit) + (0 ± 1) mV/decade × $\log[Na^+]_{ex}$

Thus, in a given external pH_{ex} and $[Na^+]_{ex}$ condition, we know how much energy one sodium ion can gain as it crosses the membrane, and how much of this energy is due to electrical or chemical potential.

(6) We were able to vary the sodium-motive force between -187 ± 15 mV and -53 ± 15 mV by varying pH_{ex} and extracellular sodium concentration in the ranges 7.0–5.0 and 1–85 mM respectively.

Chimeric Motor Function:

(1) We measured the torque-speed relationship of the chimeric flagellar motor in *E. coli*. The speed response is similar to wild-type sodium motor in *V. alginolyticus*. This suggests the torque generation properties strongly depend on stators.

(2) Rotation rates for 0.35 μm and 1 μm beads attached to sodium-driven chimeric flagellar motors varied linearly with V_m. For the larger beads the two components of the smf were equivalent, but for a given smf the speed of smaller beads increased with sodium gradient and external sodium concentration.

(3) In low smf conditions, stepwise rotation can be observed in a stably rotating motor. We observed 25-27 steps per revolution in these motors. This is consistent with the 24-26 fold symmetry of MS-ring. The dwell time distribution of motor steps is a single exponential. This supports the single Poisson stepper mechanism of the motor.

(4) From energy-balance, the number of ions required for one step is more than one in high load conditions.

7-2 Outlook

Extending from this thesis, the torque-speed relationship of chimeric BFM in different smf is clearly the next experiment which can clarify the contribution of V_m and ΔpNa as the driving force. We also need a new model treating V_m and ΔpNa separately as the driving force. A colleague, Fan Bai, in our group, is starting new modelling and simulation work. Another clear plan is using the knowledge from this thesis to extend the step experiments to conditions of stable rotation and known smf. From the fundamental events of rotation, these stepwise movements, hopefully we can develop a deeper understanding of the BFM mechanism.

The measurement of ion consumption of the BFM is challenging due to the small ion flux in the BFM. The estimated flux through a single BFM is only ~ 0.1 pico-amperes. The intracellular sodium measurements we developed may allow measurement of this flux if proper control of the cell volume and rotation could be made.

Full understanding of the BFM mechanism would require the knowledge of both mechanical performance and detailed structures. Several groups are keen to resolve the atomic structures of crucial stator and rotor proteins. With our efforts on the chimeric motor energetics and functions, hopefully we can understand this natural amazing rotary motor.

In terms of fundamental scientific research, knowing the mechanism of the BFM, or more generally, all molecular motors, is the ultimate goal. The application of the knowledge we learn from molecular motors may apply to many different fields including medical or industrial ones. A micro-scale pump or propeller may not be a dream in the near future.

PUBLICATIONS

Lo, C.-J., M. C. Leake, and R. M. Berry. 2006. Fluorescence Measurement of Intracellular Sodium Concentration in Single *Escherichia coli* Cells. *Biophys. J*. 90:357-365.

Lo, C.-J., M. C. Leake, Pilizota, T. and R. M. Berry. 2007. Non-equivalence of membrane voltage and ion-gradient as driving force for the bacterial flagellar motor at low load. *Biophys. J*. 93:294-302.

Reid, S., M. C. Leake, J. H. Chandler, C-J. Lo, J. P. Armitage and R. M. Berry. 2006. The maximum number of torque-generating units in the flagellar motor of *Escherichia coli* is at least 11. *Proc. Natl. Acad. Sci. USA.* 103:8066-8071.

BIBLIOGRAPHY

Amorino, G. P. and M. H. Fox. 1995. Intracellular Na^+ measurement using Sodium Green tetraacetate with flow cytometry. *Cytometry*. 21: 248-256.

Asai, Y., I. Kawagishi, R. E. Sockett, and M. Homma. 1999. Hybrid motor with H^+- and Na^+-driven components can rotate *Vibrio* polar flagellar by using sodium ions. *J. Bacteriol.* 181:6332-6338.

Asai, Y., I. Kawagishi, R. E. Sockett, and M. Homma. 2000. Coupling ion specificity of chimeras between H^+ and Na^+-driven motor proteins, MotB and PomB, in *Vibrio* polar flagella. *The EMBO*. 19:3639-3648.

Asai, Y., T. Yakushi, I. Kawagishi, and M. Homma. 2003. Ion-coupling determinants of Na^+-driven and H^+-driven flagellar motors. *J. Mol. Biol*. 327: 453-463.

Berg, H. C. 2003. The rotary motor of bacterial flagella. *Annu. Rev. Biochem*. 72:19-54.

Bernadette, S., S-I. Aizawa, R. M. Macnab, and D. J. DeRosier. 1989. Image reconstruction of the flagellar basal body of *Salmonella typhimurium. J. Mol. Biol*. 205:519-528.

Berg, H. C. and L. Turner. 1979. Movement of microorganisms in viscous environments. *Nature*. 278:349-351.

Berg, H. C. 1993. Random Walks in Biology. Princeton: Princeton University Press.

Berry, R. M. and H. C. Berg. 1999. Torque generated by the flagellar motor of *E. coli* while driven backward. *Biophys. J*. 76:580-587.

Berry, R. M., and J. P. Armitage. 1999. The bacterial flagella motor. *Advan. Microb. Physiol.* 41:291-337.

Berry, R. M. 2000. Theories of rotary motors. *Phil. Trans. R. Soc. Lond. B.* 355:503-509.

Berry, R. M. 2005. Bacterial flagellar: flagellar motor. In: ENCYCLOPEDIA OF LIFE SCIENCES. John Wiley & Sons, Ltd: Chichester http://www.els.net/

Blair, D. F. and H. C. Berg. 1988. Restoration of torque in defective flagellar motors. *Science*. 242:1678-1681.

Blair, D. F. and H. C. Berg. 1990. The MotA protein of *E. coli* is a proton-conducting component of the flagellar motor. *Cell*. 60:439-449.

Blair, D. F. 2003. Flagellar movement driven by proton translocation. *FEBS Letter*. 545:86-95.

Block, S. M. and H. C. Berg. 1984. Successive incorporation of force generating units in the bacterial rotary motor. *Nature.* 309**:**470-472.

Braun, T. F., S. Poulson, J. B. Gully, J. C. Empey, S. V. Way, A. Putman, and D. F. Blair. 1999. Function of praline residues of MotA in torque generation by the flagellar motor of *E. coli*. *J. Bacteriol*. 181:3542-3551.

Brown, P., C. P. Hill, and D. F. Blair, 2002. Crystal structure of the middle and C-terminal domains of the flagellar rotor protein FliG. *EMBO J.* 21:3225-3234.

Brown, P. N., M. A. A. Mathews, L. A. Joss, C. P. Hill, and D. F. Blair, 2005. Crystal structure of the flagellar rotor protein FliN from *Thermotoga maritime*. *J. Bacteriol*. 187:2890-2902.

Bustamante, C., D. Keller, and G. Oster. 2001. The physics of molecular motors. *Acc. Chem. Res.* 34:412-420.

Castle, A. M., R. M. Macnab, and R. G. Shulman. 1986. Measurement of intracellular sodium concentration and sodium transport in *Escherichia coli* by ^{23}Na nuclear magnetic resonance. *J. Bio. Chem.* 261:3288-3294.

Castle, A. M., R. M. Macnab, and R. G. Shulman. 1986. Coupling between the sodium and proton gradients in respiring *Escherichia coli* cells measured by ^{23}Na and ^{31}P nuclear magnetic resonance. *J. Bio. Chem*. 261:7797-7806.

Cheezum, M. K., W. F. Walker, and W. H. Guilford. 2001. Quantitative comparison of algorithms for tracking single fluorescent particles. *Biophys. J*. 81:2378-2388.

Chen, X. and H. C. Berg. 2000a. Torque-speed relationship of the flagellar rotary motor of *E. coli*. *Biophys. J*. 78:1036.

Chen, X. and H. C. Berg. 2000b. Solvent-isotope and pH effects on Flagellar Rotation in *Escherichia coli*. *Biophys. J*. 78:2280-2284.

Cohen-Bazire, G. and J. London. 1967. Basal organelles of bacterial flagella. *J. Bacteriol.* 94:458-465.

Cruz, E., A. L. Wells, S. S. Rosenfeld, E. M. Ostap, and H. L. Sweenry. 1999. The kinetic mechanism of myosin V. *Proc. Natl. Acad. Sci.USA.* 96:13726-13731.

DeRosier, D. 1998. The turn of the screw: The bacterial flagellar motor. *Cell*. 93:17-20.

Duchen, M. R., A. Leyssens, and M. Cropton. 1998. Transient mitochondrial depolarisations reflects focal sarcoplasmic reticular calcium release in single rat cardiomyocytes. *J. Cell Biol*. 142:975-988.

Duke, T. A. J., N. Le Novere, and D. Bray. 2001. Conformational spread in a ring of proteins: a stochastic approach to allostery. *J. Mol. Biol.* 308:541-553.

Ehrenberg, B., V. Montana, M.-D. Wei, J. P. Wuskell, and L. M. Loew. 1988. Membrane potential can be determined in individual cells from the nernstian distribution of cationic dyes. *Biophys. J*. 53:785-794.

Epstein, W., and S. G. Schultz. 1965. Cation transport in *E. coli*. V. Regulation of cation content. *J. Gen. Physiol*. 49:221-234.

Felle, H., J. S. Porter, C. L. Slayman, and H. R. Kaback. Quantitative measurements of membrane potential in *Escherichia coli*. *Biochemistry*. 19:3585-3590.

Fink, C., F. Morgan, and L. M. Loew. 1998. Intracellular fluorescent probe concentration by confocal microscopy. *Biophys. J.* 75:1648-1658.

Fisher, M. and A. Kolomeisky. 1999. The Force Exerted by a Molecular Motor. *Proc. Natl. Acad. Sci.USA.* 96:6597-6602.

Franklin, M. J., W. S. Brusilow, and D. J. Woodbury. 2004. Determination of proton flux and conductance at pH6.8 through single F_o sectors from *E. coli. Biophys. J*. 87:3594-3599.

Fung, D. C. and H. C. Berg. 1995. Powering the flagellar motor of *Escherichia coli* with an external voltage source. *Nature.* 3575:809-812.

Gabel, C. V., H. C. Berg. 2003. The speed of flagellar rotary motor of *Escherichia coli* varies linearly with protonmotive force. *Proc. Natl. Acad. Sci. USA.* 100:8748-8751.

Gosink, K. K. and C. C. Häse. 2000. Requirements for conversion of the Na^+-dirven flagellar motor of *Vibrio cholerae* to the H^+-driven motor for *Escherichia coli. J. Bacteriol.* 182:4234-4240.

Häse, C. C., N. D. Fedorova, M. Y. Galperin, and P. A. Dibrov. 2001. Sodium ion cycle in bacterial pathogens: evidence from cross-genome comparisons. *Microbiology and Molecular Biology Reviews.* 65: 353-370.

Hirota, N. and Y. Imae. 1983. Na^+-driven flagellar motor of an *Alkalophlic Bacillus* Strain YN-1. *J. Bio. Chem*. 258:10577-10581.

Howard, J. 1997. Molecular motors: structural adaptations to cellular functions. *Nature.* 389:561-567.

Inaba, K. 2003. Molecular architecture of the sperm flagellar: Molecules for motility and signalling. *Zoological Science*. 20:1043-1056.

Julicher, F., A. Ajdari, and J. Prost. 1997. Modeling Molecular Motors. *Rev. Mod. Phys.* 69**:**1269-1281.

Kaim, G. and P. Dimroth. 1999. ATP synthesis by F-type ATP synthase is obligatorily dependent on the transmembrane potential. *The EMBO*. 18:4118-4127.

Khan, S., M. Meister, and H. C. Berg. 1985. Constraints on flagellar rotation. *J. Mol. Biol.* 184:645-656.

Khan, S. and M. Dapice. 1988. Effect of *mot* gene expression on the structure of the flagellar motor. *J. Mol. Biol*. 202:575-584.

Khan, S., I. H. Khan, and T. S. Reese. 1991. New structure features of the flagellar base in *Salmonella typhimurium* revealed by rapid-freeze electron microscopy. *J. Bacteriol.* 173:2888-2896.

Kojima, S. and D. F. Blair. 2001. Conformational change in the stator of the bacterial flagellar motor. *Biochemistry*. 40:13041-13050.

Kojima, S. and D. F. Blair. 2004. Solubilization and purification of the MotA/MotB complex of *E. coli*. *Biochemistry*. 43:26-34.

Korn, E. D. 2000. Coevolution of head, neck, and tail domains of myosins heavy chains. *Proc Natl Acad Sci USA*. 97:12559-12564.

Leake, M. C., D. Wilson, M. Gautel, and R. M. Simmons. 2004. The elasticity of single titin molecules using a two-bead optical tweezers assay. *Biophys. J*. 87:1112-1135.

Leake, M. C., J. H. Chandler, G. H. Wadhams, F. Bai, R. M. Berry and J. P. Armitage. 2006. Stoichiometry and turnover in single, functioning membrane protein complexes. *Nature*. 443:355-358.

Lindenm M. and M Wallin. 2007. Dwell time symmetry in random walks and molecular motors. *Phys. Rev. E.* submitted.

Liu, J. Z., M. Dapice, and S. Khan. 1990. Ion selectivity of the *Vibrio alginolyticus* flgellar motor. *J. Bacteriol*. 172:5236-5244.

Lloyd, S. A. and D. F. Blair. 1997. Charged residues of the rotor protein FliG essential for torque generation in the flagellar motor of *E. coli. J. Mol. Biol*. 266:733-744.

Lloyd, S. A., F. G. Whitby, D. F. Blair and C. P. Hill. 1999. Structure of the C-terminal domain of FliG, a component of the rotor in the bacterial flagellar motor. *Nature*. 400:472475.

Lo, C.-J., M. C. Leake, and R. M. Berry. 2006. Fluorescence Measurement of Intracellular Sodium Concentration in Single *Escherichia coli* Cells. *Biophys. J*. 90:357-365.

Lo, C.-J., M. C. Leake, T. Pilizota and R. M. Berry. 2006. Non-equivalence of membrane voltage and ion-gradient as driving forces for the bacterial flagellar motor at low load. *Biophys. J*. Under review.

Loew, L. M., R. A. Tuft, W. Carrington, and F. S. Fay. 1993. Imaging in five dimensions: Time-dependent membrane potentials in individual mitochondria. *Biophys. J.* 65:2396-2407.

Macnab, R. M. 2003. How bacteria assemble flagella. *Annu. Rev. Microbiol*. 57:77-100.

Magariyama, Y., S. Sugiyama, K. Muramoto, I. Kawagishi, Y. Imae, and S. Kudo. 1995. Simultaneous measurement of bacterial flagellar rotation rate and swimming speed. *Biophys. J*. 69:2154-2162.

Mallik, R., B. C. Carter, S. A. Lex, S. J. King, and S. P. Cross. 2004. Cytoplasmic dynein functions as a gear in response to load. *Nature.* 427:649-652.

Manson, M. D., P. M. Tedesco, and H. C. Berg. 1980. Energetics of flagellar rotation in bacteria. *J. Mol. Biol.* 138:541-561.

McCarter, L. L. 2001. Polar flagella motility of the *Vibrionaceae. Microbiol. Mol. Biol. Rev*. 65:445-462.

Meister, M., G. Lowe, and H. C. Berg. 1987. The proton flux through the bacterial flagellar motor. *Cell*. 49:643-650

Meister, M., and H. C. Berg. 1987. The stall torque of the bacterial flagellar motor. *Biophys. J*. 52:413-419.

Minamino, T., Y. Imae, F. Oosawa, Y. Kobayashi, and K. Oosawa. 2003. Effect of intracellular pH on rotational speed of bacterial flagellar motors. *J. Bacteriology*. 185:1190-1194.

Molecular Biology of the Cell. 2002. Fourth Edition. By B. Albert et al. Taylor & Francis Group.

Molecular Probes, The Handbook. http://probes.invitrogen.com/handbook/

Morehouse, K. A. I. G. Goodfellow, and R. E. Sockett. 2005. A chimeric N-terminal *Excherichia coli*- C-terminal *Rhodobacter sphaeroides* FliG rotor protein supports bidirectional *E. coli* flagellar rotation and chemtaxis. *J. Bacteriol*. 187:1695-1701.

Nagata, S., K. Adachi, K. Shirai, and H. Sano. 1995. ^{23}Na NMR spectroscopy of free Na^+ in the halotolerant bacterium *Brevibacterium sp*. and *Escherichia coli*. *Microbiology*. 140: 729-736.

Nakanishi-Matsui, M., S. Kashiwagi, H. Hosokawa, D. J. Cipriano, S. D. Dunn, Y. Wada, and M. Futai. 2006. Stochastic high-speed rotation of *E. coli* ATP synthase F1 Sector. *J. Biol. Chem.* 281:4126-4131.

Neuman, K. C., E. M. Chadd, G. F. Liu, K. Bergman, and S. M. Block. 1999. Characterisation of photodamage to *Escherichia coli* in optical trap. *Biophys. J.* 77:2856-2863.

Noji, H., R. Yasuda, M. Yoshida, and K. Kinoshita Jr. 1997. Direct observation of the rotation of F_1-ATPase. *Nature*. 386:299-302.

Novo, D., N. G. Perlmutter, R. H. Hunt, and H. M. Shapiro. 1999. Accurate flow cytometric membrane potential measurement in bacteria using diethyloxacarbocynine and a ratiometric technique. *Cytometry*. 35:55-63.

Padan, E., M. Venturi, Y. Gerchman, N. Dover. 2001. Na^+/H^+ antiporters. *Biochimica et Biophysica Acta*. 1505:144-157.

Park, S. Y., B. Lowder, A. M. Bilwes, D. F. Blair, and B. R. Crane. 2006. Structure of FliM provides insight into assembly of the switch complex in the bacterial flagella motor. *Proc Natl Acad Sci USA*. 103:11886-91.

Reenstra, W. W., L. Patel, H. Rottenberg, and H. R. Kaback. 1980. Electrochemical proton gradient in inverted membrane vesicles from *Escherichia coli*. *Biochemistry*. 19:1-9.

Reid, S., M. C. Leake, J. H. Chandler, C-J. Lo, J. P. Armitage and R. M. Berry. 2006. The maximum number of torque-generating units in the flagellar motor of *Escherichia coli* is at least 11. *Proc. Natl. Acad. Sci. USA*. 103:8066-8071.

Rodriguez, E. and A. Darszon. 2003. Intracellular sodium changes during the speract response and the acrosome reaction of sea urchin sperm. *J. Physiol.* 546**:** 89-100.

Rowe, A. D., M. C. Leake, H. Morgan, and R. M. Berry. 2003. Rapid rotation of micron and submicron dielectric particles measured using optical tweezers. *J. Modern Optics*. 50: 1539-1554.

Rowe, A. D. 2005. DPhil Thesis at the University of Oxford. Rotation of the sodium driven bacterial flagellar motor.

Ryu, W. S., R. M. Berry, and H. C. Berg. 2000. Torque-generating units of the flagellar motor of *Escherichia coli* have a high duty ratio. *Nature.* 403: 444-447.

Samatey, F.A., H. Matsunami, K. Imada, S. Nagashima, T. R. Shaikh, D. R. Thomas, J. Z. Chen, D. J. DeRosier, A. Kitao, and K. Namba, 2004**.** Structure of the bacterial flagellar hook and implication for the molecular universal joint mechanism. *Nature*. 431:1062-1068.

Samatey, F.A., K. Imada, S. Nagashima, F. Vonderviszt, T. Kumasaka, M. Yamamoto, K. Namba, 2001. Structure of the bacterial flagellar protofilament and implications for a switch for supercoiling. *Nature*. 410:331-337.

Samuel, A.D.T. and H. C. Berg, 1995. Fluctuation analysis of rotational speeds of the bacterial flagellar motor. *Proc. Natl. Acad. Sci., USA.* 92: 3502-3506.

Samuel, A.D.T. and H. C. Berg, 1996. Torque generating units of the bacterial flagellar motor step independently. *Biophys. J.* 71: 918-923.

Scaduto, Jr., R. C., and L. W. Grotyohann. 1999. Measurement of mitochondrial membrane potential using fluorescent Rhodamine derivatives. *Biophys. J.* 76:469-477.

Scharf, B. E., K. A. Fahrner, L. Turner, and H. C. Berg. 1998. Control of direction of flagellar rotation in bacterial chemotaxis. *Proc. Natl. Acad. Sci., USA.* 95, 201-206.

Schliwa, M. and G. Woehlke. 2003. Molecular motors. *Nature*, 422:759-765.

Sellers, J. and C. Veigel. 2006. Walking with myosin V. *Curr. Opin. Cell Biol*. 18:68-73.

Shioi, J-I., S. Matsuura, and T. Imae. 1980. Quantitative measurement of proton motive force and motility in *Bacillus subtilis*. *J. Bacteriol*. 144:891-897.

Silverman, M. and M. Simon. 1974. Flagellar rotation and the mechanism of bacterial motility. *Nature*. 249:73-74.

Slonczewski, J., B. P. Rosen, J. R. Alger, and R. M. Macnab. pH homeostasis in E. coli: Measurement by 31P nuclear magnetic resonance of methlyphosphonate and phosphate. *Proc. Natl. Acad. Sci., USA.* 78: 6271-6275.

Sowa, Y., H. Hotta, M. Homma, and A. Ishijima. 2003. Torque-speed relationship of Na^+-driven flagellar motor of *Vibrio alginolyticus. J. Mol. Biol.* 327:1043-1051.

Sowa, Y., A. D. Rowe, M. C. Leake, T. Yakushi, M. Homma, A. Ishijima, and R. M. Berry. 2005. Direct observation of steps in rotation of the bacterial flagellar motor. *Nature*. 437:916-919.

Stock, D., C. Gibbons, I. Arechaga. A. Leslie and J. E. Walker. 2000. The rotary mechanism of ATP synthase. *Curr. Opion. Stru. Biol*. 10:672-679.

Suzuki, H., Z. Wang, M. Yamakoshi, M. Kobayashi. 2003. Probing the transmembrnae potential of bacterial cells by voltage-sensitive dyes. *Analytical Sciences.* 19:1239-1242.

Svoboda, K., C. F. Schmidt, B. J. Schnapp, and S. M. Block. 1993. Direct observation of kinesin stepping by optical trapping interferometry. *Nature*. 365:721-727.

Thomas, D., D. G. Morgan, and D. J. DeRosier. 2001. Structure of bacterial flagellar motors from two FliF-FliG gene fusion mutants. *J. Bacteriol*. 183:6404-6412.

Thomas, D., N. R. Francis, C. Xu, and D. J. DeRosier. 2006. The three-dimensional structure of the flagellar rotor from a clockwise-locked mutant of *Salmonella enterica* Serovar Typhimurium. *J. Bacteriol*. 188:7039-7048.

Tsygankov, D., M. Linden, and M. E. Fisher. 2007. Back-stepping, hidden substeps, and conditional dwell times in molecular motors. *Phys. Rev. E*. Submitted.

Turner, L., W. S. Ryu, and H. C. Berg. 2000. Real-time imaging of fluorescent flagellar filaments. *J. Bacteriol.* 182, 2793-2801.

Vale, R. D., T. Funatsu, D. W. Pierce, L. Romberg, Y. Jarada, and T. Tanagida. 1996. Direct observation of single kinesin molecules moving along microtubules. *Nature*. 380:451-453.

Visscher, K., M. J. Schnitzer, and S. M. Block. 1999. Single kinesin molecules studied with a molecular force clamp. *Nature*. 400:184-189.

Warshaw, D. M., G. G. Kennedy, S. S. Work, E. B. Krementsova, S. Beck, and K. M. Trybus. 2005. Differential labelling of Myosin V heads with quantum dots allows direct visualization of hand-over-hand processivity. *Biophys. J. Biophysical Letter*. L30.

Xing, J., Jung-Chi Liao, and G. Oster**.** 2005. Making ATP. *Proc. Natl. Acad. Sci. USA*. 102:16539-16546.

Xing, J., F. Bai, R. M. Berry, and G. Oster. 2006. Torque-speed relationship of the bacterial flagellar motor. *Proc. Natl. Acad. Sci. USA*. 103:1260-1265.

Yagasaki, J., M. Okabe, R. Kurebayashi, T. Yakushi, and M. Homma. 2006. Roles of the intramolecular disulfide bridge in MotX and MotY, the specific proteins for the sodium-driven motor in *Vibrio spp*. *J. Bacteriol.* 188:5308-5314.

Yasuda, R., H. Noji, K. Kinoshita Jr., and M. Yoshida. 1998. F_1–ATPase is a highly efficient molecular motor that rotate with discrete 120^o steps. *Cell.* 93:1117-1124.

Yasuda, R., H. Noji, M. Yoshida, K. Kinoshita Jr., and H. Itoh. 2001. Resolution of distinct rotational substeps by submillisecond kinetic analysis of F_1–ATPase. *Nature*. 410:898-904.

Yildiz, A., J. N. Forkey, S. A. Mckinney, T. Ha, Y. E. Goldman, and P. R. Selvin. 2003. Myosin V walks hand-over-hand: Single fluorophore imaging with 1.5-nm localization. *Science*. 300:2061-2065.

Yonekura, K., Maki-Yonekura, S., Namba, K. 2003. Complete atomic model of the bacterial flagellar filament by electron cryomicroscopy. *Nature*. 424:643-650.

Yorimitsu, T., and M. Homma. 2001. Na^+-driven flagellar motor of *Vibrio*. *Biochim. Biophys. Acta.* 1505:82-93

Zhou, J. and D. F. Blair. 1997. Residues of the cytoplasmic domain of MotA essential for torque generation in the bacterial flagellar motor. *J. Mol. Biol*. 273:428-439.

Zhou, J., L. L. Sharp, H. L. Tang, S. A. Lloyd, S. Billings, T. F. Braun, and D. F. Blair. 1998. Function of protonatable residues in the flagellar motor of *E. coli*: a critical role for Asp 32 of MotB. *J. Bacteriol.* 180:2729-2735.